Landslide motion assessment including thermal interaction. An MPM approach.

Author
Mauricio Alvarado Bueno

Thesis Advisors
Eduardo Alonso Pérez de Ágreda
Núria Mercè Pinyol Puigmartí

A thesis submitted to the Universitat Politècnica de Catalunya (UPC) in partial fulfillment of the requirements for the degree of DOCTOR OF PHILOSOPHY

Ph.D. program on Geotechnical Engineering and Geo-Sciences
Department of Civil and Enviromental Engineering
Barcelona, April 2018

Thesis written by Mauricio Alvarado Bueno

This work has been supported by FPI Research Fellowship Program, ref. BES-2014-068284 under the project BIA2013-48133-R

Acknowledgments

Primero que todo, agradezco al profesor Eduardo Alonso por haber confiado y darme la oportunidad de trabajar con él, por haberme ayudado y haber aportado sus ideas para mejorar el trabajo de la tesis.

También agradezco a mi co-tutora Núria Pinyol que con sus grandes aportes y visión crítica me ayudaron a finalizar exitosamente este trabajo.

Agradezco a los profesores Francisco Zabala y Ruben Rodari por la ayuda que me brindaron y a todos los colegas que me recibieron con los brazos abiertos durante mi estancia en San Juan.

Decir también que esta tesis se ha podido realizar gracias a la ayuda económica por parte del Ministerio de Economía y Competitividad del Gobierno de España y la Universitat Politècnica de Cataluña a través del CIMNE con la beca FPI BES-2014-068284.

Agradezco a todos los profesores del Departamento de Ingeniería Civil y Ambiental y del Centro Internacional de Métodos Numéricos en Ingeniería que han contribuido en mi formación académica durante el master y en la fase de doctorado.

Deseo expresar un especial agradecimiento a mi amiga y compañera Alba Yerro que me ha brindado muchísimo de su tiempo para ayudarme siempre que lo he necesitado.

Muchas gracias a todo el Grupo de investigadores MPM, ya que con las reuniones, conferencias, cursos y congresos, he reunido ideas para solventar diversas dificultades y avanzar exitosamente en el desarrollo de esta tesis.

Comentar que gracias a la ayuda por parte de Alvaro Ruiz y Ferran Parera, que con su trabajo en laboratorio han colaborado con casos de estudio para validar

parte del trabajo realizado durante la tesis.

También agradezco al personal administrativo y de secretaria del departamento de ingeniería civil y ambiental por su acompañamiento durante todos los tramites que he necesitado.

Quiero agradecer a mis compañeros de piso y amigos durante estos seis años de travesía en el master y el doctorado, Daniel Ruiz y Claudia Villarraga y también a mis compañeros de doctorado y de despacho con los que he compartido de una u otra forma; Gaia, Sergio, Luis, Rodrigo, Miguel y Mauricio.

Y finalmente, agradezco a mi familia que desde la distancia siempre han estado conmigo, especialmente a mis padres que me han brindado apoyo incondicional.

Abstract

Risk associated with landslides of natural or man-made origin depends on the prediction of the post-failure behaviour of the mobilized mass. Numerical models capable of integrating the landslide geometry and its evolution, the coupled hydro-mechanical interaction and the soil properties in the context of dynamic forces and large displacements are currently under development. This thesis is a contribution to this effort.

In this sense, the material point method (MPM) is especially suited for analysing landslides with large displacements. This numerical procedure must be accompanied by tests under controlled conditions in order to accurately check and calibrate the numerical response.

In this thesis the capabilities of the MPM code developed are evaluated through the modelling of scaled laboratory slope tests with large displacements. In order to achieve an adequate comparison of the experimental and numerical results, the experiments are analysed by means of the interpretation of sequential digital images of the movement of the granular medium during the test (PIV technique). A novel procedure is developed to obtain the field of deformations over time and the tracking of particle path in a manner suitable for comparison with numerical results calculated in MPM.

The main objective of the thesis was the development of a comprehensive calculation tool capable of simulating the behaviour of the slides from the initial triggering to the post-failure phase including thermal effects that determine the evolution of the movement.

A formulation for non-isothermal problems coupled with hydraulic and mechanical behaviour in MPM was developed and implemented. The formulation includes the dissipation of frictional work as heat, which takes place, mainly, in shear bands. The described phenomena are strongly dependent on the thickness of the shear band and this results in a strong dependence of the numerical result in MPM with

the discretization mesh. A novel procedure to solve this problem is presented in this thesis.

Finally, very rapid Vajont landslide (Italy 1963) is modelled. A plane strain 2D model is presented without an "a priori" definition of the sliding surface. In fact, in a generalization of previous and recent work, the mobilized materials are not restricted to rigid solids interconnected along a predefined contact surface and the heat generation is not it is limited to a single predefined surface. Thus, thermal interaction processes are developed throughout the model as a function of the location and intensity of deformations.

Resumen

El riesgo asociado con deslizamientos de origen natural o artificial depende de la predicción del comportamiento posterior a la rotura de la masa movilizada. Actualmente se están desarrollando modelos numéricos capaces de integrar la geometría del deslizamiento y su evolución, la interacción hidromecánica acoplada y las propiedades del suelo en el contexto de fuerzas dinámicas y grandes desplazamientos. Esta tesis es una contribución a este esfuerzo.

En este sentido, el método del punto material (MPM) es especialmente adecuado para analizar deslizamientos con grandes desplazamientos. Este procedimiento numérico debe ir acompañado de ensayos bajo condiciones controladas para poder comprobar y calibrar la respuesta numérica.

En esta tesis se evalúan las capacidades del código MPM desarrollado, mediante la modelación de ensayos de laboratorio a escala con grandes desplazamientos. Para lograr una adecuada comparación de los resultados experimentales y numéricos, se analizan los experimentos mediante la interpretación de imágenes digitales secuenciales del movimiento del medio granular durante el ensayo (técnica PIV). Con este fin, se desarrolla un procedimiento novedoso para la obtención del campo de deformaciones en el tiempo y el seguimiento de la trayectoria de las partículas de forma idónea para la comparación con resultados numéricos calculados en MPM.

El principal objetivo de la tesis fue el desarrollo de una herramienta potente de cálculo capaz de simular el comportamiento de los deslizamientos desde la rotura inicial hasta la fase de post-rotura incluyendo efectos térmicos que determinan la evolución del movimiento.

Para esto, se desarrolla e implementa una formulación para problemas no isotérmicos acoplados con el comportamiento hidráulico y mecánico en MPM. Esta formulación incluye la disipación del trabajo friccional en forma de calor, lo cual ocurre principalmente en las bandas donde se localiza la deformación de corte. Este fenómeno descrito es fuertemente dependiente con el espesor de la banda de corte

y esto se traduce en una fuerte dependencia de los resultados numéricos en MPM con la malla de discretización empleada. En esta tesis se presenta un novedoso procedimiento para solventar este problema.

Por último se presenta la modelación del movimiento ocurrido en el deslizamiento rápido de Vajont (Italia 1963). Se introduce un modelo 2D en deformación plana sin una definición "a priori" de la superficie de deslizamiento. De hecho, generalizando los trabajos hechos anteriormente, los materiales movilizados no se restringen a solidos rígidos interconectados a lo largo de una superficie de contacto predefinida y la generación de calor no se limita a una única superficie predefinida. Así, los procesos de interacción térmica se desarrollan en todo el modelo en función de la localización e intensidad de las deformaciones.

Contents

1

Chapter 1
Thesis Description

The first Chapter describes the motivation and antecedents of this work and highlights the objective of the thesis. Finally, the organization of the document is outlined.

1.1 Motivation and background

Landslides have been a big threat to human beings, their communities and the infrastructures built to have a functional civilization. There are several history cases well documented that show the casualties and damage that landslides caused (Sosio et al., 2008). The scale of damage associated with landslides is directly related with the final displacement of the mobilized mass, its velocity and acceleration of the soil movement besides the volume of the unstable mass and the internal characteristics of the deforming body.

There are not only natural landslides but also man excavated slopes. The first ones, as mentioned before, can cause large catastrophic events (loss of lives and material damages) but have low occurrence frequency, while the second ones have a larger rate of occurrence and incidence in infrastructure.

In order to have an assessment of the risk a relevant issue refers to their "static" stability as well as the consequence of possible instability. For a given case of a potential unstable mass, risk assessment depends on the post failure behaviour in terms of run-out and velocity. What is observed in the field is that landslides may exhibit widely different velocities ranging from extremely slow (velocities lower than 16 $mm/year$) to extremely rapid (velocity values higher than 5 m/sec). Several factors determine the evolution of the motion, i.e. external actions, kinematic restrictions and constitutive response of the involved material that may depend on the range of strains and thermal interaction due to frictional work dissipation. Taking into account all of these factors into a comprehensive tool able to predict the behaviour of slopes becomes a challenge.

A simple way to advance in the understanding of the response of landslides is by means of scaled tests carried out in the laboratory under controlled conditions. Scaled slopes can be built under predefined initial and boundary conditions in terms of stress and pore water pressure and simplified homogeneous geometries. The materials involved can be characterized by means of laboratory tests providing the constitutive parameters. In addition, with current techniques such as particle images velocimetry (PIV) (Adrian, 1991; Take et al., 2004; Thielicke and Stamhuis, 2014; White et al., 2003), the slope movement during failure can be recorded and analysed to obtain very accurate data about displacements and velocities and their evolution in time. With the appropriated methodology, this information can be used to identify strains and shear surfaces.

On the other hand, real slopes can exhibit a complex behaviour over long periods of time involving changes in velocity and acceleration. Such variations of static and dynamic equilibrium of landslides cannot only be explained by taking into account the modifications of external actions. Changes in resistant forces depending on the sliding velocity should also be included (Dieterich, 1979; Ruina, 1983; Skempton, 1985; Tika et al., 1996; Wedage et al., 1998).

Regarding landslide failures at high velocities, there are few explanations to the phenomena of rapid acceleration after a status of creeping behaviour. One condition that explains this behaviour is the progressive failure in brittle materials that can cause the reduction in strength parameters from peak to residual values even under small deformations (Yerro et al., 2014, 2016a,b; Zabala and Alonso, 2011). However, even this reduction of soil strength cannot explain some known extremely fast landslide failures such as Vajont landslide that reached almost 30 m/s in around 15 seconds (Hendron and Patton, 1985). According to simulations (Alonso and Pinyol, 2010; Alonso et al., 2016; Pinyol and Alonso, 2010a,b; Yerro, 2015), the only way to explain the displacements, velocities and acceleration cal-

culated for Vajont landslides, is to accept that the frictional soil strength drops to zero. The main accepted idea for this phenomenon is the reduction of the soil strength by an increment in the pore pressure due to changes in water density by temperature increments developed during the mechanical energy dissipation in the sliding area.

This idea of fast sliding due to changes in temperature was introduced by Habib (1967). Other authors (Alonso et al., 2016; Cecinato and Zervos, 2012; Cecinato et al., 2011; Goren and Aharonov, 2007, 2009; Goren et al., 2010; He et al., 2015; Uriel and Molinia, 1977; Vardoulakis, 2000, 2002; Veveakis et al., 2007; Voight and Faust, 1982) have used the same approach combining different analysis methods trying to explain Vajont rapid motion. Those works shared two simplified assumption, the first one is that the slope kinematics are solved over a simplified geometry of the real problem and the second one is the assumption that mechanical work dissipation in concentrated shear bands predefined by a simplified geometry.

A general approach to analyse static, creeping conditions and post-failure behaviour requires therefore adequate tools capable of reproducing complex models and perform numerical simulations at global and local scale. The formulation of displacement, thermal interactions and rate dependent constitutive models should be integrated in general numerical tools capable of handling large displacements and inertial terms under dynamic conditions. In this way the assumption of a predefined rupture surface is removed from the analysis.

In the last decades, different types of numerical methods have been developed taking advantage of the improvements in the technology and hardware. These developments increase the complexity of the models and get closer to real conditions. The numerical approaches to describe the soil behaviour require the discretization of the domain. Some methods consider the material as a continuum formed by sub-domains (Collatz, 1955; Donea et al., 1977; Eymard et al., 2000; Zienkiewicz, 1977) and some others methods analyse the material as a discontinuum medium formed by particles (Belytschko et al., 1994; Cundall and Strack, 1979; Gingold and Monaghan, 1977; Idelsohn et al., 2003; Monaghan, 1988). Each approach has advantages and disadvantages when examining the deformation range, boundary conditions, internal boundaries between materials, contact surfaces for soil-structure interactions, computational cost, among others. Despite this, one of the most important criteria to select a numerical method to perform an analysis is the field of application and the material type to be modelled. For example, modelling a granular material with large particle size, will be most suited for a discontinuum media method in order to get the adequate representations of the problem. The

contribution of Soga et al. (2016) provided detailed description of the application and limitations of several numerical methods.

In this Thesis, the material point method (MPM) (Sulsky et al., 1994; Sulsky and Schreyer, 1996) has been selected as a convenient tool to analyse landslides. This method consist of a mixed formulation (Fig. 1.1) that couples the advantages of meshless methods and the finite element method (FEM). It was an evolution of the "particle in cell" method used in fluid dynamics. The MPM models a solid as a collection of material points transporting the discretized information of the porous medium (strains, stresses, velocities, accelerations, water pressures, temperature, porosity, etc) moving through a background mesh (Fig. 1.1). The governing equations are solved in the nodes of the background mesh. Each material point has an initial mass that is preserved during the whole calculation process. The solution of governing equations is used to update the material points. All the information is mapped between material points and mesh nodes by means of standard shape functions as in FEM.

Detailed information for the mechanical problem (single-phase MPM formulation) can be found in Sulsky et al. (1995). The coupled hydro-mechanical problem (two-phase MPM formulation, solid-liquid) for saturated soils is described in detail by Zabala (2010), Jassim et al. (2013) and Al-Kafaji (2013). The coupled hydro-mechanical problem (three phase MPM formulation, solid-liquid-gas) for unsaturated soils was presented by Yerro (2015). These formulations were made under the one point multiphase assumption. Recently Abe et al. (2014) and Bandara (2013) have presented a new two-point formulation where the solid skeleton and the liquid phase are represented separately by two sets of material points.

In this work, a two-phase single point MPM formulation has been developed with the aim of analysing landslide including thermal effects. This MPM approach is capable of removing the limiting assumptions used so far to explore the thermal pressurization effects on landslides. In fact, the kinematics of the motion should not be an assumption made "a priori" but part of the solution. In general, heat sources are generated wherever plastic work develops.

The Geopart code, initially developed by Zabala et al. (2004) and Zabala (2010) was selected as a base code. The code follows an explicit MPM integration in a $2D$ formulation using structured rectangular mesh with four node elements. This code was used to analyse dam failures (Zabala and Alonso, 2011, 2012). Basic validation of simulations results (wave propagation, one-dimensional consolidation problem, stability of the solution) have been performed in the studies listed here.

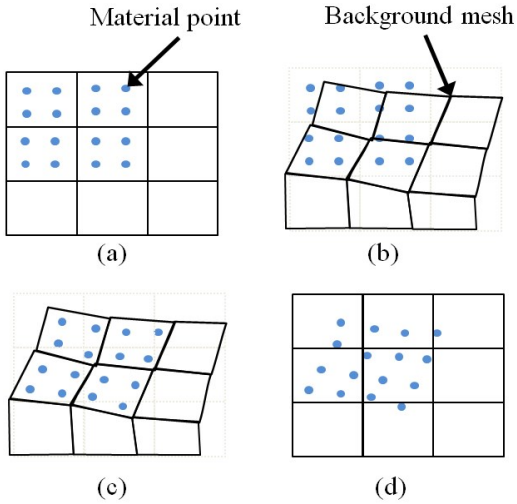

Figure 1.1: MPM approach. (a) Initial discretizacion; (b) Lagrangian phase; (c) Convective phase; (d) final phase and initial for next cicle

The displacement-water pressure-temperature $(u-p-T)$ formulation integrated in the MPM framework follows the flow chart indicated in Figure 1.2. Appendix A describes a detailed step by step of the algorithm developed.

Following the ideas previously described, this thesis proposes the objectives stated next.

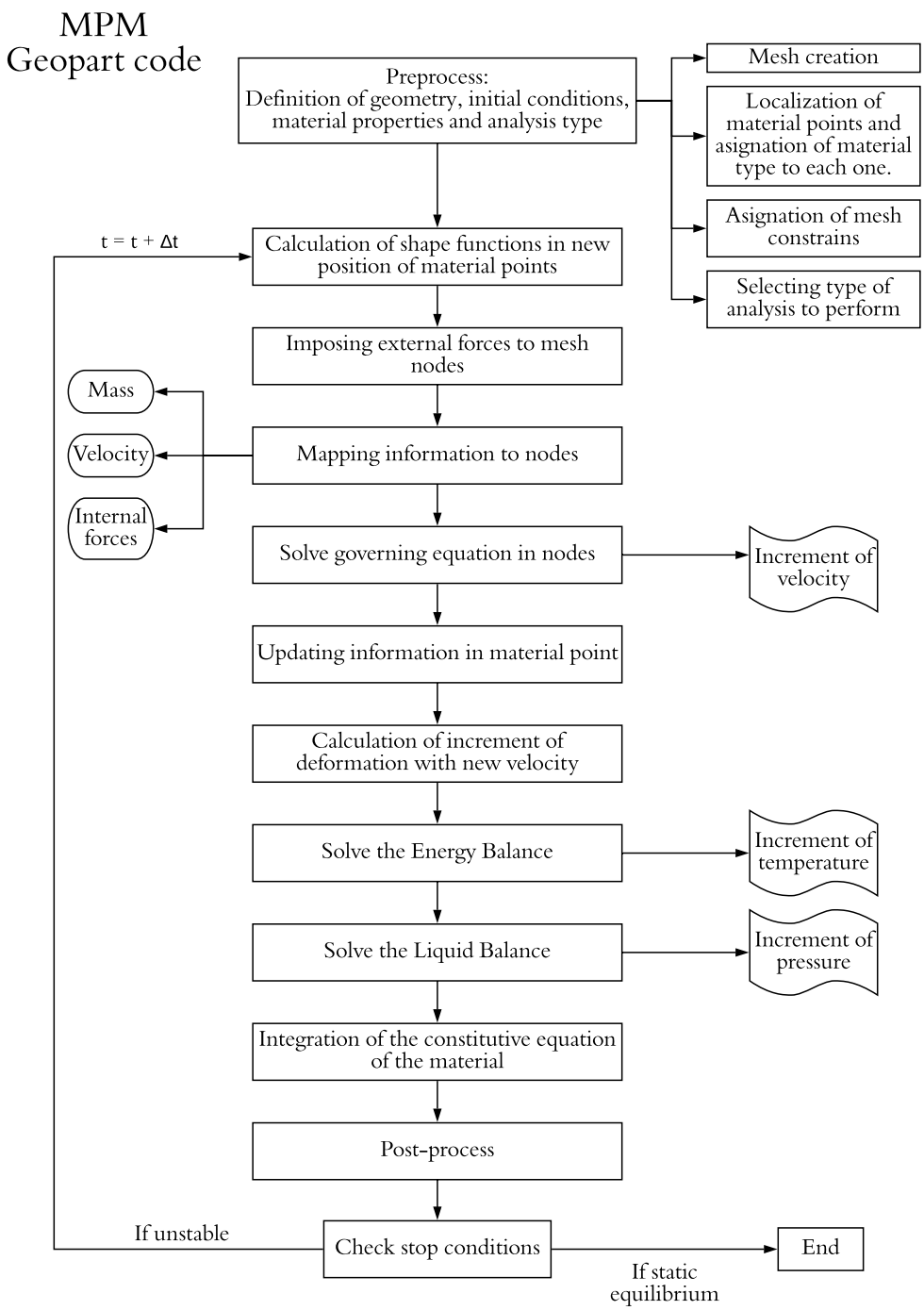

Figure 1.2: Simplified flow char of the code developed

1.2 Objectives

This Thesis focuses on developing the Material Point Method (MPM) with the aim of modelling landslides including thermal interaction, in brittle and saturated soils. In order to achieve such general purpose, the following specific objectives are formulated.

Regarding numerical improvements:

- Extending the formulation of 2 phase (solid and liquid) MPM to non-isothermal hydro-mechanic problems in saturated soil.
- Developing new numerical approaches to simulate thermally induced landslides.
- Developing a novel procedure to post-process displacement measurements taken from digital images of granular soils involving large deformations and to be able to track the position of the particles and the deformation field.

Regarding geotechnical knowledge:

- Evaluating the capability of MPM to model large deformation and displacements by simulating scaled laboratory test and centrifuge test of slope instabilities.
- Modelling the development of heating processes during landslide motion.
- Modelling Vajont landslide with MPM to analyse the development of the initial failure triggering mechanism and the subsequent post failure behaviour.
- Modelling the transition from slow to rapid landslide motion.

1.3 Methodology

After the evaluation of the state of art on landslide behaviour and its modelling, the first step carried out in the Thesis was to simulate scaled laboratory tests of slope failure to evaluate the capability of MPM (Geopart code) to simulate real cases. The experiments, which involved large displacements, were analysed by

means of particle image velocimetry (PIV) technique. Some difficulties appeared when the PIV measurements were analysed with the purpose of tracking the path of the solid particles and recovering the evolution of displacement and strain fields in time. To overcome such difficulties, a novel procedure was developed which is presented as an interesting tool to compare PIV measurements with numerical results. This is specially interesting for the case of MPM results.

Some drawbacks and limitations of the initial code were addressed to improve its capabilities:

- The Implementation of a Mohr-Coulomb constitutive models with strain softening with the aim of modelling the soil behaviour during progressive failure, following the substepping procedure proposed by Sloan (1987), in which the elastoplastic deformations are integrated in an explicit scheme by means of subdividing the increment of deformation looking for the minimization of the error. The modification in the Mohr-Coulomb law presented by Abbo and Sloan (1995) to avoid gradient discontinuities of the yield surface criterion were also included in the implementation of the constitutive model.

- Improvement the stability of the solution by inclusion of artificial damping (Cundall, 1987).

- Implementation of alternative options to integrate the internal force (GIMP, Bardenhagen and Kober (2004)).

- Implementation of changes in boundary conditions and several ways to apply external forces to obtain different triggering conditions of failure (increasing mass of a body, variation of water level and water pressures, excavation in soil)

- Implementation a the contact algorithm to deal with soil-structure problems (Alvarado et al., 2016) following the procedure proposed by Bardenhagen et al. (2000) and Bardenhagen et al. (2001).

- Improving the pre-process and creating a post-process for visual interpretation of simulation's results.

- Reducing computational cost by calculating and storing shape functions one time per computational cycle and applying a parallel calculation algorithm using OpenMP interface.

Later, the work carried out focused on the extension of the code to non-isothermal problems and its applications to thermally driven accelerated landslides. A coupled thermo-hydro-mechanical formulation was developed including the dissipation of the frictional work into heat as a source term in the energy balance equation. Synthetic cases of slopes failures were evaluated and the obtained results evidenced the mesh dependency due to the fact that the generation of heat is strongly dependent to the shear band thickness which, in the numerical simulations, is of the same order than the mesh element size.

This pathological dependence was overcome by defining embedded shear bands which a thickness is defined as an input parameter. Local thermal and hydraulical equilibrium was established between the "continuous" domain and embedded shear bands.

The procedure was applied to simples examples of slope failures used to carry out parametric studies with the aim of obtaining practical conclusions.

Finally, Vajont landslide was simulated.

1.4 Thesis layout

The Thesis is organised in 6 Chapters. The main contents are introduced here:

Chapter 2 shows a novel methodology developed to interpret sequential digital images processed with PIV technique of solids in motion with large displacements. The methodology is inspired in the MPM numerical scheme. The method is applied to synthetic cases of rectangular samples in which known displacements are imposed in order to validate the developed procedure. Finally, a laboratory scaled slope failure is analysed to show capabilities of the methodology.

In Chapter 3, two laboratory-scale sandy slope failures, involving large displacements, are interpreted with the methodology presented in Chapter 2. Results of MPM modelling for both cases are compared with the processed data from the laboratory tests in order to evaluate the accuracy of the MPM Geopart code to reproduce soil behaviour under dry and isothermal conditions.

The governing equations for saturated soils under non-isothermal conditions are presented in Chapter 4. This formulation is integrated into a general MPM numerical code following an explicit Euler approach, providing a thermo-hydro-

mechanical coupled MPM code (THM-MPM code). A reference case of an unstable saturated slope is then analysed to explore the effect of some relevant parameters. A key point regarding the effect of the shear band thickness on the motion of the landslides and the consequences of such dependence on the numerical modelling is later discussed. A new numerical strategy to overcome the mesh dependency under some assumptions is presented. The capabilities of the proposed methodology is evaluated by means of a reference case.

In Chapter 5, the THM-MPM code described in Chapter 4 is applied to analyse the well-known Vajont landslide (Italy, 1963), taking into account the available documentation on the geometry, materials involved and boundary conditions. The case is taken as a good opportunity to validate the code developed.

Finally, in Chapter 6, the general conclusions are summarised and future developments are outlined.

2

Chapter 2

Novel Procedure for PIV Measurements in Large Strain Problems

Over the last few decades, the particle image velocimetry (PIV) technique has become an interesting tool used to measure displacements in the field of experimental mechanics. This chapter presents a procedure to interpret PIV displacements, measured following an Eulerian scheme, with the purpose of providing accumulated displacements, velocities, accelerations, and strains on points representing physical particles. Strains are computed as the gradient of displacements. When compared with other standard procedures already published, the presented methodology is especially well suited to interpret large strains and large displacements. The basis of the procedure is to map displacement increments measured through PIV analysis on the subset (or patch) centres into numerical particles (NP) that are defined as portions of the moving masses whose deformation is analysed. The implementation of the method called PIV-NP is explained in detail, highlighting its simplicity. The procedure can be used as a post-processor of currently available PIV software packages. The methodology is first applied to synthetic cases of rectangular samples in which known displacements are imposed and also to a sandy slope failure experiment carried out in a centrifuge machine involving large displacements. The method reproduces satisfactorily the recorded

images.

This chapter is part of the published paper "Novel analysis for large strains based on particle image velocimetry (2017)" (See list of publication)

2.1 Introduction

Particle image velocimetry (PIV), also known as Digital Image Correlation (DIC), is widely used as a non-invasive technique to measure displacements in the field of experimental mechanics. By comparing two digital images of an object before and after deformation, incremental displacement fields are calculated to subpixel accuracy without installing sensors that may disturb the material observed. A digital photograph, understood as a set of pixels with different colour intensities, is divided into a virtual grid of subsets (also called "patches"). The entire set of pixels is integrated into regions or subsets which play the role of points. The displacement vectors observed between two photographs taken at different times is determined for each subset. The displacement is defined as the difference between the position of the reference subset centre and the corresponding subset centre in the deformable image (Fig. 2.1). A region or subset is selected instead of an individual pixel because a pixel characterized by its colour intensity will not be distinguished from others pixels. However, a set of pixels distributed in a particular manner in a given area ($l_x \times l_y$ in Fig. 2.1) which contains sufficient texture is capable of being identified in the subsequent image. A correlation criterion should be predefined to find the corresponding position of the subset in a search region of the deformed image by identifying the pattern of pixel intensity values that best represent the reference subset. It is assumed that, although the shape of the subset changes, a set of neighboring points in the reference subset remains as neighboring points in the deformed subset. The position of the deformed subset is then defined by the maximum value of the correlation coefficient.

During the last few years, research on the method led to a high accuracy on displacement and strain measurements and several image analysis algorithms and techniques have been developed to suit different applications. A description of Digital Image Correlation (DIC) and a review of the different methodologies used are presented by White et al. (2003), Pan et al. (2009) and more recently by Take (2015). Readers are referred to these contributions for a description of the methodology and a full discussion on factors that affect accuracy and precision of the technique.

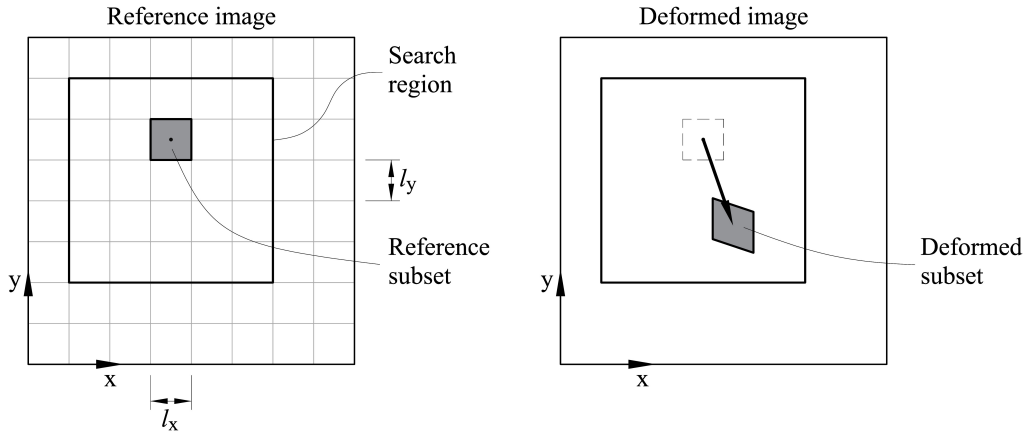

Figure 2.1: Schematic illustration of displacement measurement by means of PIV technique. (Pinyol and Alvarado, 2017)

When using PIV, the direct measurement is the "instantaneous" displacement occurred during the time interval elapsed between the capturing of two images. The displacements are measured in points located in the centres of rectangular subsets, the collection of subsets form a mesh that covers the whole image. In order to evaluate the accumulated displacement in time, the set of images captured along time can be analysed in two different ways. In the so-called "leapfrog" method, the images taken at different times are compared with an initial reference image (Fig. 2.2a). In this case, the displacement measured at each time corresponds to the displacement occurred during the time elapsed between the image analysed and the reference one. The correlation between the deformed image and the first one has a clear limit due to mismatch in regions experiencing large deformations. Alternatively, a "sequential" scheme can be selected in which the reference image is updated after every computational step and each deformed image is compared with the previous one. The coordinates of the subset are also updated to the nearest integer pixel coordinates (Fig. 2.2b). In this way, distortion which affects the correlation between images is reduced but random walk errors (White and Bolton, 2004) increase significantly because the accumulated displacement should be calculated as the sum of the displacements measured between images. Mixed options combining these two schemes are also possible. In this case, displacements are calculated with respect to a fixed reference image whilst maintaining a tolerable correlation. Once the correlation loss is significant, the reference image is updated. There are available procedures to update the reference image automatically (Stanier et al., 2016).

Alternatively, measurements can be made in an Eulerian mode in which a mesh

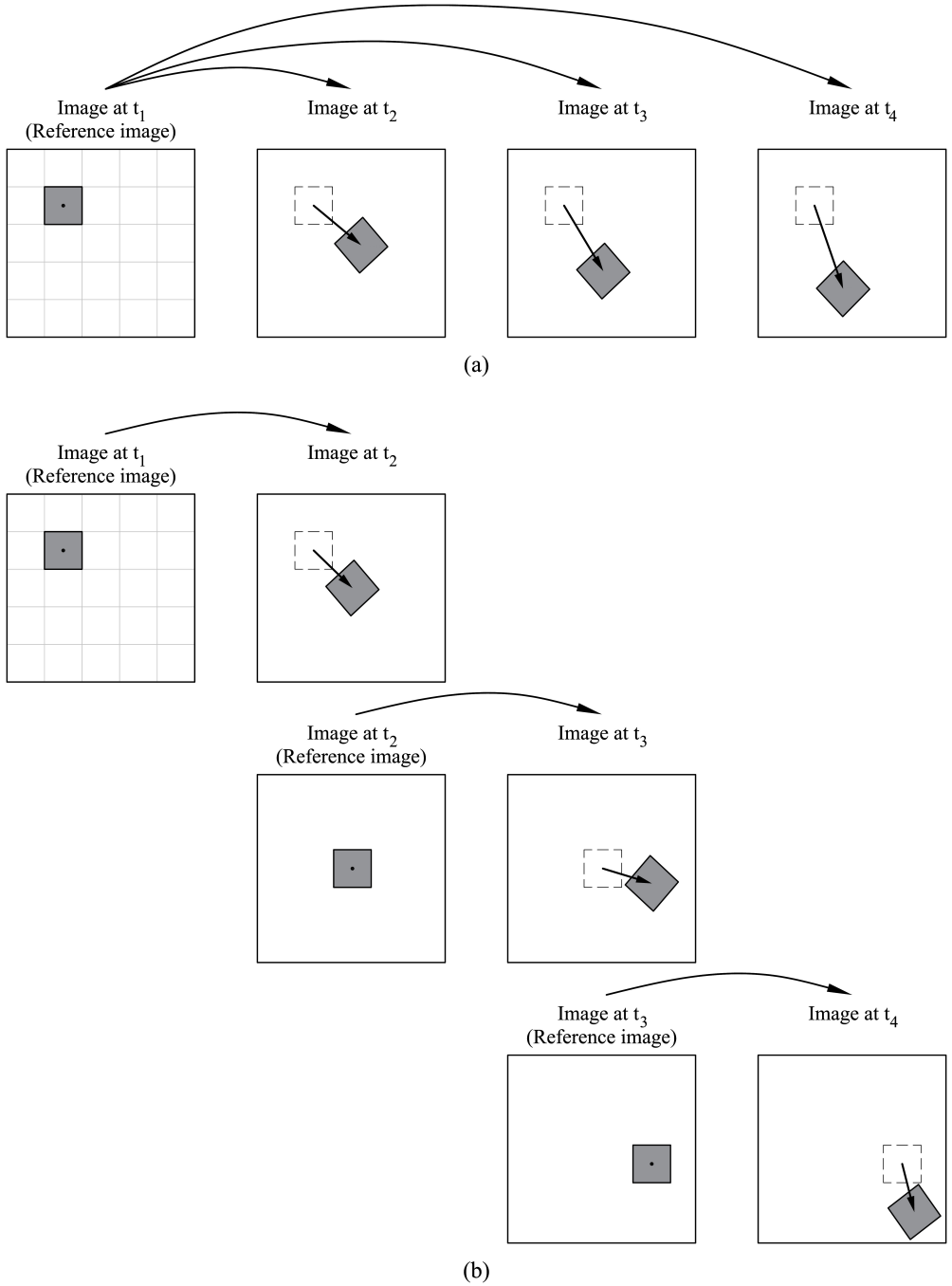

Figure 2.2: Schematic illustration of (a) leapfrog and (b) sequential schemes. (Pinyol and Alvarado, 2017)

of patches is fixed in the space and displacements measured between images refer to the same points at each computational step (Fig. 2.3). Each patch of the first image is searched in a defined area of the second image called "interrogation area". Time elapsed between images must ensure good relationship for the patch of pixels. In addition to a good correlation between the two sequential images, there are two main factors that affect the accuracy and precision of PIV measurements: the size of interrogation area and the texture of the analysed material. White et al. (2003) show that for small interrogation area (patch size lower than 10 pixels), the error substantially increases and regarding the texture of the material, a better contrast in the texture gives more precision in the measurements. Using this Eulerian scheme, the tracking of physical particles of the observed object during the motion is not directly possible.

Another important aspect of the analysis of motion is the estimation of strains. Strain distributions are required in many applications of PIV in solid mechanics where the response of the material depends on the strain path histories. In addition, the evolution of strains is of especial interest in the validation of numerical methods and constitutive models by comparing numerical results with direct or indirect PIV measurements.

Field strain distributions can be obtained directly from digital image correlations using a non-zero-order approximation mapping functions for the displacement field in the subset region (Lu and Cary, 2000). First-order mapping functions only allow rigid translation between reference and deformed subset. A second-order functions are required in order to allow translation, rotation, shear, normal strains and their combinations.

Alternatively, displacement gradients (strains) can be directly calculated by differentiating (numerically) the measured displacement field. This issue is discussed by Pan et al. (2009) who highlight the fact that the differentiation of the displacements amplifies the noise (errors inherent to the PIV technique) associated with the computed displacement. The accuracy of strain estimated by differentiating displacements can be improved by smoothing previously the computed displacement field. Smoothing algorithms (Sutton et al., 1991; Tong, 1997) and (Wang et al., 2002) have been presented to remove the noise inherent to the measured displacement. This aspect is out of the discussion presented in this work. Strains will be calculated from displacements assuming the noise level has been significantly decreased after applying some technique.

One of the techniques available to estimate strains is the point wise local least squares fitting technique used and advocated by Wattrisse et al. (2001) and Pan

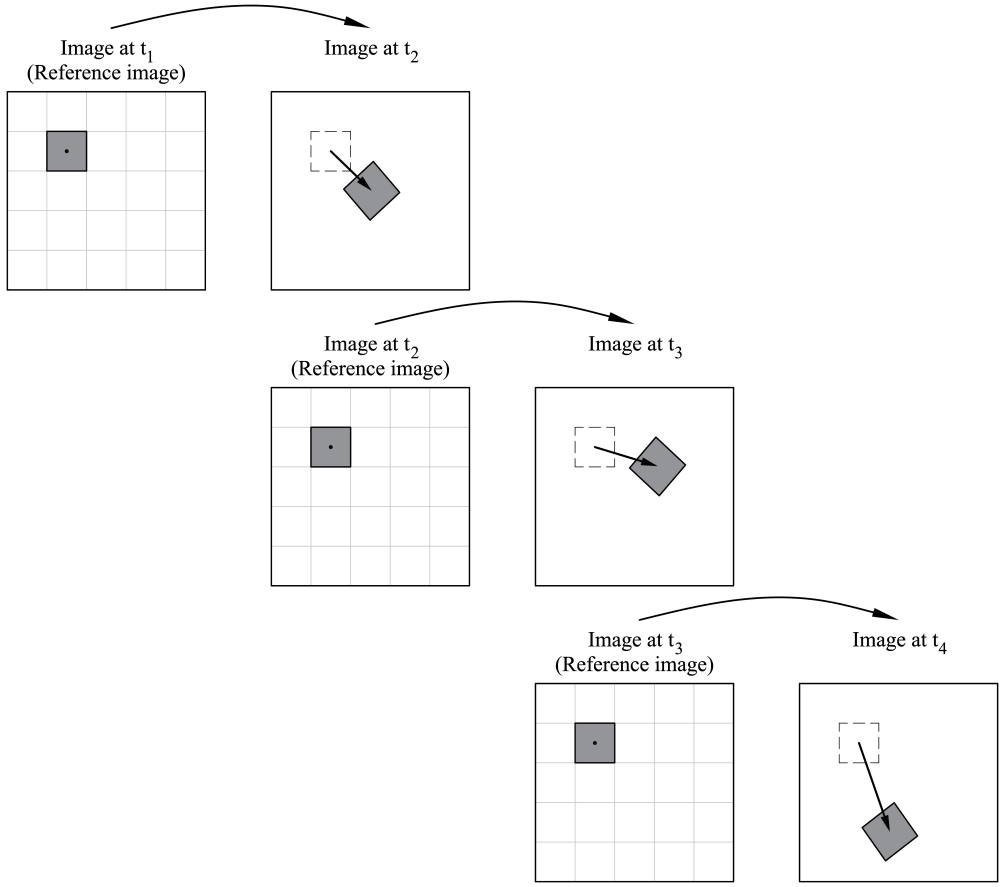

Figure 2.3: Schematic illustration of Eulerian approach. (Pinyol and Alvarado, 2017)

et al. (2009, 2007). The strains at a given point are calculated by selecting a square window where it is assumed that the strains are small enough to approximate the displacement distribution as a linear plane. This technique is limited to estimate the "instantaneous" strains calculated from "instantaneous" displacement distributions referred to fixed points in the space. Therefore, accumulated strains occurred in a deformable object cannot be directly calculated.

White and Bolton (2004) presented a procedure to calculate strains from single displacements increments by dividing the PIV subset into triangular elements and calculating the deformation gradient matrix expressed in strain and rotation components. Based on finite element methods, strain fields occurred during a given interval of time are calculated in the nodes from the displacements measured

by PIV technique of the triangular elements. This methodology has the same limitations present in the finite element method. Large deformation implies severe distortion of the defined elements leading to computation errors.

This chapter addresses some limitations encounter when using PIV technique in large deformation problems by presenting a numerical tool for processing the PIV measurements. The methodology allows the calculation of the accumulated displacements and strains in points as well as other variables such as velocity and acceleration. Such points, called numerical particles (NP), will represent a portion of the soil analysed and their motion will be tracked. The variables resulting from the methodology are calculated from PIV measurements following an Eulerian approach (Fig. 2.3). The methodology is inspired by numerical tools that combine two spatial discretizations: Eulerian based on, fixed reference points in the space, and Langrangian, which follow the moving reference points attached to the material. This double discretization of the domain and the deformable objects allow the estimation of large accumulated displacements and strain fields without numerical problems resulting from the distortion of elements of the mesh discretizing the space.

A description of the proposed methodology is first presented by giving the basis of the method and the equations required to calculate the displacement field in points attached to the observed deformed object. To facilitate the understanding and implementation of the presented methodology the formulation is given in detail. Applications of the method are finally presented. Synthetic cases of constant deformation of rectangular samples are first presented and, later, a scaled landslide experiment of a sandy slope is analysed.

2.2 PIV-NP post-process: Calculation procedure

2.2.1 Description

In the procedure presented here, the input data are the displacement occurred during the time elapsed, Δt, between two successive digital images, measured by means of PIV in the centres of a rectangular grid defining the subsets. Eulerian mode is selected (Fig. 2.3) which means that displacement are measured at the centre of each subset, fixed in the space, and the reference image is updated after every computational step. It is assumed that the data provided by PIV is: (i) the time interval Δt elapsed between image capturing; (ii) the coordinates of

each centre of the rectangular grid where displacements are measured at each computational step (they remain fixed throughout the analysis); and (*iii*) the corresponding displacement increments, $u(t)$, at each centre of the rectangular grid.

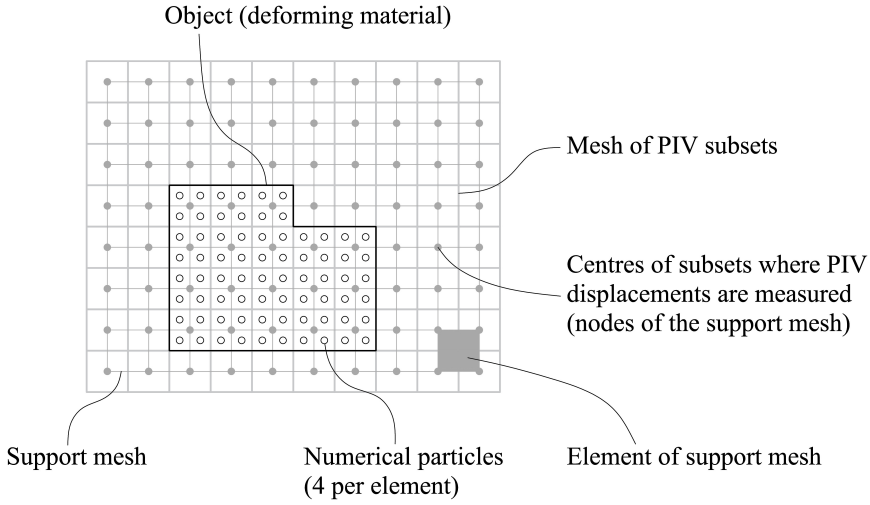

Figure 2.4: Schematic illustration of discretizations. (Pinyol and Alvarado, 2017)

Consider now a rectangular mesh, which will be called support mesh, formed by rectangular elements defined by nodes coinciding with the subset centres in which displacement increments are measured in PIV (Fig. 2.4). Each rectangular element will be constituted by four nodes in which displacement are measured by PIV analysis. This is an assumption. However, other alternatives of elements having a higher number of nodes would be possible (as discussed in a next section). This mesh should cover all the subsets used in PIV. The object or objects analysed have to be located on this mesh.

The elements of the support mesh that are totally or partially filled by the reference continuous mass should be identified. This identification can be done manually or using a preprocessor program as those typically used for finite element calculations. Notice that the support mesh will be extended beyond the limits of the initial configuration of the deforming solid in order to track the evolution of the entire motion. In the elements occupied by the objects, one or more points should be assigned and distributed inside of each element, for example in the gauss points position. These points, called "numerical particles" (NP), will represent the portion of the material initially contained in the element. Figure 2.4 shows a representation of the PIV subsets, the support mesh and 4 numerical particles per element. The numerical particles tracked throughout the deformation his-

tory of the body and their position in time will be determined by projecting the displacement increments from the nodes of the support mesh to the numerical particles, allowing them to move through the domain. Standard shape functions (N_i) (Zienkiewicz, 1989) are used to map the displacement increments from nodes of the supporting mesh to numerical particles. The displacement of any numerical particle located at position of the domain is then approximated as follows:

$$\mathbf{u}_p(t) = \sum_{j=1}^{N_n} \mathbf{u}_j(t) N_j(\mathbf{x}) \tag{2.1}$$

where N_n is the total number of nodes of the support mesh (which are equivalent to the number of centres of the subset) and $\mathbf{u}_j(t)$ is the displacement of node j at time t. Linear shape functions have been selected here since the elements of the support mesh are defined by 4 nodes. Shape functions are calculated analytically by defining a local system of coordinates, ξ and η, located at the centre of the element, whose coordinates are (x_c, y_c). Then:

$$\xi = \frac{x - x_c}{l_x/2} \; ; \; \eta = \frac{y - y_c}{l_y/2} \tag{2.2}$$

where l_x and l_y are the horizontal and vertical lengths of the element (Fig. 2.1). The value of the interpolation function at node j is:

$$N_j = \frac{1}{4}\left(1 + 2\frac{\xi\,\xi_j}{l_x}\right)\left(1 + 2\frac{\eta\,\eta_j}{l_y}\right) \tag{2.3}$$

where (ξ_j, η_j) are the local coordinates of node j. A discussion on the selection of the order of the shape function is presented later.

Time is discretized into time steps coinciding with the times of image capturing. The displacement of each numerical particle, p, located at $\mathbf{x}_p$ is then calculated with Equation (2.1) for each time:

$$\mathbf{u}_p^{t_{k+1}} = \sum_{j=1}^{N_n} \mathbf{u}_j^{t_{k+1}} N_j\left(\mathbf{x}_p^{t_k}\right) \tag{2.4}$$

where $\mathbf{u}_j^{t_{k+1}}$ is the displacement increment read as a input data at time $t_{k+}1$ and subindex p indicates the numerical particle, which ranges from 1 to N_p.

The velocity, $\mathbf{v}_p^{t_{k+1}}$,and acceleration, $\mathbf{a}_p^{t_{k+1}}$,of the numerical particles can be now calculated:

$$\mathbf{v}_p^{t_{k+1}} = \frac{\mathbf{u}_p^{t_{k+1}}}{\Delta t_k} \tag{2.5}$$

$$\mathbf{a}_p^{t_{k+1}} = \frac{\mathbf{v}_p^{t_{k+1}}}{\Delta t_k} \tag{2.6}$$

The strain increments of each numerical particle can be expressed as a function of the nodal displacement increments:

$$\Delta\varepsilon_p^{t_{k+1}} = \sum_{j=1}^{Nn} \mathbf{B}_j^{t_k}\left(\mathbf{x}_p\right)\mathbf{u}_j^{t_{k+1}} \tag{2.7}$$

where $B_j^k\left(\mathbf{x}_p\right)$ is the strain matrix of the elements at time k evaluated at the position of the numerical particle p:

$$\mathbf{B}_j^{t_k} = \begin{bmatrix} \frac{\partial N_j}{\partial x} & 0 \\ 0 & \frac{\partial N_j}{\partial y} \\ \frac{\partial N_j}{\partial y} & \frac{\partial N_j}{\partial x} \end{bmatrix}^{t_k} \tag{2.8}$$

and $\frac{\partial N_j}{\partial x} = \frac{\partial N_j}{\partial \xi}\frac{\partial \xi}{\partial x}$ and $\frac{\partial N_j}{\partial y} = \frac{\partial N_j}{\partial \eta}\frac{\partial \eta}{\partial y}$ can be easily calculated with Equation (2.2) and Equation (2.3). Accumulated strains $\Delta\varepsilon_p^{t_{k+1}}$ during large displacements result from the sum of the incremental strains $\varepsilon_p^{t_{k+1}} = \varepsilon_p^{t_k} + \Delta\varepsilon_p^{t_{k+1}}$ which are calculated assuming small displacements.

Finally, the position of the numerical particles is updated as follows:

$$\mathbf{x}_p^{t_{k+1}} = \mathbf{x}_p^{t_k} + \mathbf{u}_p^{t_{k+1}} \tag{2.9}$$

At the next time step, new displacement increments are considered in the same nodes of the mesh from PIV measurements. These values of displacement increments are mapped to the particles located at the new position calculated in the previous step.

2.2.2 Algorithm steps

To summarize, the algorithm steps are indicated below including some particular details that may be useful for the numerical implementation of the method.

- Step 1. Identification of the rectangular mesh nodes by reading their coordinates from PIV results

  The advantage of using a rectangular mesh is that the position of nodes can be determined by knowing the position of one node (assigning coordinates $(0, 0)$ to the reference node), the width and the height of the elements, and the number of rows and columns of elements. Notice that this information should be specified in PIV because it corresponds to the dimension of the subsets. The position of the nodes can be then identified by means of the numbering of the columns and rows instead of their coordinates, which is advantageous regarding numerical aspects. However, the PIV-NP post-process procedure presented in this chapter is general, and it can be also implemented in a general mesh defined by nodes (corresponding to the subset centres) not regularly distributed.

- Step 2. Identify the elements that are filled by the observed deforming material

  An input file should be specified, indicating in which elements numerical particles should be defined. They define the initial position of the observed material.

- Step 3. Locate numerical particles in the non-empty elements

  Step 3 is defined by

$$\mathbf{x}_p^{t_{k+1}} \text{ for } p = 1, N_n \tag{2.10}$$

After defining the number of numerical particles per element, they should be distributed into the element assigning coordinates to particles.

- Step 4. Read, from PIV measurements, displacement increments at nodes

  Step 4 is defined by

$$\mathbf{u}_j^{t_{k+1}} \text{ for } i = 1, N_n \tag{2.11}$$

- Step 5. For each numerical particle, identify the nodes of the element in which the numerical particle is located

  Identifying the nodes can be easily done specially in case of a regular mesh.

- Step 6. Map the displacement to the numerical particles

  Step 6 is defined by

$$\mathbf{u}_p^{t_{k+1}} = \left[\sum_{j=1}^{4} \mathbf{u}_j^{t_{k+1}} N_j\left(\mathbf{x}_p^{t_k}\right)\right]^{(e)} \text{ for } p = 1, N_p \tag{2.12}$$

  Since local expressions of shape functions are used, the displacement of each numerical particle is calculated at element level (e), taking into account the four nodes surrounding the particle identified in the previous step (step 5).

- Step 7. Calculate strain increments at numerical particles

  Defined by:

$$\Delta\varepsilon_p^{t_{k+1}} = \left[\sum_{j=1}^{4} \mathbf{B}_j\left(\mathbf{x}_p^{t_k}\right) \mathbf{u}_j^{t_{k+1}}\right]^{(e)} \tag{2.13}$$

  Since local expressions of spatial derivatives of shape functions are used, strain increments are calculated at element level (e) for the nodes surrounding the particle in which strain increments are calculated. Such nodes have

been identified for each particle in step 5. In order to avoid mesh locking problems due to linear shape functions, the gradient of displacement is calculated in the center of the element.

- Step 8. Update the position of the numerical particles and other variables of interest:

$$\mathbf{x}_p^{t_{k+1}} = \mathbf{x}_p^{t_k} + \mathbf{u}_p^{t_{k+1}} \tag{2.14}$$

- Step 9. Calculate variables of interest that are stored in the numerical particles:

$$\mathbf{v}_p^{t_{k+1}} = \frac{\mathbf{u}_p^{t_{k+1}}}{\Delta t_k}; \mathbf{a}_p^{t_{k+1}} = \frac{\mathbf{v}_p^{t_{k+1}}}{\Delta t_k}; \varepsilon_p^{t_{k+1}} = \varepsilon_p^{t_k} + \Delta\varepsilon_p^{t_{k+1}} \tag{2.15}$$

2.2.3 Discussion on shape function order and number of particles

In the description of the PIV-NP post-process methodology presented earlier, the support mesh selected is defined by linear rectangular elements (four nodes) (Fig. 2.5); therefore, linear shape functions are used for interpolation. Other alternatives would be possible, for instance, rectangular elements with nine nodes or triangular elements with three nodes (Fig. 2.5). In any case, notice that the total number of nodes and their position is fixed, since they are defined in the previous PIV analysis. The element selected and the shape function associated will allow the interpolation of the displacement field between nodes of the support mesh, which coincide with the subset centres where displacements are measured in PIV. The accuracy of the results will depend on the real displacement field analysis as well as on the number of nodes defined as an input data in PIV. Given a support mesh, the use of elements of higher order will allow a better approximation of the field displacement. Consider for discussion a one-dimensional case that deforms during a time step following a polynomic function of third order (Fig. 2.6a). The displacement increments at each computational step will only be known in the nodes (five nodes in the one-dimensional example of Fig. 2.6a). If four linear elements (two nodes per element) are selected (Fig. 2.6b), the displacements will be interpolated linearly, and the approximation will be poorer than the solution obtained from two quadratic elements (three nodes per element) (Fig. 2.6c). The exact solution is obtained in the case of using cubic elements (four nodes). Notice that for this case of cubic elements, there is a node that cannot be included in the

analysis, and the displacement measured at this node will be lost. This possibility should be taken into account in the definition of the region of interest in PIV.

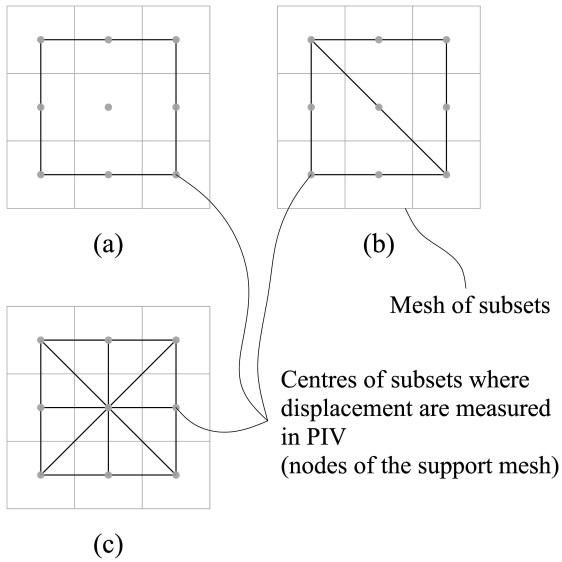

Figure 2.5: Examples of alternative elements of the support mesh. (Pinyol and Alvarado, 2017)

The accuracy will be better if the number of nodes defined in PIV is higher (Fig. 2.6d). For this case, it will probably be an acceptable linear interpolation. Linear elements, and linear shape functions for interpolation, are able to reproduce deformation modes with constant gradient of displacement (constant strain) into the element. Therefore, they allow the exact representation of translations, rotations, uniform normal and shearing strains, and their combinations.

In general cases, taking into account the complexity of real experiments, complicated deformation states may occur. However, displacement increment fields, successfully obtained in PIV techniques, are subjected to a proper correlation between images analyzed at subset level. The subset size, which will determine the number of nodes, is a critical factor to control the accuracy of measured displacements (Pan et al., 2009). On one hand, the size of a subset should be large enough to exhibit a sufficiently distinctive intensity pattern contained in the subset to distinguish itself from the other subsets. It is directly related with the texture of the sample analyzed. On the other hand, the subset size should be selected taking into account the underlying deformation field and the type of the approximated displacement mapping used in PIV analysis. Given a deformation field occurs in a computational step, a small subset can accurately be approximated by low-order approximation mapping (zero-order or first-order subset shape functions),

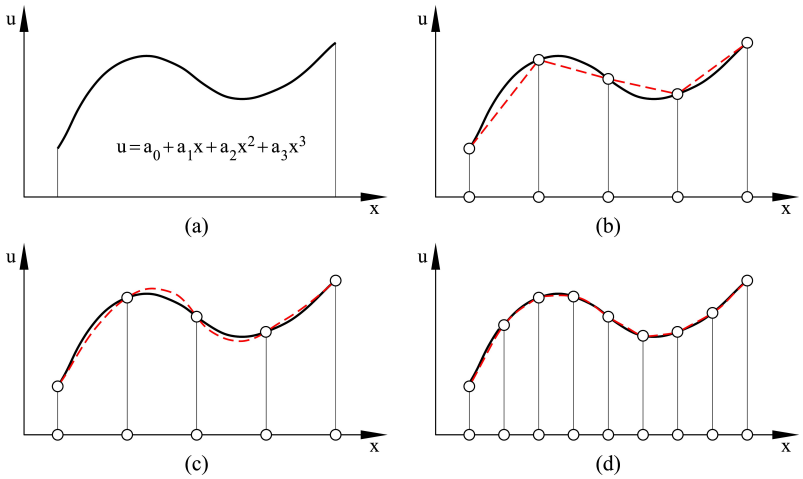

Figure 2.6: Interpolation of cubic polynomic function with five nodes: (a) analytical function; (b) linear interpolation with four elements of two nodes; (c) quadratic interpolation with two elements of three nodes; (d) lineal interpolation with eight elements of two nodes. (Pinyol and Alvarado, 2017)

whereas larger subset sizes leads to larger errors in the approximation and may lead to loss of correlation in those subsets subjected to significant strains.

When using zero-order subset shape functions in PIV analysis, it is assumed that the subset does not deform (motion of a rigid solid), whereas first-order subset shape functions involve linear deformation of the subset. In both cases, once PIV measurements are successfully obtained and given a subset size, a linear interpolation of the displacement increments between nodes of the support mesh in the PIV-NP post-process analysis will approximate reasonably well the displacements because PIV data were obtained using functions of the same or lower order than the interpolation functions in PIV-NP. Only in those cases in which the subset size is so large and the level of the deformation is such that the use of subset shape functions of second-order is required, the use of non-linear shape functions in PIV-NP post-process will be justified.

The criterion for the selection of the number of numerical particles per element should take into account that the numerical particles represent a portion of the material, and they act as points where the displacement field is stored. The data evaluated in the nodes are lost at each computational step. A greater number of numerical particles may be able to provide a better approximation.

In addition, a low number of particles, i.e., one per element, may result in empty

elements during calculations. Then the displacements given by PIV in subsequent computational steps in nodes belonging to such empty elements will not be considered in the analysis.

2.3 Simple validation examples

2.3.1 Constant deformation of rectangular samples

Consider rectangular samples of 2×2 m, in which displacements are imposed at the nodes of the support mesh with mesh element of 0.5×0.5 m to simulate the following cases: (*i*) constant horizontal deformation (Fig. 2.8); (*ii*) constant shearing (Fig. 2.10); and (*iii*) a combination of a translation and rotation without deformation (rigid solid) (Fig. 2.12). The imposed displacement at nodes simulates the input data from a PIV analysis in Eulerian mode. All cases will be simulated with one and four particles per element to examine their effect.

Figure 2.8b shows the results of constant horizontal deformations of a sample. Displacement field simulating a 24% horizontal constant strain is imposed in nodes. The computational mesh is also plotted in the figure. The incremental displacements are imposed at each of the 15 computational steps. Note that the displacement increments in nodes located at the sixth column of the mesh are initially zero. Nodal displacements on the sixth column become positive once the sample deformation is large enough to reach the position of those nodes. A linear distribution of the position of the particles along the horizontal correlation is obtained in both cases (for one and for four particles per element) (Fig. 2.7a). The displacement in time for the particle at the right in 1-particle discretization and a mean value for the 2 last particles at the right for the 4-particle discretization is plotted in Figure 2.7b. The horizontal strain accumulated in particles is exactly equal to the imposed one (24%) (Fig. 2.9).

An exact solution of deformation is also computed in the case of a sample with an imposed shearing equal to 10%. Figures 2.10 and 2.11 show the final displacement field and the computed strain, respectively. Finally, Figure 2.12 shows the results when the sample is translated and rotated with respect its centre. The exact solution is obtained in calculated results of the PIV-NP.

In these cases, in which the exact solution is computed because the strain gradient is constant, the number of particles does not affect the results.

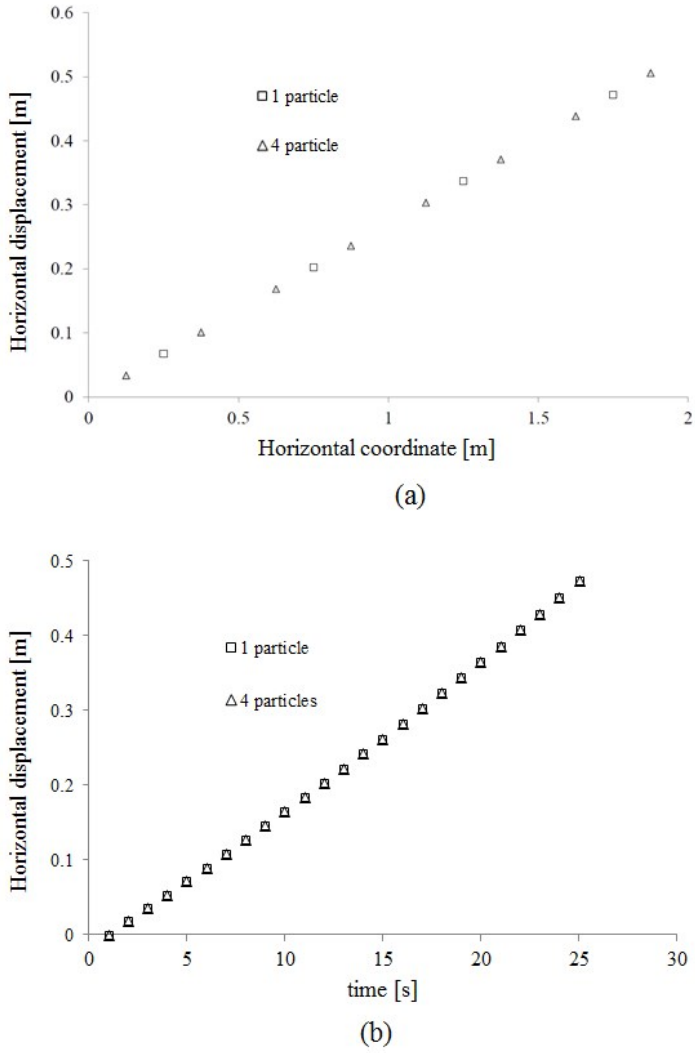

Figure 2.7: Displacements [m] for case of imposed constant horizontal deformation on rectangular sample for one and four particles per element. (a) Total horizontal displacement calculated in numerical particles at the end of analysis; (b) total displacements in time (4 particles calculated as mean value of last 2 particles at right)

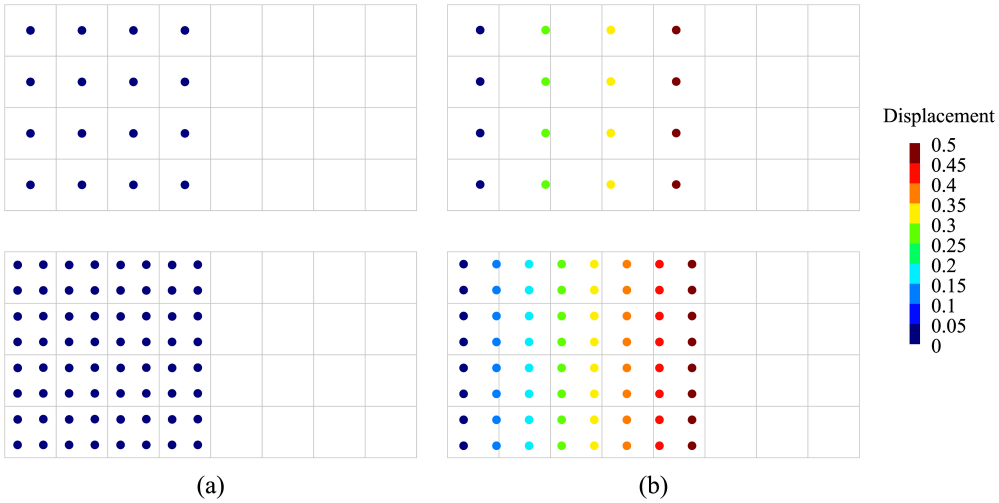

Figure 2.8: Displacements [m] for case of imposed constant horizontal deformation on rectangular sample: (a) initial configuration of numerical particles; (b) final position and displacement. For cases of one and four particles per element. Grey mesh corresponds to computational mesh.

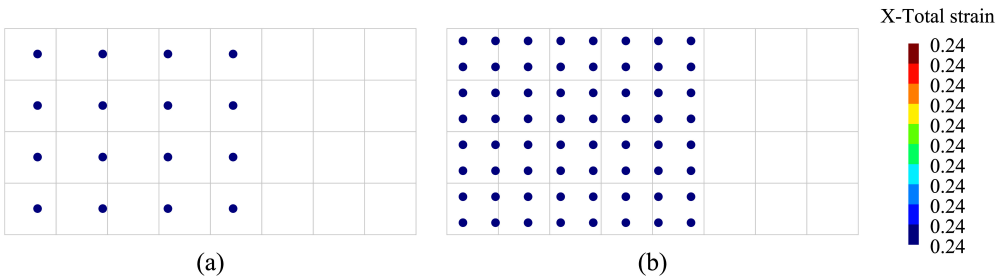

Figure 2.9: Horizontal deformation for the case of imposed constant horizontal deformation on rectangular sample. Computed with (a) one and (b) four particles per element.

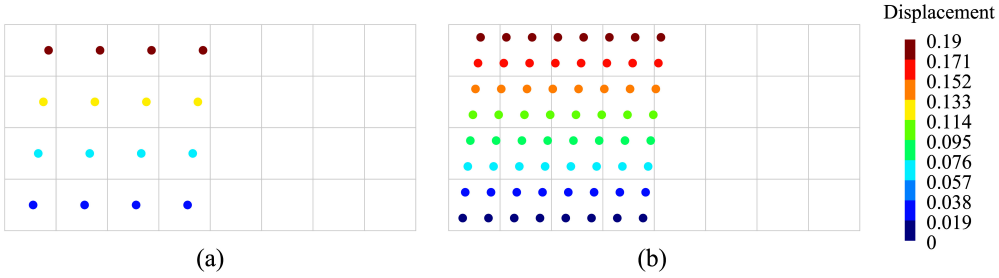

Figure 2.10: Final displacement field [m] for the case of imposed shearing. Computed with (a) one and (b) four particles per element.

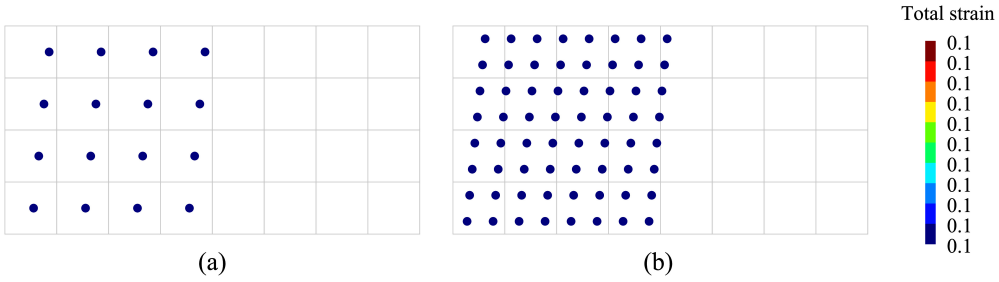

Figure 2.11: Case of imposed shearing. Final total strain computed with (a) one and (b) four particles per element.

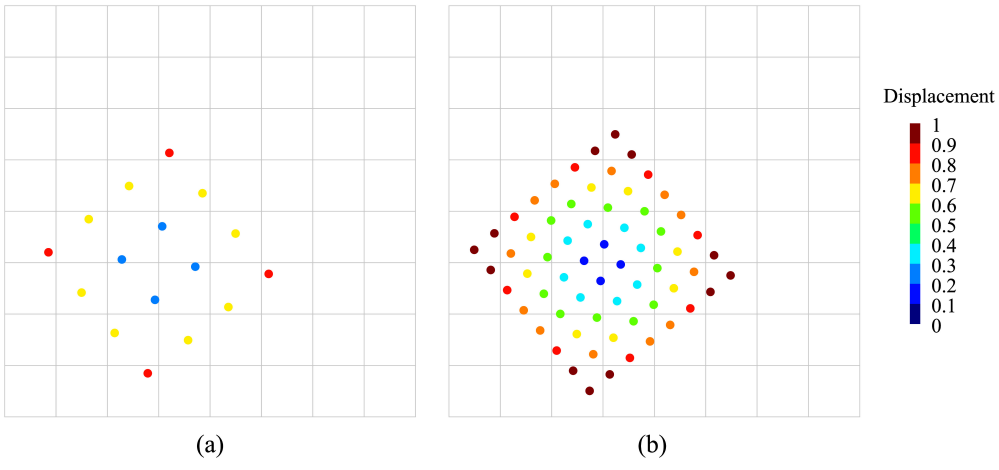

Figure 2.12: Final displacements field [m] for the case of translation and rotation. Computed with (a) one and (b) four particles per element.

2.4 PIV-NP analysis of a slope failure in a centrifuge machine

A laboratory silty clayey slope failure is analysed with the procedure previously described. The slope was built in a box with transparent walls placed in a centrifuge machine. An increased gravity is applied to ensure more realistic stresses. The increase of the gravity acceleration is applied to the slope under unsaturated conditions. The slope is later wetted by water injection from the bottom. The deformation of the slope and the subsequent failure is analysed.

2.4.1 Description

The slope model was carried out in the centrifuge machine of the geotechnical laboratory of the University of Andes in Bogotá (Colombia). The model of the slope was built in the transparent box shown in Figure 2.13a (where the dimensions on the slope are indicated). The slope inclination is 50°. The soil is a silty clay of low plasticity ($w_L = 33\%$, $IP = 18\%$) used in the construction of a dam core (Albagés dam, Spain). Initially, the soil had an average water content equal to 10% and an average dry density equal to 1500 kg/m^3. A column of gravel is built on the right side of the slope at the contact between the soil and the box lateral wall, to facilitate the saturation of the slope in the manner observed in Figure 2.13.

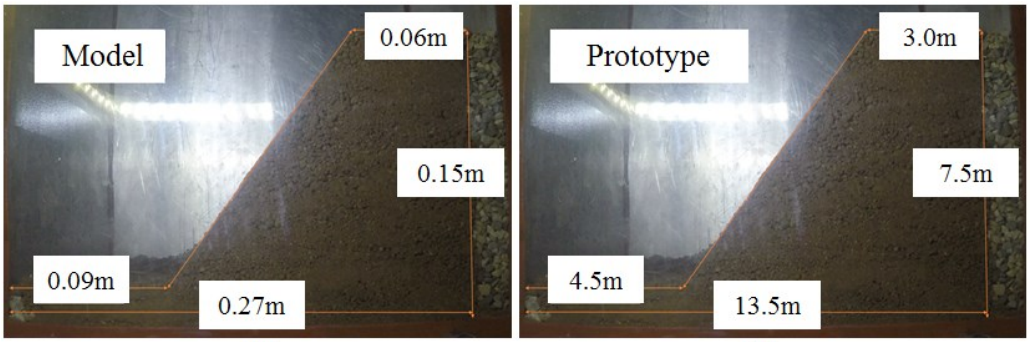

Figure 2.13: Silty clayey slope after construction in the transparent box located inside the centrifuge machine. (a) Model $1g$; (b) Equivalent dimensions in prototype $50g$. Ruiz et al. (2017b)

After slope construction, the centrifuge flight started, increasing the gravity until

$50g$ which corresponds to an increase the scale of the model of 50 times. Therefore, the 15 cm height of the slope model is equivalent to 7.5 m (Fig. 2.13b) in the slope prototype. During centrifuge flight water injection from the box base is imposed.

The whole experiment is recorded by means of a digital image captured in a video with a digital camera GoPro with 1440 pixels resolution and 60 FPS. The images were analysed in PIV. This technique allows the non-invasive measurement of displacements occurred in the time elapsed between the capture of two images. In the analysis performed here, interrogation areas of 100×100 pixels were selected, a mesh size of 0.212×0.212 m in the prototype and 9 numerical particles per element were used.

The images show the settlement of the slope when gravity increases. During wetting, water went up through the soil and, more quickly, through the sandy column. The settlement of the slope is also observed during wetting as a consequence of the collapse strains. At a certain time, the failure of the slope took place and the final inclination of the slope, after equilibrium is restored, is equal to 28°.

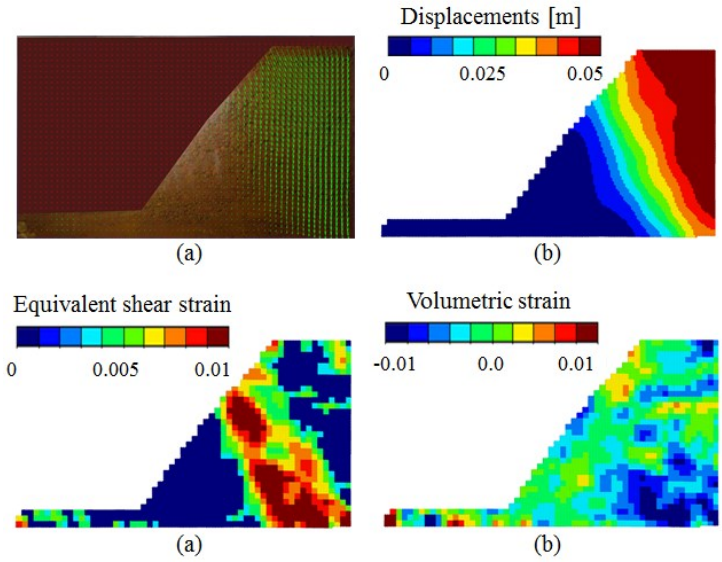

Figure 2.14: Measurements at the end of the gravity increase stage ($t = 10s$). (a) Incremental PIV displacements vectors occurred during 2 seconds; (b) Accumulated displacement $[m]$; (c) Accumulated deviatoric strain; (d) Accumulated volumetric strain.

2.4.2 Experimental results

Three stages of the motion of the slope were identified. Firstly, the slope settled due to the increase of gravity till $50g$. Figure 2.14 shows the displacement and strains occurred during this first stage of loading. Figure 2.14a shows the displacement vectors measured by comparing two images captured at the end of the loading stage which are directly obtained by PIV. The accumulated displacements, obtained by means of PIV-NP, are plotted in Figure 2.14b. The displacements are larger in the zone where the slope is higher. A maximum displacement of 5 cm is measured. A clear shear zone is observed in the middle of the slope due to the different settlements between the toe and crest zone. Maximum volumetric strains are measured in the deepest zone of the slope.

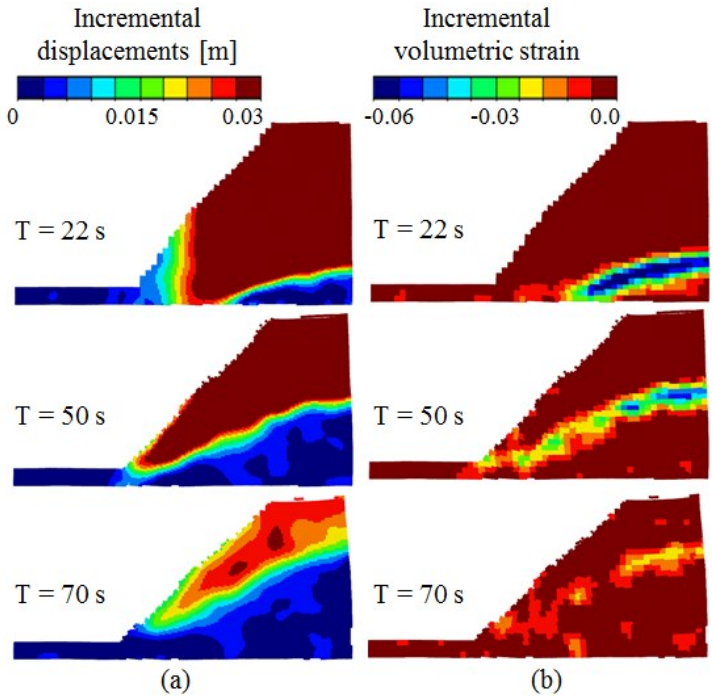

Figure 2.15: Wetting stage. (a) Post-processed incremental displacements $[m]$; (b) Incremental volumetric strains.

During the wetting process, water injected from the bottom of the slope went up through the silty soil and through the gravel column. A horizontal flow from the gravel column (quickly saturated) into the soil is also observed. The wetting front in time can be clearly distinguished because of the change in the colour of the sand between unsaturated and saturated states. The wetting-induced slope deformation is shown in Figure 2.15. The volumetric compression strains due to

the collapse of the soil are concentrated in the material becoming saturated and displacements are observed only in the zone above the wetting front which settles as a rigid block.

Figures 2.16a and 2.16b show the evolution during the test of a normalised total displacement and velocity, respectively, of a numerical particle located at the edge in the top of the slope. The first peak in velocity plot is the movement due to collapse of the soil and the second peak is the slope failure.

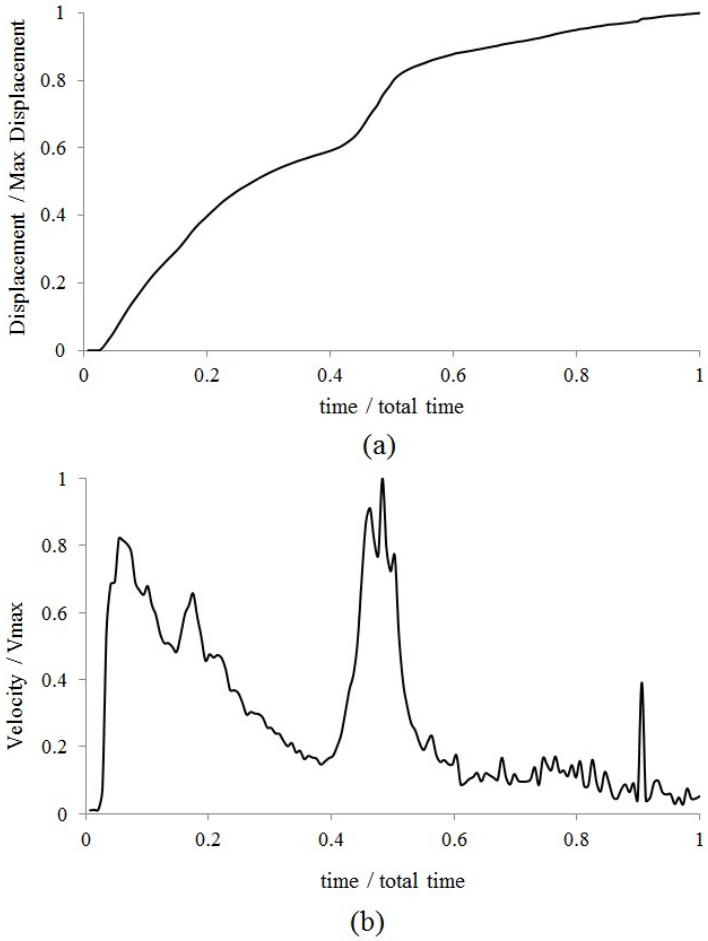

Figure 2.16: Evolution during the test of the numerical particle located at the edge in the top of the slope for (a) Normalised total displacements; (b) Normalised velocity.

Finally, the wetting induce the failure of the slope (Fig. 2.17) due to effective stress reduction and loss of suction. There is a time interval where collapse and shear deformation occurs at the same time. The failure surface is located in the

wetting front. From Figure 2.17b, it can be identified two principal shear surfaces, the first, which is the main shear band, is a circular one that defines the superficial motion of the slope and is the principal, and a second surface located deeper that is also appreciated in the laboratory test.

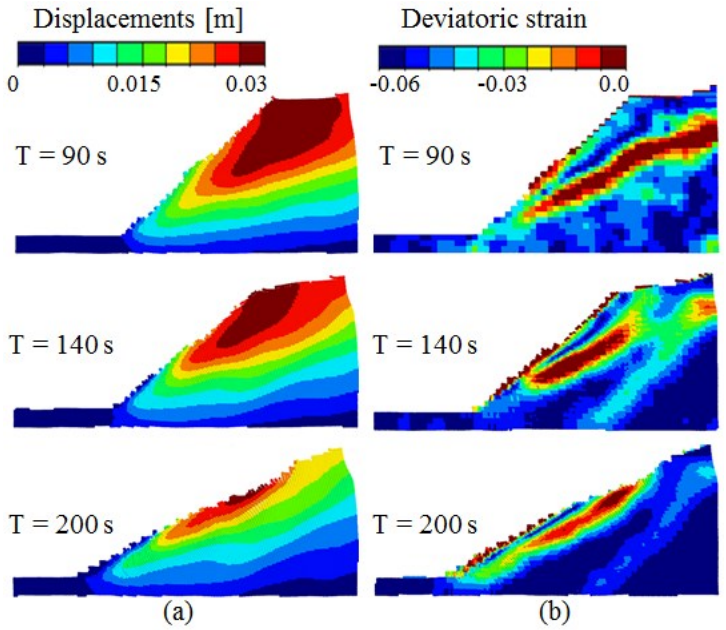

Figure 2.17: Failure stage. (a) Accumulated displacements $[m]$; (b) Deviatoric strain.

2.5 Concluding remarks

A novel procedure to interpret PIV results is described with the purpose of generating a comprehensive identification of kinematic variables of a deforming continuum. The method relies on a combination of Eulerian and Lagrangian interpretation of the incremental displacements provided by PIV techniques in a set of fixed spatial points that cover the whole domain where the deforming body is moving (the region of interest). The key idea was to discretize the mass moving across the reference Eulerian frame by a set of "numerical particles". Measurements of displacement increments from PIV in the nodes of the fixed mesh are interpolated by means of mapping functions (also used in finite elements). The displacements are then assigned to the numerical particles that move through the mesh. Strains are calculated in the numerical particles from the displacement increments of the nodes. Other variables of interest such as velocity and acceleration can be also

stored in the numerical particles.

The method, compared with other available procedure, is especially well suited to interpret scaled laboratory test of granular material involving large displacements. The method may be used in connection with currently available PIV software packages.

The capability of PIV-NP has been shown for the case of a scaled silty clayey slope failure carried out in a centrifuge machine.

Regarding PIV limitations, any type of soil could be used for the analysis while the texture has enough contrast. Rapid motion requires a camera with high shutter speed, otherwise the correlation between two subsequent images cannot be reached. The resolution of the images is directly related with the accuracy of the measurements. Small interrogation areas and small mesh size, increase the error in the precision of the method. These limitations of PIV affects the capability to capture the observed behaviour of the body, but in any case, PIV-NP reproduce very well the data obtained.

The methodology presented allowed the identification of the strain and displacement field at the different stages of the experiment (wetting, collapse and failure). The method provides the numerical value of several variables in a massive way, which is for great interest to be compared with numerical results to validate numerical tools. In particular, PIV-NP is very useful to evaluate and validate MPM numerical results because numerical particles representing small portion of granular material in the laboratory test could be identified as material points in the MPM calculation. Such comparison is presented in the next chapter of this thesis.

3

Chapter 3

MPM Modelling of Scaled Laboratory Test

Modelling small-scale experiments and well-instrumented real cases is an interesting way to validate numerical codes and to evaluate their capabilities and limitations. Laboratory experiments present some drawbacks in the study of real phenomena due to the difficulty of reproducing the actual conditions of the field and the scale effects. However, regarding the validation of numerical tools, scaled laboratory experiments are very useful since the materials, geometry and boundary conditions are controlled. In addition, simulating reduced geometries allow reducing the computational cost involved in modelling real cases.

3.1 Introduction

The method presented in Chapter 2 called PIV-NP is especially useful to compare experimental measurements with MPM numerical results. The variables from the numerical model stored in material points can be directly compared with the experimental measurements obtained by means of the PIV-NP. In this chapter, two scaled laboratory test of slope failure are simulated in MPM in order to evaluate the capabilities of the code and the numerical results are compared with

the PIV measurements processed with PIV-NP

The instability of the slopes was recorded with a digital camera with appropriate resolution and frame rate. The images were processed using PIV technique (Thielicke and Stamhuis, 2014) to obtain the displacement vectors of pre-selected points. From the measured displacements in time, velocities and strains were calculated by means of PIV-NP. The experiments was modelled by means of the MPM Geopart code to characterized the initiation of the failure and the post-failure response, which involves large displacements.

With the aim of modelling the soil behaviour, a Mohr-Coulomb model was implemented in the MPM code following the substepping procedure proposed by Sloan (1987), in which the elastoplastic deformations are integrated in an explicit scheme by means of subdividing the increment of deformation looking for minimizing the error. The modification of the Mohr-Coulomb law, presented by Abbo and Sloan (1995) to avoid gradient discontinuities of yield surface criterion, were also included in the implementation of the constitutive model.

The scaled laboratory slope failures analysed have two main characteristics differentiating them; the triggering condition and more importantly, the scale of gravity acceleration applied to each one. The first case presented here wass performed under $1g$ of gravity acceleration force and the failure was triggered by a removing a constraining wall holding the slope face. The second case is a slope built in a centrifuge machine where $50g$ of gravity acceleration was applied and the failure was achieve by imposing and incremental load on the top of the slope.

Centrifuge modelling is a valuable geotechnical tool to avoid problems of reduced scaled model and to obtain an extrapolate result of a full-scale prototype by reproducing confining stresses more similar to the ones in a real slope in field, by increasing the gravity acceleration (Caicedo and Thorel, 2014)

3.2 Slope failure induced by removing an inclined retaining wall under "$1g$" conditions

3.2.1 Test description

This study case is the failure and run-out of a 60° sand slope in dry conditions carried out in the soil mechanics laboratory of the UPC (Barcelona, Spain) (Pinyol

et al., 2017b). The granular soil is a calcareous-siliceous sand from Castelldefels beach (Catalonia, Spain). The slope was built in a transparent and instrumented box. The slope dimensions are 250 mm height, 200 mm width and 330 mm long (Fig. 3.1a). In the case presented here, the slope is initially stable because an inclined guillotine is restraining the motion. Failure is triggered by removing this guillotine. The landslide motion lasts 0.5 seconds after removing the guillotine. The final stable geometry is shown in Figure 3.1b.

The test was recorded in a 50 fps Full HD video using a reflex camera with shutter manual control. A sequential scheme was selected to correlate each image with the previous one. Quadrilateral patches of 0.0075 $\times$ 0.0075 m were selected for the analysis.

Figure 3.2a shows the instantaneous velocity measured by PIV at three different times. The grid of patches centres is indicated by red crosses. The equivalent instantaneous velocity field plotted by the PIV-NP code are also indicated in Figure 3.2b. A mesh of rectangular elements whose nodes are located in the centres of patches has been selected. Four numerical particles per element were defined. The deformed slope, obtained by PIV-NP code, is plotted using the accumulated displacements of numerical particles, representing physical volumes. Once PIV measurements are processed, displacements, velocities, accelerations and strains are available for each numerical particle defined at each time step during the recorded motion.

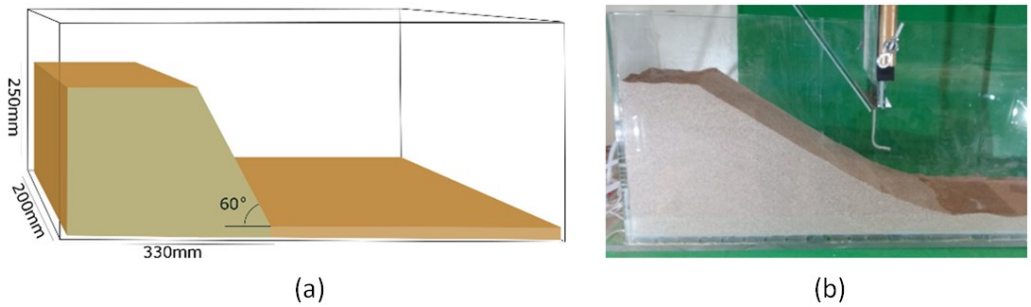

Figure 3.1: (a) Diagram of the selected case study; (b) Photograph of the slope at equilibrium after failure. Pinyol et al. (2017b)

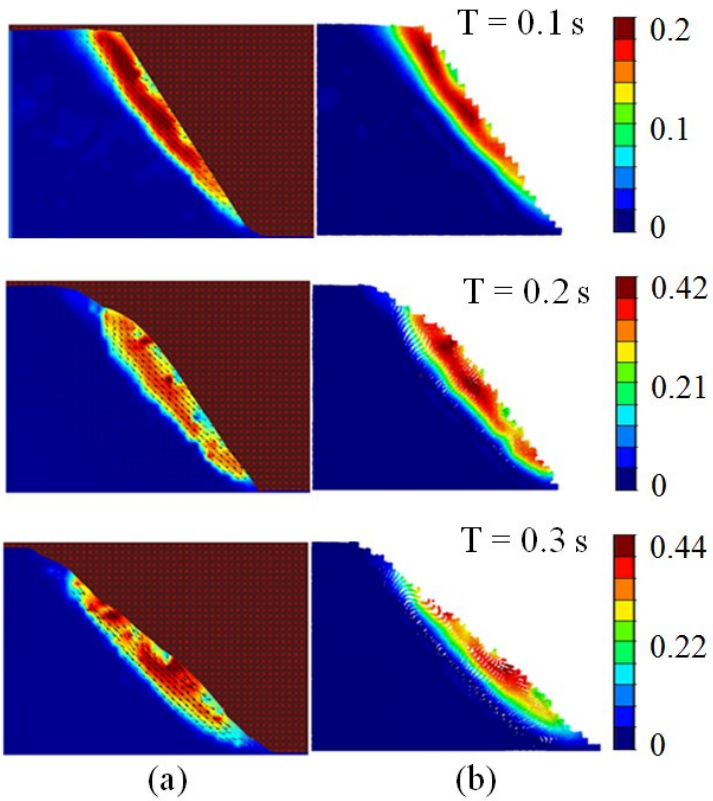

Figure 3.2: Contours and vectors of velocities in m/s at different times (indicated in the figures). (a) Measured by means of PIV-Lab (Thielicke and Stamhuis, 2014) in the centres of patches; (b) reproduced by PIV-NP code.

3.2.2 MPM simulation

The slope simulation is perform under the assumption of a plane strain ($2D$) formulation. The MPM model was created using the same mesh size defined in the PIV analysis and four material points per element are used for the discretization. The boundary conditions imposed in the base suppress the motion in x and y axis, while in the lateral faces only the y axis restriction is applied. In order to simulate initial conditions, zero displacements in the y axis direction are also applied in the slope surface when the gravity load is applied. The failure triggering was reproduced by removing the constrains acting in the slope surface.

The constitutive behaviour of sand is simulated as a one-phase material (dry soil) with the Mohr-Coulomb model implemented. Sand density is measured as an average value taking into account the volume of the slope and the total weight of

Table 3.1: Sand Properties.

Parameters	Value	Units
Sand density	1545	kg/m³
Grain density	2665	kg/m³
Porosity	0.42	-
Poisson's coefficient	0.3	-
Young's modulus	30	MPa
Cohesion	0	kN
Friction angle	43°	-

the material. The maximum and minimum density of the sand measured in the laboratory by a standard procedure (UNE 103-105-93) are 1795 kg/m^3 and 1442 kg/m^3, respectively. An average relative density of 28% is calculated for the sand used in the experiment.

The sand was previously tested in a conventional direct shear test to evaluate the strength. A friction angle equal to 30° was measured in the range of $50-200$ kPa of vertical stress and a nil value for cohesion was obtained. A higher friction angle (43°) has been considered in the MPM simulation which has been calibrated by back analysis to fit better the observed post-failure behaviour of the slope. An increment of the friction angle with respect to the value measured in the direct shear tests can be explained because of the low value of the stress actually acting on the failure surface (Sture et al., 1998, 2009). The failure surface observed in the experiment is located at few centimeters deep which involves a vertical stress lower than 2 kPa. This value is close to two orders of magnitude lower than the stress applied in the laboratory tests, where a friction angle equal to 30° was measured.

Sture et al. (1998, 2009) indicates that the operating sand friction in scaled 1g test performed in the laboratory should be substantially larger than the value measured in standard shear box tests. The back analysed friction by fitting MPM results is consistent with the mentioned data. Note also that the calculation code used does not consider the non-linearity of the strength envelope expected at low confining stresses. Sand's properties for model's parameters introduced in the MPM calculation are indicated in Table 3.1.

In addition, the friction angle (43°) introduced in calculations coincides with the average slope angle of the final geometry in the upper part of the slope once the slope stabilizes after failure. This can be observed in Figure 3.3a where the final slope geometry is plotted once the equilibrium is restored. In the figure,

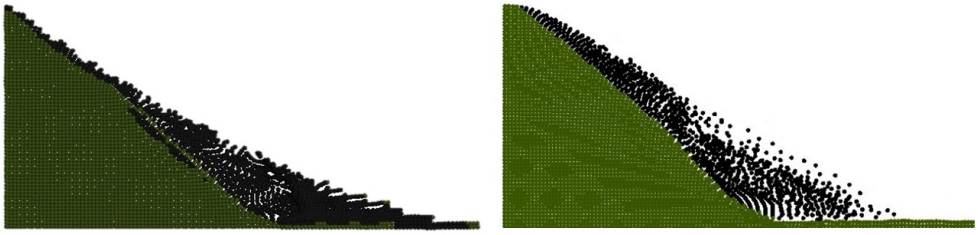

Figure 3.3: Final geometry. The mobilized material is indicated in black. Green colour indicates the material than remains at rest. (a) PIV-NP post-process measurements; (b) MPM results.

two colours are selected to distinguish the material mobilized during the landslide with respect to the material that remains at rest. The slope angle of the material at rest is also equal to 43°.

The final geometry (Fig. 3.3a) can be compared with calculated results plotted in Figure 3.3b. The calculated volume of the material which did not move is similar to the volume observed in the experiment. On the contrary, the final geometry of the mobilized material is not fully captured because in the model, sand accumulates in the central and upper parts of the slope which is a result not observed in the experiment.

Even if the observed and calculated final geometry differs from each other, the evolution in time for both geometries match quite well for the first half of the test (Fig.3.4 and Fig. 3.5). In the final seconds of the slope motion, the sand particles were sliding over the smooth base glass and no visible shear band could be observed at this contact. This "zero thickness" slip motion is difficult to capture by the PIV and moreover, the numerical approximation of MPM used in this work is unable to reproduce this motion. A consequence is a reduced calculated run-out, if compare with measurements.

The equilibrated average sand slope in the experiment was 26° (measured in Figure 3.3a) while the calculated value was 31° (measured in Figure 3.3b).

The time evolution of accumulated displacements at three material points is plotted in Figure 3.5. Numerical results are compared with values calculated from PIV measurements once post-processed by PIV-NP. The agreement is reasonably good. Once again, differences can be observed at the point nearest the surface during the test's final half.

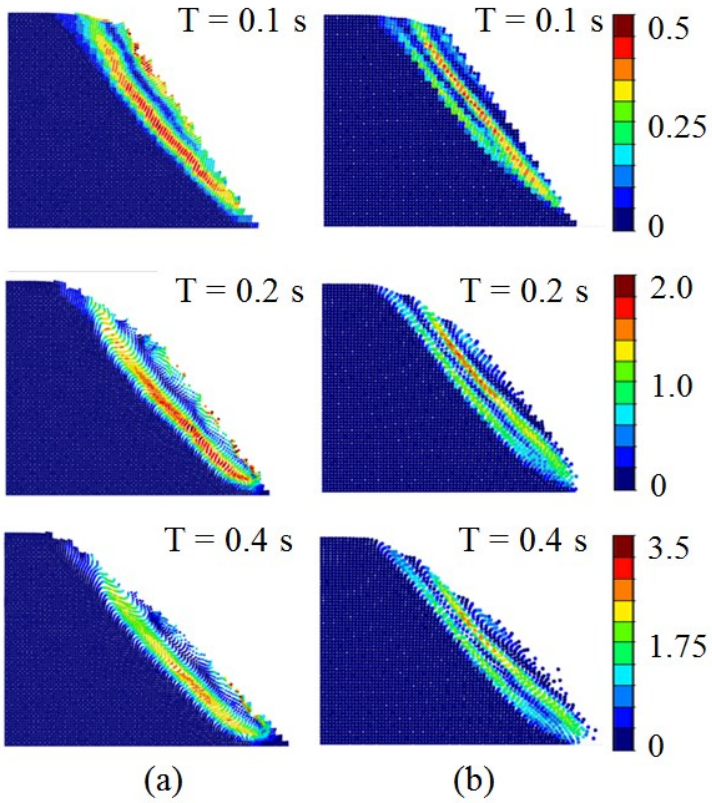

Figure 3.4: Deviatoric plastic strain. (a) Post-processed PIV-NP results; (b) MPM simulation results.

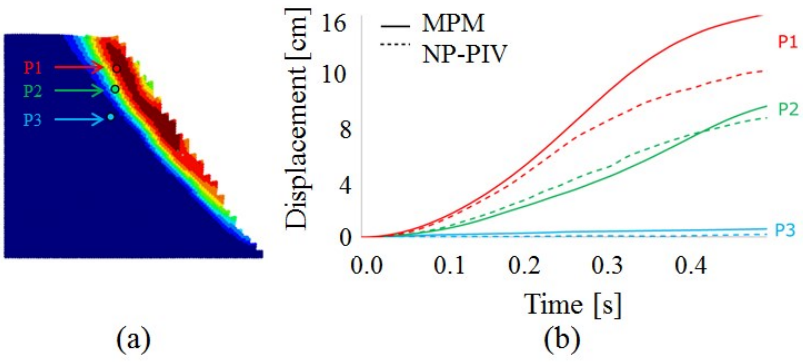

Figure 3.5: Accumulated post-failure displacements of three points in the slope. (a) Position of the selected points; (b) Comparison of MPM results and PIV-NP post-process experimental observations.

A possible explanation to the described discrepancies could be due to the MPM natural "sticky" contact between material points. In MPM the soil is modelled as a continuum medium with numerical interaction between adjacent subdomains. This characteristic adds an artificial, numerical cohesion to the medium by the interaction between material points at nodes; two material points are not fully decoupled until there is at least, one empty mesh element between them. This numerical issue could be interfering with superficial zero thickness sliding material and also with the lower part of the slope where the real boundary condition allows free motion (material slides over glass).

Making the assumption that sand exhibits small or near null elastic deformations, the strains obtained from PIV-NP can be considered directly as plastic strains and deviatoric plastic strain (ε_d^p) can be obtained. The deviatoric plastic strains field was plotted in Figure 3.4a for PIV-NP results and in Figure 3.4b for MPM simulation results at three different times. PIV-NP measurements are compared with MPM numerical results.

A unique shear band is observed in the experimental results whereas numerical calculation indicate that shear strains localize in two shear bands that develop simultaneously (Fig. 3.4). This discrepancy is probably associated with the complex behaviour of sand at very low confining stresses (non-linear strength envelope) (Sture et al., 1998, 2009) which are features not reproduced by the standard elastoplastic Mohr Coulomb model used.

3.3 Bearing capacity of scaled slope in centrifuge machine under $50g$ conditions

3.3.1 Test description

A sand slope model was carried out in the centrifuge machine of the geotechnical laboratory of the University of Andes in Bogotá (Colombia) (Ruiz et al., 2017a). The slope was built in a transparent box with sand from Guamo (Tolima, Colombia). The initial slope inclination was 32°. After slope construction, the centrifuge flight started increasing the gravity until $50g$ which corresponds to an increase the scale of dimension 50 times larger. The dimensions of the slope are indicated in the Figure 3.6. The so called slope model refers to real laboratory dimensions of the slope (Fig. 3.6a), while the slope prototype refers to scaled dimensions of the slope according to the gravity acceleration applied (3.6b). Therefore, the 7 cm

height of the slope model are equivalent to 3.5 m in the slope prototype.

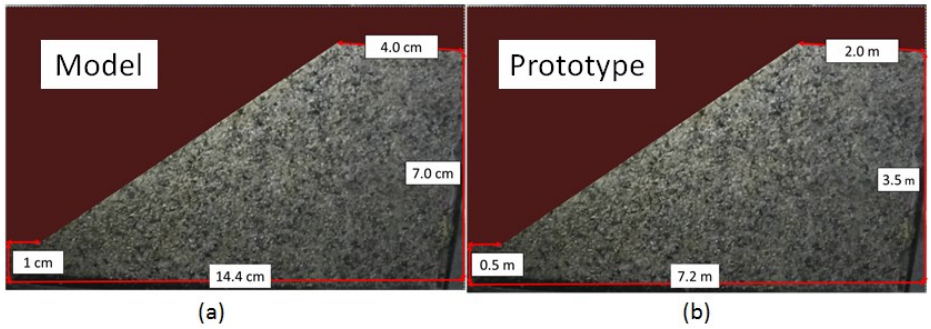

Figure 3.6: Sand slope after construction in the transparent box located inside the centrifuge machine. (a) Model $1g$; (b) Equivalent dimensions in prototype $50g$. (Ruiz et al., 2017a)

During the centrifuge flight, an imposed load with a rotational piston on the top of the slope was increased until failure. The time elapsed until slope failure was 40 seconds. After reaching failure conditions, the rotational piston applying the surface load reached its maximum limit of vertical displacement and the slide stops.

The whole motion of the slope was recorded with a digital camera taking 1 picture per second and images where interpreted with PIV technique. Taking into account the possibility of scaling dimensions according to the gravity accelerations applied, two quadrilateral patches of 1.6×1.6 mm for the slope model and 80×80 mm for the slope prototype were selected for the PIV-NP analysis. It is important to highlight that the accuracy of the method depends on the relation between total number of mesh elements and the size of the domain. Then, both cases, model and prototype will provide the same results because the mentioned correlation is kept equal.

3.3.2 MPM simulation

The slope modelling was perform under the assumption of plane strain ($2D$) formulation. The MPM discretization was created following the same mesh size defined for the slope model and the slope prototype in the PIV-NP post-process. Nine material points per mesh element was used (Fig. 3.7). The boundary conditions imposed in the base includes motion constrains along x and y axis. Both, the lateral sides of the domain have the motion in y axis restricted. The initial conditions are reached after applying the gravity acceleration force for each case

($50g$ for slope model dimension and $1g$ for slope prototype dimensions). In order to simulate the triggering condition for the slope failure, a rigid body is located on top of the slope (Fig. 3.7) and its density was increased, reproducing the same rate of the applied incremental load in the laboratory test.

Table 3.2: Sand Properties.

Parameters	Value	Units
Sand density	1755	kg/m³
Grain density	2700	kg/m³
Porosity	0.35	-
Poisson's coefficient	0.3	-
Young's modulus	30	MPa
Cohesion	0	kN
Friction angle	35°	-

The sand is simulated as a one-phase material (dry soil) with the Mohr-Coulomb constitutive model implemented. Sand density is measured as an average value taking into account the volume of the slope and the total weight of the material. The sand was tested in a conventional direct shear test to evaluate the strength. A friction angle equal to 35° was measured and nil value for cohesion was obtained. Other parameters required for the simulation were assumed based in the previous case. Parameter are indicated in Table 3.2.

MPM simulations were made for the slope model as well as for the slope prototype. As expected, results obtained in both simulations were exactly the same due to the same mesh proportion (element size / mesh size), number of elements and number of material points per element for each case. The confining stresses, boundary conditions, initial displacements and strains and the destabilizing load per unit of volume are the same for both cases. Then, the results presented here can be interpreted as the results for either of them. Values for displacement are presented for slope prototype and must be divided by 50 in order to obtain the values corresponding to the slope model.

The deformed geometry and the total displacement field obtained by PIV-NP are plotted in Figure 3.8a, the MPM results are given in 3.8b, for three different times. The time to reach the final stage was 40 seconds. The values obtained with the simulations are quite similar to the obtained from the laboratory test and the final geometry is almost the same. The maximum displacements are around 40 *cm*.

Making the same assumption as previous case, elastic strain in sands can be considered negligible. Then, measured deformation can be interpreted as plastic

deformations and deviatoric plastic strains (ε_d^p) can be calculated. Figure 3.9 compares PIV-NP measured and MPM computed deviatoric plastic strain at different times. Shear strains in the test are located in a wide sheared zone, while in MPM simulations localized in a thin shear band. However, the MPM model results is remarkably good providing the path of shear strain localization processed with PIV-NP.

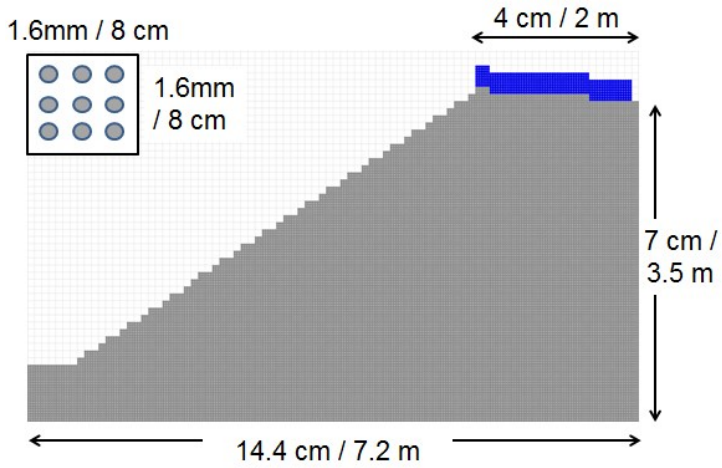

Figure 3.7: MPM discretization of the slope. Mesh and element size for (model / prototype)

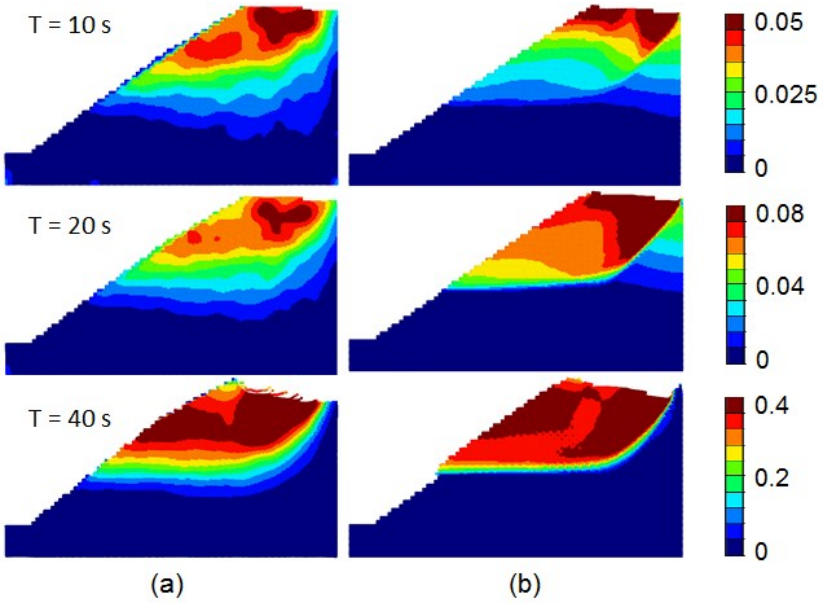

Figure 3.8: Total displacements [m] at different times. (a) PIV-NP measurements; (b) MPM simulation results.

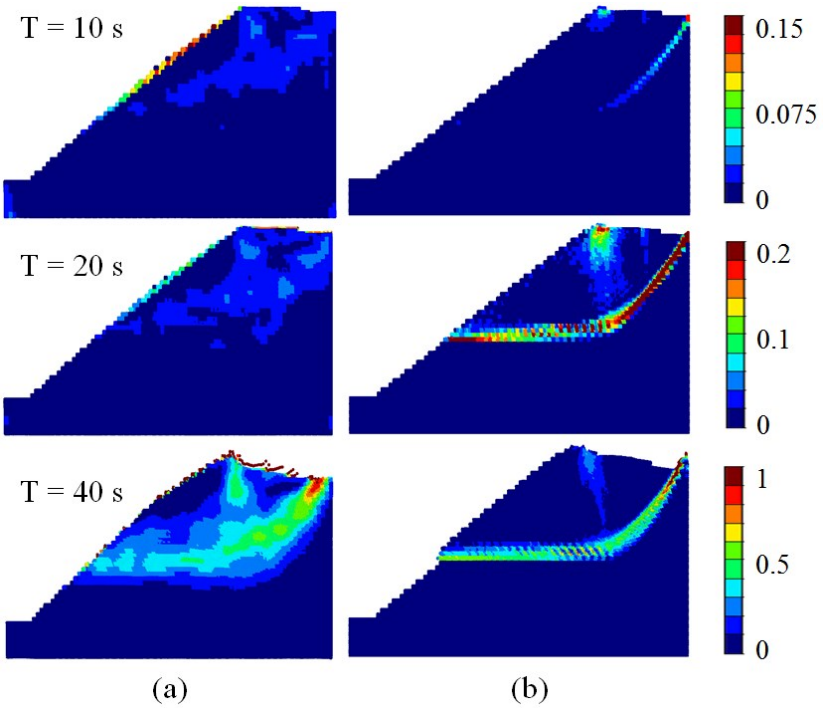

Figure 3.9: Shear deviatoric strain ε_d^P at different times. (a) PIV-NP measurements; (b) MPM simulation results.

3.4 Concluding remarks

The study cases presented in this chapter illustrate the capability of the PIV post processing method PIV-NP, described in Chapter 2, to interpret the response of slope failures. The method provides time evolution of displacements, velocities, accelerations and strain fields. The laboratory test were simulated in MPM, modelling the sand with a Mohr-Coulomb constitutive model. The variables obtained by PIV-NP were directly compared with MPM results.

Shearing behaviour of sand at very low normal stresses typical of small scale $1g$ experiments is rather complex and this observation probably explains some discrepancies highlighted in the first slope failure case. Despite this, the MPM provides results reasonably good in terms of geometry, displacements and shearing surfaces.

The first case can be understood as an experiment of a slope failure and also as a column collapse. The numerical simulation is complex (Pouliquen, 1999) due to transition from solid-like to fluid-like behaviour and the low stresses. Taking into account this, it is possible that a Mohr-Coulomb constitutive model is not the most accurate way to simulate the soil behaviour. In addition, field measurements indicate a compressive behaviour during shearing of the loose sand that was not compacted during experiment preparation. This compressive response is not capture by the MPM simulation with Mohr-Coulomb.

In case of the centrifuge test, the sand is densified when the gravity acceleration ($50g$) in applied and the compressive behaviour is not observed.

The MPM simulation of the slope in the centrifuge machine under $50g$ presents good reproduction of the real behaviour observed during the test and matches the results processed with PIV-NP. The increasing load produces a superficial shearing surface and the MPM simulation reproduce very well its evolutionary geometry.

4

Chapter 4

Thermo-Hydro-Mechanical Coupling for saturated soils in MPM

This chapter describes a thermo-hydro-mechanical formulation to model thermally-induced effects due to the irreversible work input generated during the soil deformation. The governing equations of the phenomena were discretized and implemented into a Material Point calculation procedure. The method is applied to the analysis of landslides. A simple slope stability is analysed. Mechanical work essentially dissipates in shearing bands inducing excess pore water pressures that, eventually, reduce the effective strength. The marked effect of soil permeability to control the slide motion after failure is described. Shear band thickness is also a relevant control variable. The problem posed by the non-realistic thickness of shear bands in numerical calculation is addressed by means of a novel numerical procedure that includes the consideration of embedded shear bands where the strains are assumed to be localized. Balance equations describing local flow and thermal interactions between shear bands and the remaining material are formulated.

This chapter is part of the published paper "Thermal effects in landslide mobility (2017)" (See list of publication)

4.1 Introduction

One of the mechanisms invoked to explain the rapid acceleration eventually observed in landslides is the heating of shearing bands induced by the mechanical energy dissipated during sliding. It leads to thermal-induced dilation of solid particles and water filling the pores in saturated soils which, in turn, leads to increments of pore water pressure essentially dissipated as flow from the shear band towards the surrounding soil. As a result, effective frictional resistance forces reduce and the landslide accelerates.

The idea of explaining fast sliding due to heating generated by frictional work was first introduced by Habib (1967) who explained that the rapid motion of Vajont landslide was a consequence of the vapour pressure generated in the sliding surface. Later, Uriel and Molinia (1977) combined a limit equilibrium model and the heat-induced water pressure to explain Vajont rapid motion. Voight and Faust (1982) were the first to formulate the physics of the problem by combining the mass and heat balance equations inside the shear band and the dynamic equilibrium of the moving mass. Further contributions (Alonso et al. (2016); Cecinato and Zervos (2012); Cecinato et al. (2011); Goren and Aharonov (2007, 2009); Goren et al. (2010); He et al. (2015); Pinyol and Alonso (2010a,b); Vardoulakis (2000, 2002); Veveakis et al. (2007)) followed Voight and Faust (1982) pioneering development and introduced additional improvements. They concluded that the generated excess pore pressures were able to explain the acceleration of landslides.

The mentioned contributions share two simplifications: (a) the slope kinematics are solved in simple geometries defined by interacting solid blocks. Often the motion is simply defined by a rigid body motion of a block sliding on a planar surface; and (b) dissipation of the mechanical work is concentrated in shear bands defining the contacts between rigid bodies.

These restrictions have been removed in the work reported in this thesis with the purpose of generalizing the basic concepts and, also, with the ultimate aim of exploring the implications of thermally induced pore pressures on the vast majority of landslides, irrespective of its size, kinematic deformation mechanisms or assumptions concerning the dominant mode of energy dissipation. To do that, the dynamic behaviour of saturated soil under non-isothermal conditions has been formulated and integrated in Material Point Method framework.

The numerical analyses of the dynamic behaviour of porous media have been approached under different assumptions. For the case of and isothermal conditions, Verruijt (2010) and Zienkiewicz and Shiomi (1984) developed the governing equa-

tions based on the theoretical basis presented by Biot (1941, 1962) and Prevost (1980). Later, numerical approaches were formulated in Finite Elements (FEM) by Pastor et al. (1990), Huang et al. (2004), Jeremic et al. (2008) and Gajo and Denzer (2011), among others. The general "$u - w$" approach (a notation which refers to the displacement of the solid and the relative fluid displacement, respectively) can be reduced to the "$u - p$" formulation (where p is the pore water pressure) when material derivatives of the relative acceleration of the fluid with respect to solid is neglected (Lòpez-Querol et al. (2008); Zienkiewicz et al. (1999); Zienkiewicz and Shiomi (1984)). The $u - p$ formulation is able to capture the dynamic response for low frequency phenomena.

Zienkiewicz et al. (1999), Schrefler and Scotta (2001) and Uzuoka and Borja (2012) extended the formulation to partially saturated soils. The non-isothermal dynamic analysis for non-saturated porous media ($u-p-T$ approach) has been published by Cao et al. (2016). They included vapour pressure below the saturation water pressure (cavitation) and the evaporation of the pore liquid water due to thermal loads. Some application examples, solved by FE, involve small strains.

In this work, the $u - p - T$ formulation has been developed for saturated porous media without including evaporation. In the cases and applications analysed here, the evaporation of the pore liquid pressure is not expected because of the range of temperatures developed. The governing equations have been solved and discretized numerically in MPM with the aim of simulating the transition from static to dynamic conditions of landslides and the expected motion after failure. The $u-p$ formulation presented by Zhang et al. (2009) and Zabala and Alonso (2011) is extended to non-isothermal conditions by including the energy balance equation and by applying the assumption that the mechanical plastic work generated dissipates in heat. The fundamental phenomena are highly coupled: (a) Plastic work and, therefore, thermal effects in the entire calculation domain are the result of sliding kinematics and the particular constitutive model; (b) Pore pressures are a consequence of the rate of temperature changes, but also on their dissipation in real time because of flow effects; (c) Pore pressures and temperature modify the stress paths and the constitutive equations. These effects will be highlighted in the cases described.

The resulting MPM $u - p - T$ approach is capable of removing the limiting assumptions used so far to explore the thermal pressurization effects on landslides. In fact, the kinematics of the motion should not be an assumption made"a priori" but part of the solution. In general, heat sources are generated wherever plastic work develops.

4.2 Basic governing equations

The equations are expressed in terms of the following primary unknown variables: acceleration of solid particles ($\mathbf{a}_S$), liquid pressure (p_L) and temperature (θ). Relative acceleration of the liquid with respect to the solid skeleton is assumed negligible ($\mathbf{a}_{L/S} = \mathbf{a}_S - \mathbf{a}_L = 0$; $\mathbf{a}_S = \mathbf{a}_L$). The formulation is then simplified to a $u - p$ formulation commonly used in finite-element implementation.

4.2.1 Momentum balance of the mixture

The equation of motion is formulated for both fluid and solid particles assuming the saturation of pores.

$$\rho \mathbf{a}_S = \nabla \cdot \sigma + \rho \mathbf{b} \tag{4.1}$$

where $\mathbf{a}_S$ is the acceleration of the solid skeleton, σ is the Cauchy stress tensor, $\mathbf{b}$ the body forces vector, and ρ is the density of the mixture defined as: $\rho = n\rho_L + (1-n)\,\rho_S$, where n is the porosity and ρ_L and ρ_S are the fluid and solid density respectively. indicates the divergence vector operator.

4.2.2 Conservation of momentum of fluid

From the dynamic equilibrium equation for the fluid, the following generalized equation for Darcy flow rate, $\mathbf{q}_L$, can be obtained:

$$\mathbf{q}_L = -\frac{K}{\gamma_L}\left(\nabla p_L - \rho_L \mathbf{b} + \rho_L \mathbf{a}_L\right) \tag{4.2}$$

where ∇p_L is the gradient of pore water pressure, γ_L is the specific weight of liquid and K is the permeability, also called hydraulic conductivity.

4.2.3 Mass balance of mixture

The mass balance equation of both solid particles and liquid can be expressed as follows:

$$n\frac{D\rho_L}{Dt} + \frac{\rho_L}{\rho_S}(1-n)\frac{D\rho_S}{Dt} + \rho_L \nabla \cdot \mathbf{v}_S + \nabla \cdot (\rho_L \mathbf{q}_L) = 0 \tag{4.3}$$

where the material derivative is defined with respect to the solid as $\frac{D(\cdot)}{Dt} = \frac{\partial(\cdot)}{\partial t} + \mathbf{v}_S \nabla(\cdot)$. The Darcy's flow $\mathbf{q}_L$ in Equation (4.3) has been defined in Equation (4.2).

Constitutive equations defining the variation of solid and liquid density are now introduced with the aim of expressing the governing equations in terms of the primary unknown variables. Exponential functions have been selected to define the density variations:

$$\rho_S = \rho_S^0 \exp\left[-\beta_S\left(\theta - \theta^0\right)\right] \tag{4.4}$$

$$\rho_L = \rho_L^0 \exp\left[\alpha_L\left(p_L - p_L^0\right) - \beta_L\left(\theta - \theta^0\right)\right] \tag{4.5}$$

where ρ_S^0 and ρ_L^0 are the solid and liquid density at reference temperature θ^0 and liquid pressure p_L^0. The parameter α_L defines the liquid phase compressibility and β_S, β_L are the volumetric thermal expansion coefficients for solid and liquid phase, respectively. The compressibility of the solid particles against changes in stress is assumed negligible.

Taking into account Equations (4.4) and (4.5), assuming constant constitutive parameters and assuming the distribution of the water density sufficiently smooth, the following mass balance equation is obtained:

$$n\alpha_L \frac{Dp_L}{Dt} - \beta\frac{D\theta}{Dt} + \nabla \cdot \mathbf{v}_S + \nabla \cdot \mathbf{q}_L = 0 \tag{4.6}$$

where a volumetric thermal expansion coefficient for the mixture $\beta = (1-n)\beta_S + n\beta_L$ is introduced.

Note that the spatial variation of the liquid density is neglected ($\nabla \rho_L \approx 0$).

4.2.4 Energy balance of mixture

The internal energy balance per unit of volume can be written as:

$$\begin{array}{l} \frac{D}{Dt}\left[\left(n\rho_L c_L + (1-n)\,\rho_s c_s\right)\theta\right] + \nabla\cdot\left[-\Gamma\nabla\theta\right] + \\ \nabla\cdot\left[\rho_L c_L \theta(\mathbf{q}_L + n\mathbf{v}_S) + (1-n)\,\rho_s c_s \theta \mathbf{v}_S\right] = \dot{H} \end{array} \tag{4.7}$$

which states that the external supply of heat rate, $\dot{H}$,should be equal to the sum of the following terms: (a) internal energy in solid and liquid phase which depends on their specific heats, c_s and c_L, respectively; (b) the heat flow conduction driven by temperature gradients (Fourier's law) which depends on the thermal conductivity coefficient, Γ; and (c) the convective heat transport due to liquid and solid flows.

Assuming that the specific heat of the phases remains constant, Eq. (4.7) can be simplified to:

$$(\rho c)_m \frac{D\theta}{Dt} + \nabla\cdot\mathbf{q}_h + \rho_L c_L \theta\nabla\cdot\mathbf{q}_L + (\rho c)_m \theta\nabla\cdot\mathbf{v}_S = \dot{H} \tag{4.8}$$

where the specific heat of the mixture has been defined as $(\rho c)_m = n\rho_L c_L + (1-n)\,\rho_s c_s$ and

$$\mathbf{q}_h = -\Gamma\nabla\theta \tag{4.9}$$

is the heat flow conduction.

4.2.5 First law of thermodynamics

It is assumed that the plastic work,

$$\dot{H} = \sigma' : \dot{\varepsilon}^p \tag{4.10}$$

dissipates in heat. In Equation (4.10),

$$\sigma' = \sigma - p_L \mathbf{m} \tag{4.11}$$

is the effective stress tensor, $\mathbf{m}$ is defined by means of $m_{ij} = \delta_{ij}$ and δ_{ij} the Kronecker delta. $\dot{\varepsilon}^p$ is the plastic strain rate.

4.2.6 Constitutive equations of the porous media

A constitutive law,

$$d\sigma' = \mathbf{D} \cdot d\varepsilon \tag{4.12}$$

where $\mathbf{D}$ is the tangent matrix and defines the relationship between effective stress and strains. The soil behaviour is characterized by means of an elastoplastic Mohr-Coulomb model. Alternatively, more complex constitutive models could be defined. However, since the main purpose of this work is to model the response of landslides including thermal effects, this is a proper option to simulate the shearing behaviour of soils in first time failures (Yerro et al. (2016a); Zabala and Alonso (2011); **?**). The yield surface is defined in terms of effective cohesion, c', and effective friction angle, ϕ', whose values decrease exponentially with the accumulated deviatoric plastic strain invariant $\varepsilon_d^p = \sqrt{\frac{2}{3} e_{ij}^p e_{ij}^p}$, where e_{ij}^p is the deviatoric part of the plastic strain tensor as follows:

$$c' = c'_{res} + (c'_{peak} - c'_{res})\, \mathrm{e}^{-\eta \varepsilon_d^p} \tag{4.13}$$

$$\phi' = \phi'_{res} + \left(\phi'_{peak} - \phi'_{res}\right) \mathrm{e}^{-\eta \varepsilon_d^p} \tag{4.14}$$

Peak and residual values of cohesion and friction angle indicated by the subindex "res" and "peak", respectively, are model parameters. The rate of the strength decrease is controlled by the softening shape factor η.

4.3 MPM Discretization of governing equations for saturated conditions

The mass of a saturated porous media is discretized by a set of material points representing both the solid and the liquid phase. Each material point represents a portion of the total volume of the porous media and it is assumed that the mass of each volume portion is concentrated in the material point. Therefore, the spatial distribution of the mass density of the mixture in time, $\rho(\mathbf{x}, t)$, can be discretized in the domain following the next expression:

$$\rho(\mathbf{x}, t) = \sum_{p=1}^{N_p} m_p \delta(\mathbf{x} - \mathbf{x}_p) \tag{4.15}$$

where the density is expressed as the sum over the all number of material points, N_p, and m_p is the mass of each material point located at $\mathbf{x}_p$ coordinate. $\delta(\cdot)$ is the Dirac delta function.

4.3.1 Momentum balance equation

The equation (4.1) is solved as a boundary value problem in which displacement, $\hat{\mathbf{u}}(t)$, and tractions, $\hat{\mathbf{t}}(t)$, are imposed in Γ_u and Γ_t, respectively. Applying the Weighted Residual Method (Finlayson, 1972; Finlayson and Scriven, 1966), selecting adequate test function and substituting ρ by the expresion (4.15), integrals over the domain reduces to sums of material points and the following system of equations is obtained:

$$\sum_{j=1}^{N_n} \sum_{p=1}^{N_p} m_p N_i^p N_j^p \mathbf{a}_{S_j} = \int_{\Gamma_t} \rho N_i^p \cdot \hat{\mathbf{t}} \mathrm{d}\Gamma_t - \sum_{p=1}^{N_p} \left(\nabla N_i^p\right) \cdot \sigma_p V_p + \sum_{p=1}^{N_p} m_p N_i^p \mathbf{b}_p \tag{4.16}$$

where the stress tensor has been recovered, N_i^p refers to the shape function associated to the node i and evaluated in the position of the particle p and V_p is the volume associated to the particle p.

4.3.2 Conservation of liquid momentum and mass balance

Replacing equation (4.2) into equation (4.6) and applying the same procedure described for the momentum balance, the equation (4.6) becomes into:

$$\Delta p_{L_i} = -\frac{K}{\gamma_L V_i}\left[\sum_{p=1}^{N_p} N_i^p \left(\beta \Delta\theta_p + \Delta\varepsilon_{vol_p}\right) V_p + \int_{\Gamma_q} N_i \hat{q}_L \Delta t \mathrm{d}\Gamma_q - \sum_{p=1}^{N_p} \nabla N_i^p \cdot \mathbf{q}_p \Delta t V_p\right] \tag{4.17}$$

4.3.3 Energy balance of mixture

The temperature increment is calculated by means of solving the energy balance equation per unit of volume, Eq. (4.8), numerically in the domain Ω described in the following boundary value problem:

$$\begin{aligned} &\Delta\theta(\mathbf{x},t) + \tfrac{1}{(\rho c)_m}\left[\nabla\cdot\mathbf{q}_h(\mathbf{x},t)\Delta t + \rho_w c_w \theta \nabla\cdot\mathbf{q}_L(\mathbf{x},t)\Delta t\right] + \theta\Delta\varepsilon_{vol}(\mathbf{x},t) = \dot{H}(\mathbf{x},t) \\ &\theta(\mathbf{x},t) = \hat{\theta} \ \mathrm{on}\Gamma_\theta \\ &\mathbf{q}_h(\mathbf{x},t) = \hat{q}_h \ \mathrm{on}\Gamma_{q_h} \end{aligned} \tag{4.18}$$

where $\mathbf{q}_L$ and $\mathbf{q}_h$ is defined in equation (4.2) and (4.9) respectively. The temperature and the temperature flow are prescribed in the boundary Γ_θ and Γ_{q_h}, respectively. Applying the Weighted Residual Method, substituting ρ and removing notation $(\mathbf{x},t)$ to simplify. The equation 4.18 becomes:

$$\begin{aligned} \Delta\theta_i = \tfrac{1}{(\rho c)_m V_i}\Bigg[&\sum_{p=1}^{N_p}\left(\nabla N_i^p\right)\mathbf{q}_{h_p}\Delta t\, V_p - \int_{\Gamma_{q_h}} N_i \hat{q}_h \Delta t \mathrm{d}\Gamma + \sum_{p=1}^{N_p}\rho_w c_w \theta\left(\nabla N_i^p\right)\mathbf{q}_p \Delta t V_p - \\ &\int_{\Gamma_{q_L}} \rho_w c_w \theta N_i \hat{q}_L \Delta t \mathrm{d}\Gamma - \sum_{p=1}^{N_p}(\rho c)_m \theta N_i^p \Delta\varepsilon_{vol_p} V_p + \sum_{p=1}^{N_p} N_i^p \dot{H}_p V_p\Bigg] \end{aligned} \tag{4.19}$$

which gives the temperature increment at each node i depending on the variables at particles and boundary conditions.

4.4 Analysis of a reference case

The performance of the THM formulation was first tested by means of a $2D$ numerical stability analysis. Consider in Figure 4.1 the geometry of a homogeneous saturated slope. For this case, the soil is described by a perfectly plastic Mohr-Coulomb model defined by an effective friction angle equal to 28° and an effective cohesion equal to 2.0 kPa. The rest of parameters are indicated in Table 4.1. A square support mesh (12.5 × 12.5 cm) defines the computational domain (also plotted in Fig. 4.1). Four particles per element are initially located at each fill element representing the soil of the slope. The slope failure is triggered by the simple procedure of reducing the cohesion from 2 kPa to 1 kPa.

An isothermal case (no source term in the energy balance equation) defines the reference case. Figure 4.2a shows the accumulated displacement computed at the end of the motion (once the slope recovers a new stable geometry) five seconds after failure triggering. The distance between the initial and the final position of the slope toe is equal to 1.7 m.

According to the previous works published by Goren and Aharonov (2009) and Pinyol and Alonso (2010a,b), heating effects on the landslide motion are highly dependent on the pore water pressure dissipation, mainly controlled by the value of the saturated permeability. In those articles, the problem was analysed for simple geometries and the THM problem was solved at the scale of the shear band coupled with the momentum balance equations defining the whole motion of the unstable mass. The conclusion derived from the sensitivity analyses performed was clear: given a slope, a range of permeability values can be defined which separate rapidly accelerating landslides from non-accelerated landslides. For relatively low values of permeability, excess pore water pressure generated during the motion cannot dissipate and its accumulation induces the acceleration of the landslide, which feeds back the motion. On the contrary, higher values of permeability allow the dissipation of the excess pore pressures and the motion slows down. In this case, when compound landslides are analysed (Pinyol and Alonso (2010b)), changes in the slope geometry during the motion make the slope more stable and, after a certain time, the acceleration reduces and the slide run-out is shorter, if compared with the case of more impervious shearing bands.

Consider now the effect of permeability when thermal effects are activated in the model slope (Fig. 4.2b and 4.2c). The slope response for the more pervious case ($K = 10^{-5} m/s$) does not change if compared with the isothermal case. However, the thermal effects lead to an increased slide run-out in the more impervious case ($K = 10^{-11} m/s$).

The slide motion depends not only on the soil permeability, but also on the shear band thickness because this dimension is involved in the accumulation of plastic work per unit of volume of soil inside the band as well as in the pore pressure and heat dissipation towards the surrounding soil. Shear band thickness in the reference case depends on the size of computational mesh. This introduces a mesh-dependent problem which will be addressed below.

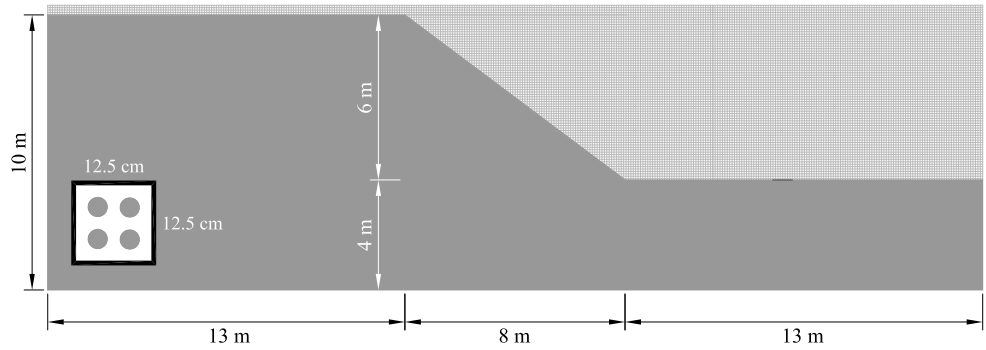

Figure 4.1: Slope geometry and discretisation of the reference case.

Table 4.1: Model parameters

Parameters	Symbol	Value	Units
Water			
Density	ρ_L	1000	kg/m^3
Bulk modulus	α_L	2200	MPa
Thermal dilation coefficient	β_L	0·00034	1/°C
Specific heat	c_L	4186	N m/(kg °C)
		1	cal/(kg °C)
Solid particles			
Density	ρ_S	2700	kg/m^3
Thermal dilation coefficient	β_S	0·00003	1/°C
Specific heat	c_S	837	N m/(kg °C)
		0·2	cal/(kg °C)
Clay Soil			
Porosity	n	0·4	—
Permeability	K	$1{\cdot}00 \times 10^{-11}$	m/s
Young's modulus	E	20 000	kPa
Poisson ratio	ν	0·33	—

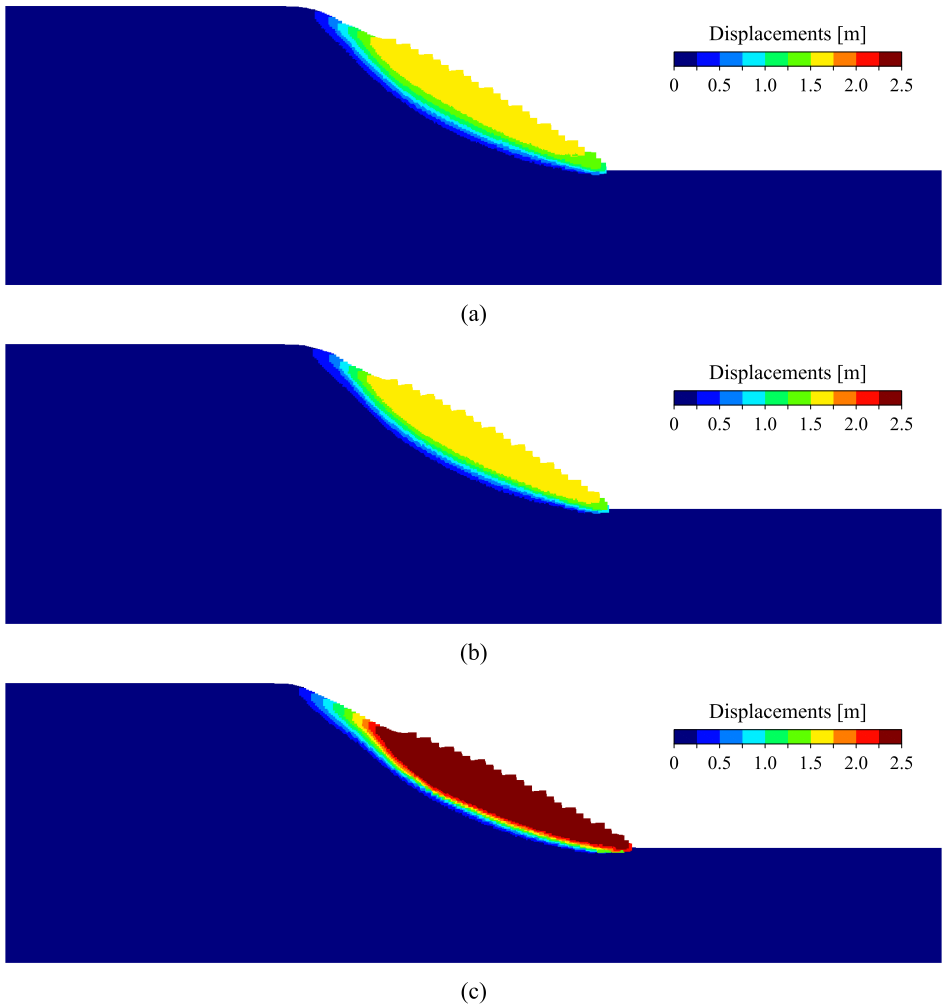

Figure 4.2: Accumulated displacements at the end of the motion for the reference case: (a) heating effects not included; (b) heating effects included and $K = 10^{-5}\ m/s$; (c) heating effects included and $K = 10^{-11}\ m/s$.

4.4.1 Effect of the shear band thickness

Consider he effect of the shear band thickness illustrated by a simple example. Figures 4.3 show two reference volumes subjected to shear deformation defined by a rate of displacement $\dot{\delta}$. It is assumed that the shear band of each sample has a different thickness. For simplicity, a planar deformation is assumed. Accepting a linear distribution of the shear strains inside the sheared zone and assuming that

the soils are at failure, the rate of the generated mechanical work per unit volume can be calculated as:

$$\dot{W}_1 = \tau_f \dot{\gamma}_1 = \tau_f \frac{\dot{\delta}}{h_1} \tag{4.20}$$

$$\dot{W}_2 = \tau_f \dot{\gamma}_2 = \tau_f \frac{\dot{\delta}}{h_2} \tag{4.21}$$

where τ_f is the shear strength, $\dot{\gamma}$ is the shear strain rate and 1 and 2 refers to the reference volumes represented in Figure 4.3. According to this, the dissipated work per unit of volume depends on the thickness of the shear band; however the total work on the band volume will be equal for both cases:

$$\dot{W}_1 h_1 l = \dot{W}_2 h_2 l = \tau_f \dot{\delta} l \tag{4.22}$$

Since temperature increments are computed from the heat generated per unit of volume (Eq. 4.10), higher increments of temperature and pore water pressure are expected in the case of the thinnest shear band (Fig. 4.3c).

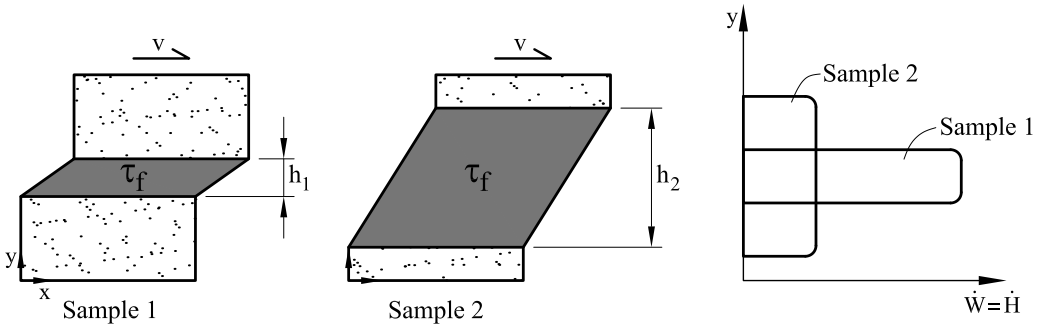

Figure 4.3: Schematic representation of two shear bands exhibiting different shear band thicknesses. Pinyol et al. (2017a)

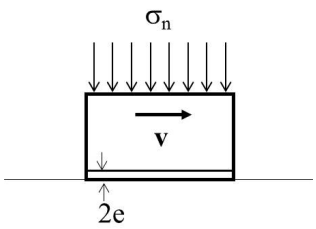

Figure 4.4: Loaded block sliding at constant velocity. Pinyol et al. (2017a)

The effect of the shear band thickness can be derived for the case of a simple block sliding on a horizontal surface at an imposed constant velocity (v) (Fig. 4.4). With the aim of getting an analytical solution, heat and pore water pressure dissipation will be neglected. Under these assumptions, the system of equations given in Section 4.2 reduces to the following differential equation:

$$\frac{\mathrm{d}p_L}{\mathrm{d}t} = \frac{\beta \tan\phi' v}{\left(m_v + n\alpha_L\right)\left(\rho c\right)_m 2e}\left[\sigma_n - p_L\right] \tag{4.23}$$

where the unknown variable is the excess pore water pressure (p_L) in time, $2e$ is the thickness of the shear band and m_v is the oedometric compressibility coefficient. Equation (4.23) has the following analytical solution:

$$p_L = \sigma_n \left(1 - \exp^{-\frac{\beta \tan\varphi' v}{\left(m_v + n\alpha_L\right)\left(\rho c\right)_m 2e} t}\right) \tag{4.24}$$

which is represented in Figure 4.5 for the case of an imposed velocity of 0.1 m/s, a normal stress $\sigma_n = 1\ MPa$, an oedometric compressibility coefficient equal to $m_v = 1.5 \cdot 10^{-3} MPa^{-1}$ and different values of shear band thickness. The rest of parameters are selected according to Table 4.1. The results show a large effect of the shear band thickness: the larger the shear band thickness the lower the excess pore water pressures generated.

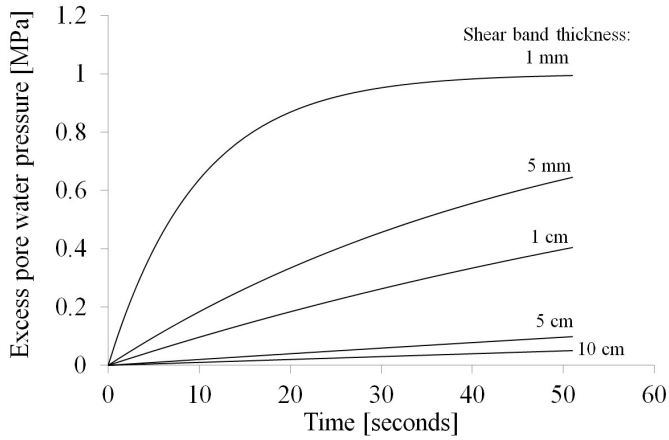

Figure 4.5: Analytical results for the excess pore water pressure for different values of shear band thickness in the case of a planar motion on a horizontal surface at constant imposed velocity. Pinyol et al. (2017a)

On the other hand, the thickness of the shear band has an influence on the liquid pressure and temperature dissipation, which has been neglected in the previous analytical solution. Following the simple example illustrated in Figure 4.3, the heat-induced increments of temperature and liquid pressure will be distributed homogeneously inside the shear band. For a given soil permeability, the dissipation will be faster in the case of the thinner shear band because of the higher water pressure gradients.

The thickness of shear band depends on the grain size distribution of soils (Alshibli and Hasan (2008); Mühlhaus and Vardoulakis (1987); Scarpelli and Wood (1982); Vardoulakis (1980)). A sensitivity analysis of the effect of the shear band thickness on landslide behaviour including thermal effects was given by Pinyol and Alonso (2010a,b) and Alonso et al. (2016). They solved the THM coupled phenomena at the scale of the shear band as a one-dimensional problem and solved it by finite differences. The geometry of the slide and the position of the sliding surface was predefined in theses contributions and they do not depend on the numerical discretization. The thickness of the shear band was also defined as an input data and it does not depend on the element size of the FD discretization.

Alonso et al. (2016) also solved the case of a zero-thickness shear band. In this case, the shear band is assumed to be a contact plane and the heat generated was included as a boundary condition. A heat flow per unit of surface of the sliding plane, calculated as the product of the shear strength and the landslide velocity, was imposed. Heat inflow induces the increments of temperature that leads to increments in pore water pressure. Based on the analyses performed, they concluded that for realistic shear bands thicknesses (in the range of few millimiters including also the zero-thickness case) the results in terms of pore liquid pressure, temperature and landslide velocity are not significantly different among them. This is an interesting conclusion which suggests that it is not necessary to specify the shear band thickness, always difficult to quantify.

However, when the shear band thickness increases the results are significantly affected. The case is analyzed here following the 1D finite difference analysis presented in Alonso et al. (2016) for a planar landslide described in Figure 4.6a, which corresponds to a situation of strict equilibrium. Consider a case of a low value of permeability ($K = 10^{-11}\ m/s$). The rest of parameters are indicated in Table 4.1. The landslide is triggered by increasing the water level by 10 cm. The results in terms of landslide velocity during the first 50 m of travelling are plotted in Figure 4.6b for different values of shear band thickness ranging from $1mm$ to $1m$. The pore water pressure dissipation during the motion is negligible in all cases. The isothermal case is also included in the plot. The results show that the

effect of the shear band thickness becomes relevant for values higher than 1 cm.

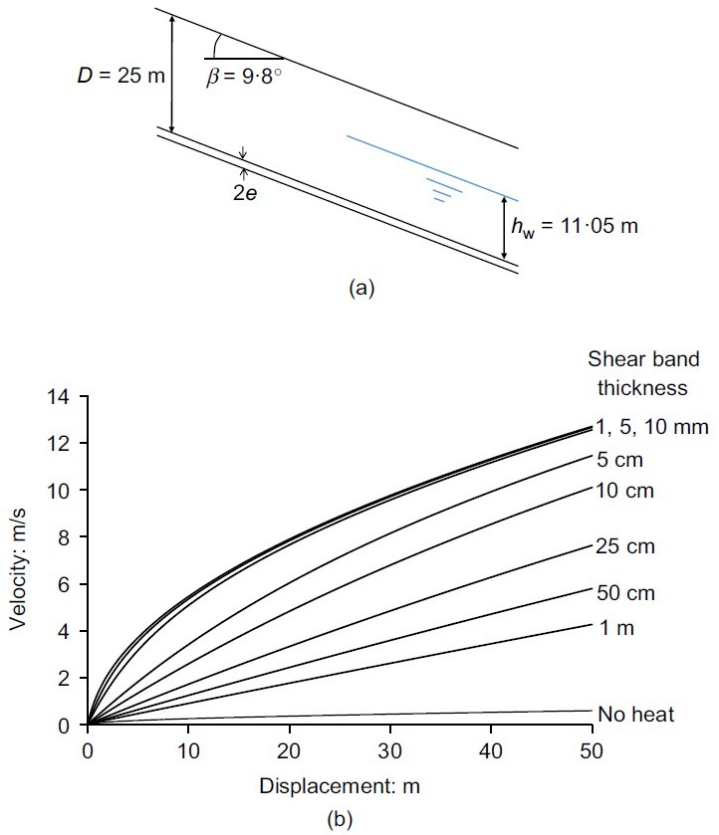

Figure 4.6: (a) Scheme of a planar slide. (b) Effect of the shear band thickness on the velocity for $K = 10^{-11}\ m/s$. $1D$ finite-difference analysis. Pinyol et al. (2017a)

In numerical approaches such as FEM, FDM and MPM, the size of the shear band developed when shear strains localize depends on the element size and on the inclination of the band with respect to the mesh lines. In practice, strains tend to localize into a single or a few elements. Therefore, in view of the previous results (Fig. 4.6b), the size of the elements of the computational mesh in a MPM numerical model should be similar to the thickness of the actual shear band (i.e. few millimiters or perhaps centimetres) in order to obtain realistic results. Otherwise, the computed heat generated in the slip zone per unit of volume will be lower than the heat actually generated. However, in real landslide modelling, the size of landslides requires element sizes in the order of decimeters or meters if the computational cost is to be kept within limited and tractable limits, especially in cases of coupled THM analysis.

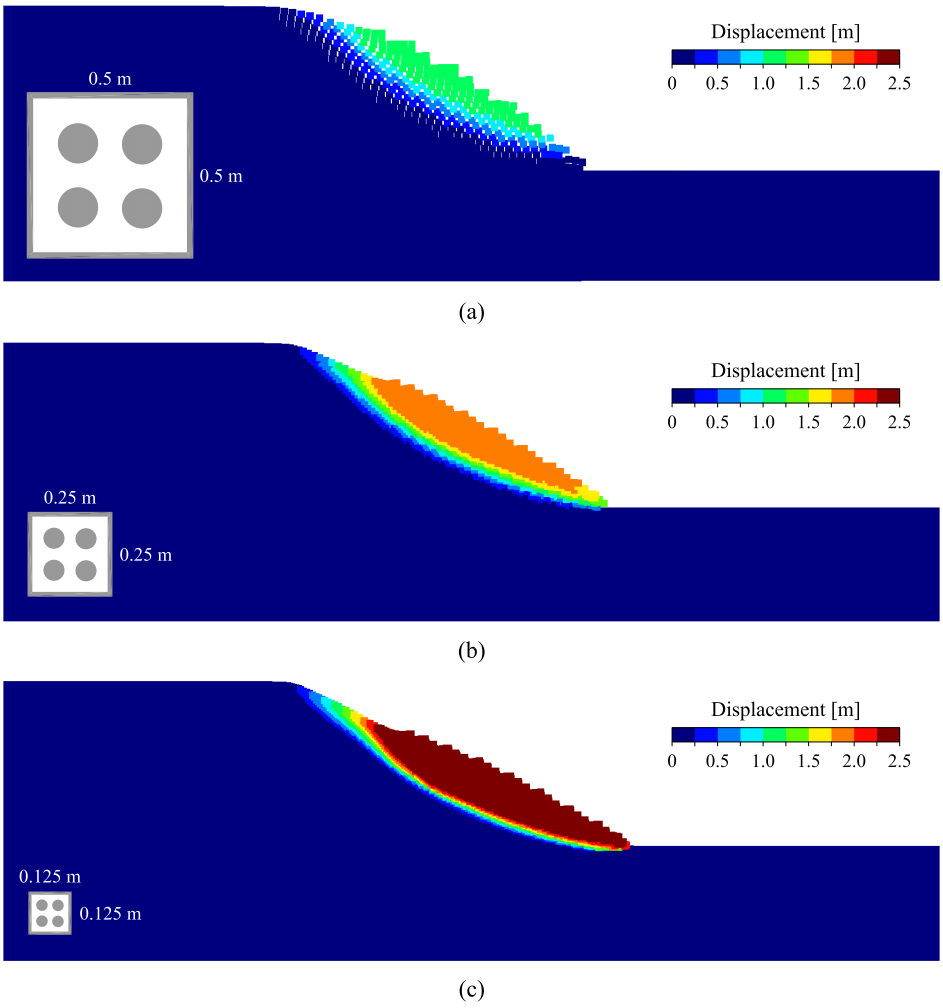

Figure 4.7: Maximum displacement calculated for the reference case for a permeability value of $K = 10^{-11}\ m/s$ and for different sizes of mesh elements (indicated in the figure).

It follows that a direct application of Equation (4.10) to calculate the energy dissipated in a shear band will results in work rates per unit volume significantly smaller that the rates dissipated in real sliding surfaces. The consequence is an underestimation of excess pore pressures generated in shear bands. This effect can be readily observed in a mesh size sensitivity analysis of the reference case discussed in the previous section for a low value of permeability ($K = 10^{-11}\ m/s$). The case has been run again using two additional coarser discretizations described by square meshes of $0.5 \times 0.5\ m$ and $0.25 \times 0.25\ m$. The calculated displacement

and excess pore water pressure at the end of the motion are plotted in Figure 4.7 and 4.8, respectively. Both depend markedly on the mesh size. A numerical alternative to overcome such dependency is described in the next section.

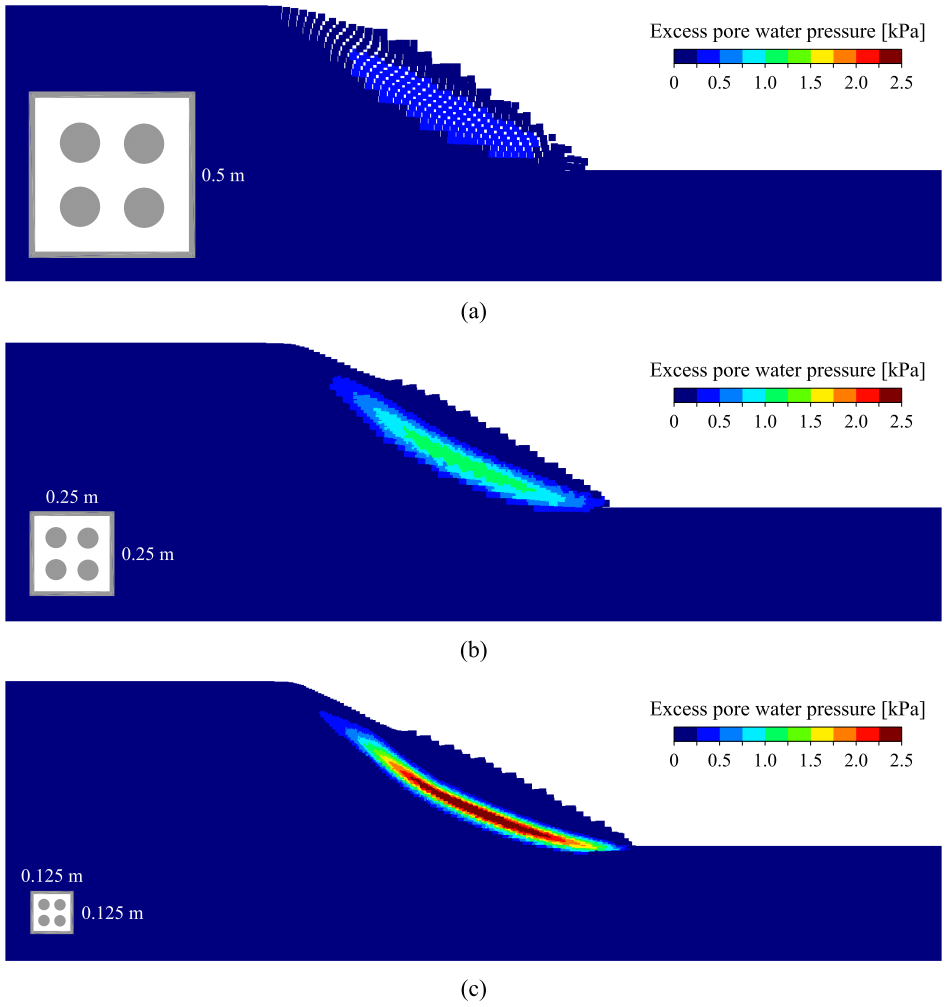

Figure 4.8: Excess pore water pressure at the end of the motion calculated for the reference case for a permeability value of $K = 10^{-11}\ m/s$ and for different sizes of mesh elements (indicated in the figure).

4.5 Embedded shear bands

A numerical procedure has been developed in order to consider the real shear band thickness when performing numerical modelling of THM phenomena in landslides. It should be noted that the proposed procedure does not provide a methodology to solve the mesh dependence effect in strain localization problems simulated by continuous numerical models such as FEM and MPM (caused or not by strength softening). The proposed procedure provides a solution to account properly for the magnitude of the heat and excess pore water pressure generated because of the generated frictional work and their dissipation, which depends on the shear band thickness.

The idea was to include a set of embedded shear bands into the material domain whenever the plastic deviatoric strain exceeds a reference value. Figure 4.9 illustrates the explanation. A reference volume corresponding to the initially assigned to each material point is characterized by a reference length, L_{ref}. The strain computed at each material point will be assumed to be localized in an embedded shear band whose thickness will be given as an input parameter, L_B, which will depend on the soil type. Heat due to friction work dissipation and the induced liquid pressure will be assumed to be generated into the embedded elements. Different variables for temperature and liquid pressure in the embedded shear bands and the rest of the soil are defined: θ^B, θ^M, p_L^B, p_L^M, respectively.

Dissipation processes of heat and liquid flow between the embedded shear bands and the rest of the material domain, called matrix, will be formulated at local level. Energy and mass balance equations are now formulated at matrix and embedded shear band level as follows:

$$\frac{D}{Dt}\left[(\rho c)_m \theta^M\right] + \nabla \cdot \left[-\Gamma \nabla \theta^M\right] + \nabla \cdot \left[\rho_L c_L \mathbf{q} \theta^M + (\rho c)_m \mathbf{v}_S \theta^M\right] = f_\theta^{B-M} \quad (4.25)$$

$$\frac{D}{Dt}\left[(\rho c)_m \theta^B\right] = -f_\theta^{B-M} + \dot{H}^B \quad (4.26)$$

$$\frac{D}{Dt}\left[\beta \theta^M\right] + n\alpha_L \frac{Dp_L^M}{Dt} + \nabla \cdot \mathbf{v}_S + \nabla \cdot \mathbf{q}_L = \frac{1}{\rho_L} f_L^{B-M} \quad (4.27)$$

$$\frac{D}{Dt}\left[\beta \theta^B\right] + n\alpha_L \frac{Dp_L^B}{Dt} = -\frac{1}{\rho_L} f_L^{B-M} \quad (4.28)$$

Local source terms of heat and liquid flow rate per unit of volume and time are included in the balance equations to take into account the dissipation of heat and

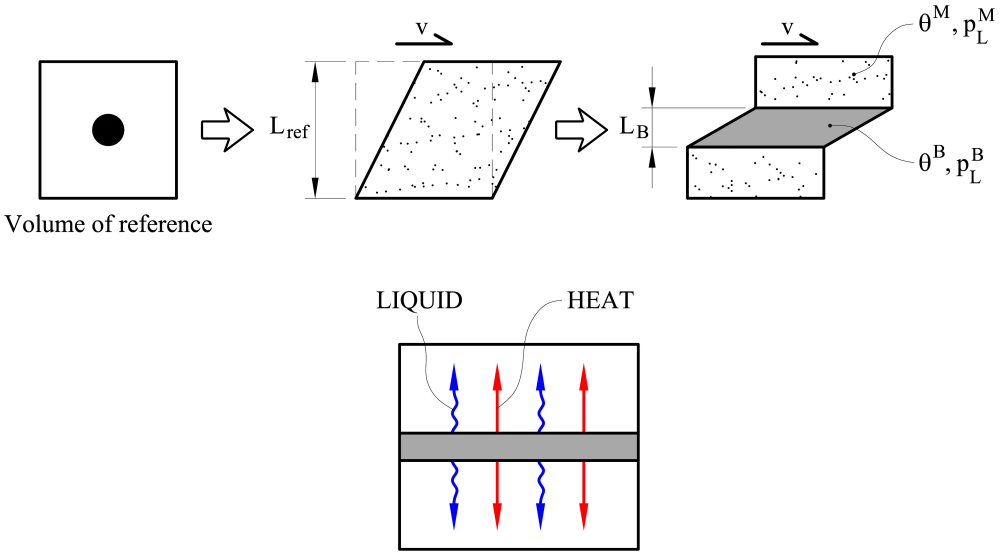

Figure 4.9: Schematic representation of embedded shear bands generated. Pinyol et al. (2017a)

liquid pressure between matrix and embedded elements. Flow rates are defined proportional to the difference between band and matrix temperature and liquid pressure:

$$f_L^{B-M} = \psi_L \left(p_L^B - p_L^M \right) \tag{4.29}$$

$$f_\theta^{B-M} = \psi_\theta \left(\theta^B - \theta^M \right) \tag{4.30}$$

ψ_L and ψ_θ are defined as liquid and energy transfer coefficients, respectively.

Equation (4.29) for the local liquid source term, f_L^{B-M} (mass per unit volume per unit time) is approximated in terms of a difference in pressures to facilitate the calculation at the local level. From a physical perspective it should be related to the gradient of pressures through some permeability coefficient. This consideration suggests that the transfer coefficient, ψ_L, has the following structure:

$$\psi_L = \frac{\rho_L k}{\mu_L \mathrm{A}_{ref}} \tag{4.31}$$

expressed in terms of liquid density, ρ_L, liquid viscosity, μ_L, intrinsic permeability, k, Fourier's coefficient, Γ, and a reference area, A_{ref}.This area is directly related to the expected distance of fluid transfer from the shear band, included in a material point, and the surrounding clay matrix associated with the material point under consideration. Therefore, A_{ref} was made equal to the element area contributing to the MP (one fourth of the element area if four material points per element are adopted). A similar argument, in the case of local heat interchanged leads to

$$\psi_\theta = \frac{\Gamma}{\mathrm{A}_{ref}} \tag{4.32}$$

Computations run for the reference case described below to show the effect of varying A_{ref} from $\mathrm{A}_{ref}/4$ to $4\mathrm{A}_{ref}$ resulted in minimum changes in results.

In Equations (4.25 to 4.28), convective and advective terms are defined exclusively at the matrix scale to impose that the interaction between embedded elements and matrix are defined locally at the scale of the reference volume.

The heat source term, $\dot{H}^B$, included into the heat mass balance equation of the band is supplied by energy generated into the embedded shear band. It is made equal to the frictional work rate dissipated assuming that the plastic strains localize in the shear band:

$$\dot{H}^B = \sigma' : \dot{\varepsilon}^p \frac{L_{ref}}{L_B} \tag{4.33}$$

The effective stress controlling the constitutive behaviour will be governed by the maximum value of liquid pressure prevailing in the embedded elements or in the matrix because they occupy the same position of the material point under consideration:

$$\sigma' = \sigma - \max\left(p_L^B, p_L^M\right)\mathbf{m} \tag{4.34}$$

4.6 Sensitivity analysis. Effect of the mesh size, shear band thickness and permeability

The reference case evaluated previously using different element sizes is analysed again including the embedded shear band with the aim of evaluating the capabilities of the methodology. In all the cases analysed, embedded shear bands are generated at those elements in which the computed plastic deviatoric strain is different from zero. The distribution of excess pore water pressure and maximum displacement is plotted in Figures 4.10 and 4.11. The effect of the mesh size is observed in minor details of the plots. However, the pathological dependence on the shear band thickness has been removed. In fact, the calculated maximum pore pressure in the shearing band (Fig. 4.10) and the displacement (Fig. 4.11) are the same. In the three cases analysed, an embedded shear band thickness L_B of 1 cm was introduced as an input parameter.

The effect of the shear band thickness is shown in Figure 4.12 in terms of maximum displacement. Band thickness varying between 10 cm and 0.5 cm are evaluated. Thinner shear bands lead to higher values of thermal induced pore water pressure and the associated reduction of the shear strength results in higher values of maximum velocity and displacement.

The effect of the permeability is now evaluated. In all the cases evaluated, L_B = 1 cm. Figure 4.13b shows the evolution of displacements of a point located initially at the surface in the middle of the slope (Fig. 4.13a) for different values of permeability ranging from 10^{-3} m/s to 10^{-11} m/s. Figure 4.13c shows the calculated pore pressure records on a central point of the sliding surface. Zero values of pore water pressure are calculated in the most pervious case ($K = 10^{-3}$ m/s). When permeability decreases to $K = 10^{-5}$ m/s, low values of excess pore pressure are accumulated. For $K = 10^{-7}$ m/s pore pressure initially increases, to reduce during the motion. As the values of permeability decrease further, the maximum velocity and the displacements increase due to additional excess pore water pressure accumulating in the shear band (Fig. 4.13b).

The distributions of plastic strains, excess pore water pressures and temperature for the case of $K = 10^{-11}$ m/s are plotted in Figure 4.14. The shear strain increments localize in a band affecting one or two elements of the computational mesh. The generation of the excess pore water pressure concentrates at those elements and, due to their low permeability and the short time of the motion, pore pressure does not dissipate.

Temperature increments are generated in all cases as a consequence of the frictional work dissipated during the motion (Fig. 4.14c). Calculated temperature increments are small but their effect is significant because of the induced changes in thermal dilation coefficient of water and solids.

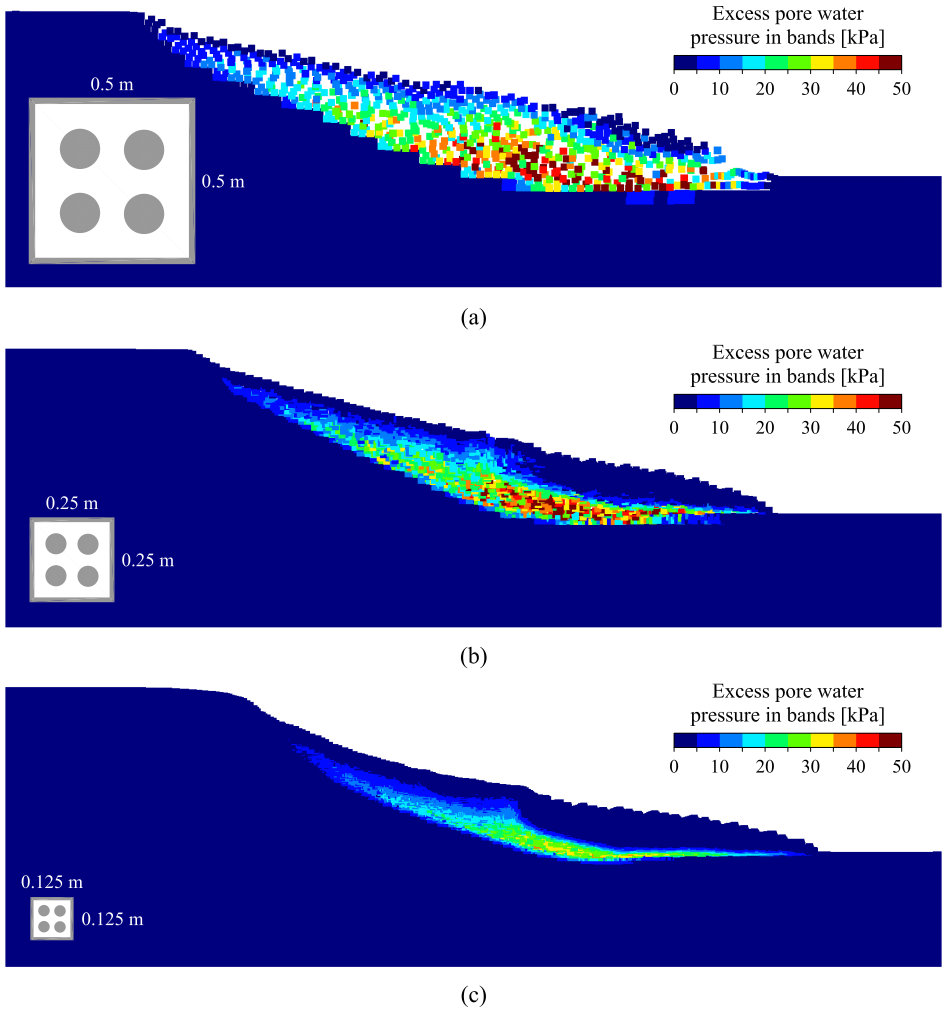

Figure 4.10: Excess pore water pressure at the end of the motion calculated for the reference case, including embedded shear bands, for a permeability value of $K = 10^{-11}$ m/s and for different sizes of mesh elements: (a) 0.5×0.5 m; (b) 0.25×0.25 m; (c) 0.125×0.125 m.

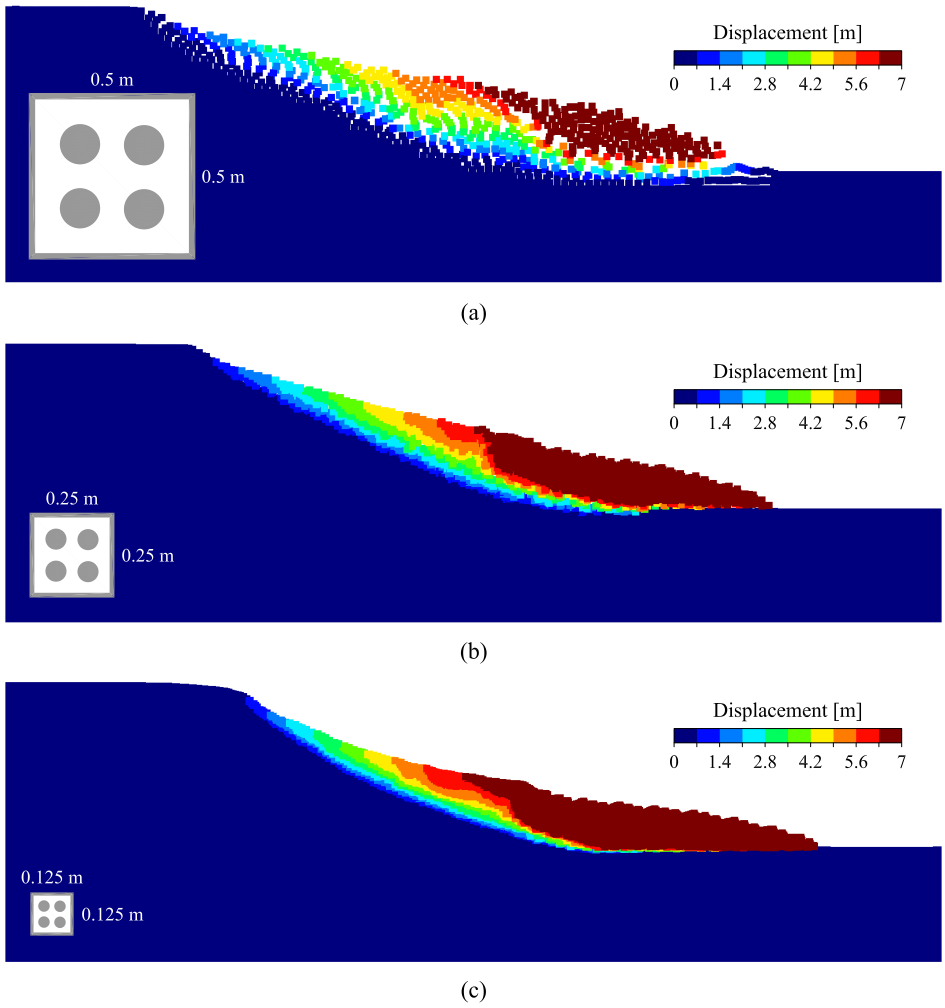

Figure 4.11: Maximum displacement calculated for the reference case, including embedded shear bands, for a permeability value of $K = 10^{-11}\ m/s$ and for different sizes of mesh elements: (a) $0.5 \times 0.5\ m$; (b) $0.25 \times 0.25\ m$; (c) $0.125 \times 0.125\ m$.

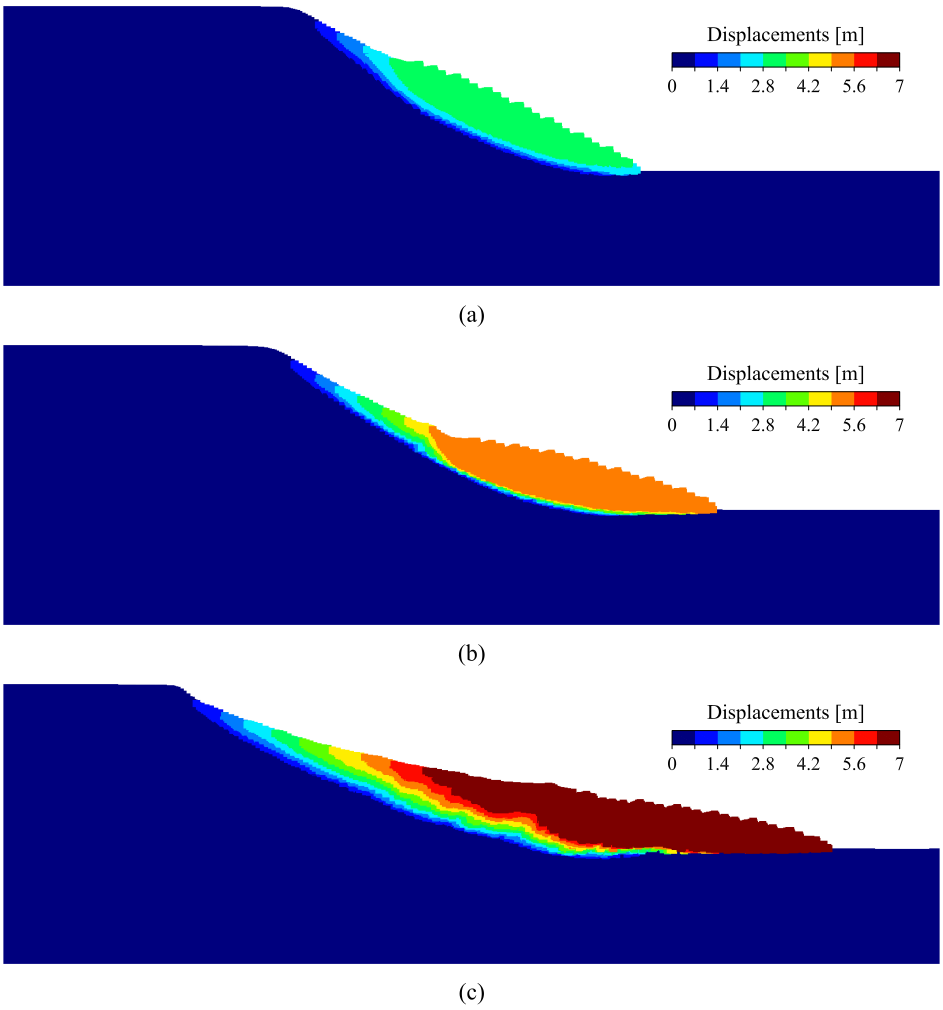

Figure 4.12: Maximum displacement calculated for the reference case with mesh size 0.125 × 0.125 m for a permeability value of $K = 10^{-11}$ m/s and for different values of shear band thickness: (a) 10 cm; (b) 5 cm; (c) 0.5 cm.

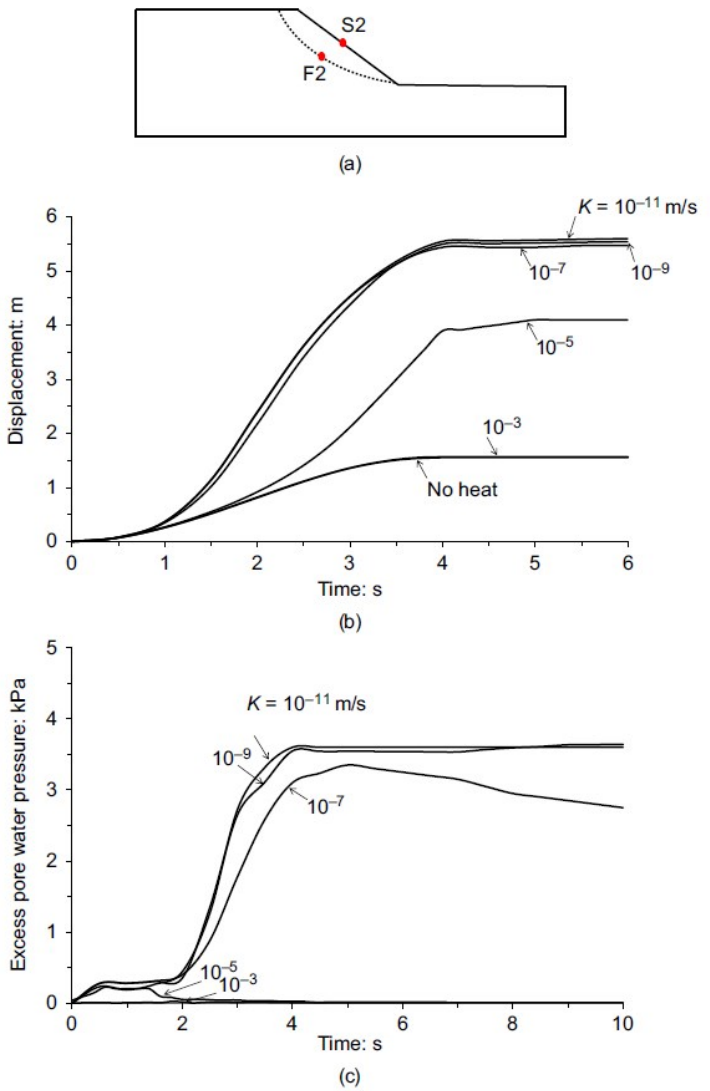

Figure 4.13: (a) Position of points analysed. (b) Displacement of point $S2$ and (c) excess pore water pressure evolution of point $F2$ for the reference case and different values of saturated permeability, K.

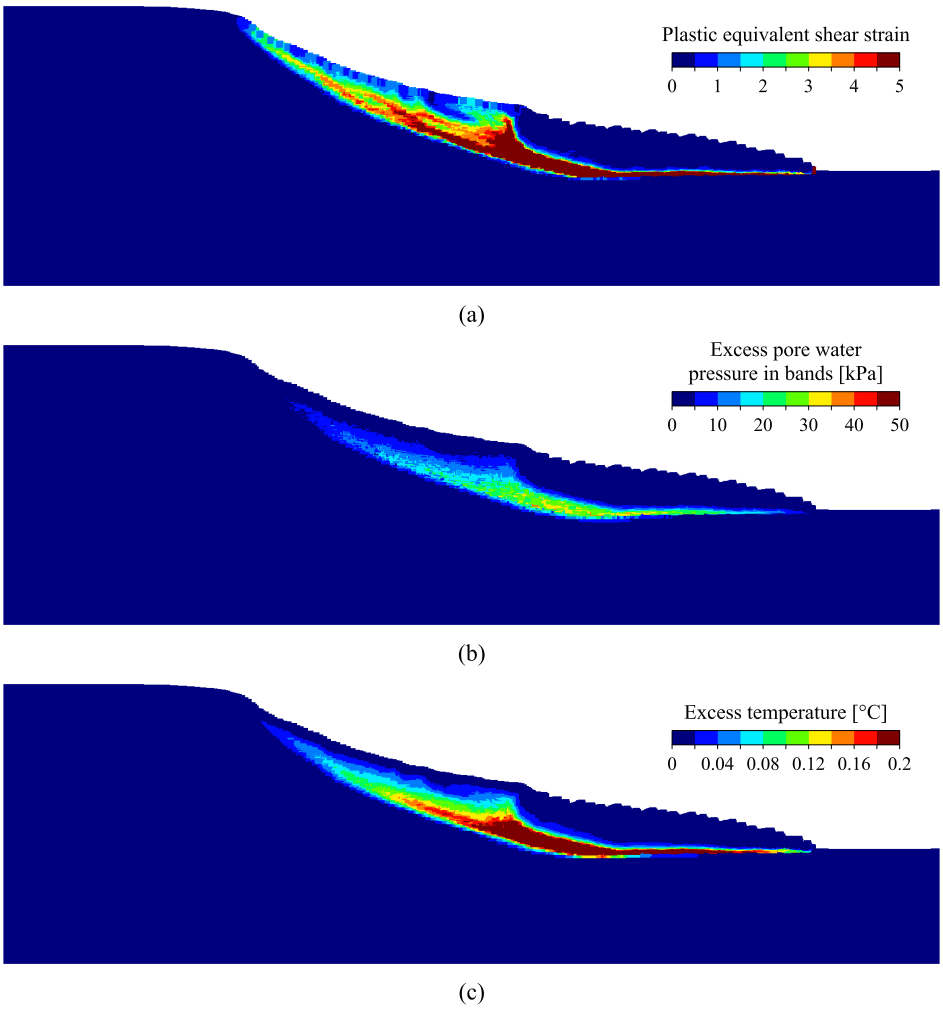

Figure 4.14: Distribution of (a) accumulated deviatoric plastic strains, (b) excess pore water pressures and (c) temperature for the reference case at the end of the motion. Saturated permeability $K = 10^{-11}$ m/s and shear band thickness of 1 cm.

4.7 Concluding remarks

This chapter describes a general formulation to include the heat dissipated in irreversible shear deformations into a coupled hydro-mechanical framework. The problem is inspired by observations and past contributions in the field of landslides. The formulation is general and based on physical principles and therefore it has applicability to sliding deformation mechanisms. The formulation of the basic theory and the subsequent elaboration is a generalization of previous contributions in the domain of fast landslides which describe the slide motion by means of a predetermined simple geometry characterized by blocks of bodies interacting at the boundaries through shearing surfaces. Furthermore, previous contributions formulate the necessary balance equations in a one-dimensional space, perpendicular to the shearing surface. This limitation is also removed in the present analysis.

One difficulty of the model developed, which was numerically solved by means of a Material Point Method approach, is the dependence of the results on the thickness of the shear bands developing in a failure scenario. In fact, the method predicts the generation of heat induced excess pore water pressures in shear bands, which controls the available drained shear strength. Excess pore pressures dissipate in a consolidation-like processes controlled by permeability, soils stiffness and shear band thickness. Permeability is the main controlling factor for pore water pressure and heat development as well as for the resulting slide kinematics once failure is triggered. However, shear band thickness is also a critical parameter which depends on the size of elements and geometry of the computational mesh. Given the small thickness expected in shear bands in clayey soils, the appropriate computational mesh would become unrealistically dense. The effect of shear band thickness is first discussed with the help of a simple sliding model which was solved analytically.

A two-dimensional plane strain MPM analysis of the failure of a reference simple slope illustrates the significant effect of mesh size in results. The procedure described in the chapter to solve the shear band thickness issue is to embed a ubiquitous set of shear bands into the material domain whenever plastic strains develop. These strains are assumed to be localized in a shear band whose thickness is selected in view of the material properties or other observations. A set of balance equations for the local transfer of liquid and heat is formulated to reproduce the expected physical phenomena in the vicinity of the shear bands. The procedure was successfully tested in a reference slope analysis. Excess pore pressures and slope deformation were found to be independent of mesh size.

5

Chapter 5

Vajont Landslide in THM-MPM

In the previous chapter, the thermo-hydro-mechanical formulation in MPM was presented. In this chapter the MPM code developed is applied to model the instability and subsequent rapid motion of Vajont landslide (Italy, 1963). Calculated run-out and sliding velocity reproduce, in a satisfactory manner, field observations.

5.1 Vajont landslide

An ancient slide in the left bank of the Vajont river (Italy), under creeping motion, presented a rapid failure in October 1963, when the reservoir provided by the built dam, reached the maximum level. The mobilized mass developed great speed, provoking a gigantic water wave over 220 m high that flew over the dam.

According to observations of geological study, since the construction and partially impounded of the reservoir in 1960, a long, peripheral crack developed, indicating creeping motion towards the reservoir (Hendron and Patton, 1985) (Fig. 5.1) that continued until the rapid failure in October 1963, exhibiting a wide range of

rate of movement over the years. Velocities of $20 - 30$ cm/day were registered near failure date, while estimations of the field reached velocity on $9th$ October 1963 was of 30 m/s. The accumulated displacements of surface markers showed correlation with reservoir elevation (Nonveiller, 1987).

Semenza (2001) included a tentative reconstruction of the past history of the slide in a series of cross sections. Two representative cross-sections of the slide, located upstream of the dam's position at distances of 400 and 600 m (5.2), respectively, are reproduced in Figure 5.2 (Sections 2 and 5. (Hendron and Patton, 1985)).

Regarding the sliding surface of the landslide, Hendron and Patton (1985) indicates that it was located in a thin continuous layer of high plasticity clay. Other authors suggest the existence of a more complex geometry defining not a unique sliding surface but by several sliding layers or even a thick sliding area. This topic is discussed in the next section.

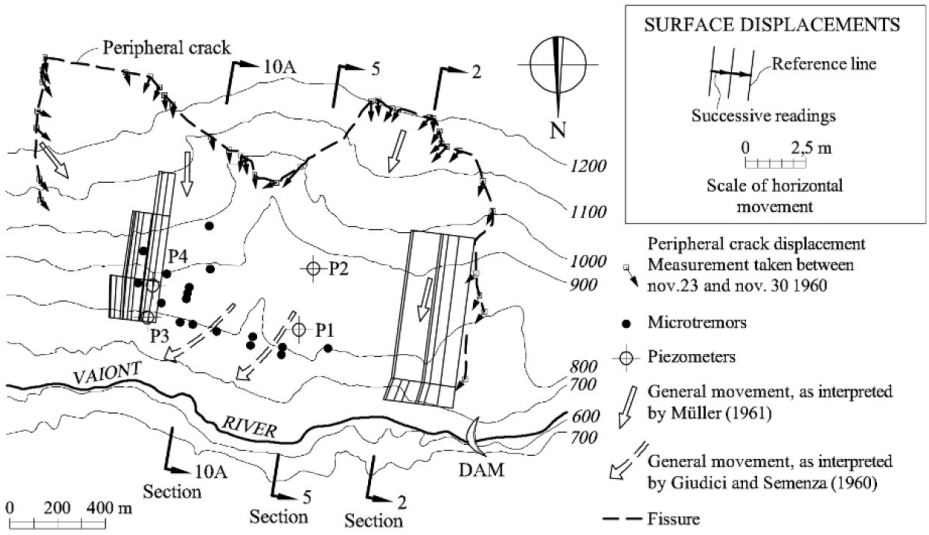

Figure 5.1: Map of the Vajont sliding area. Alonso et al. (2010)

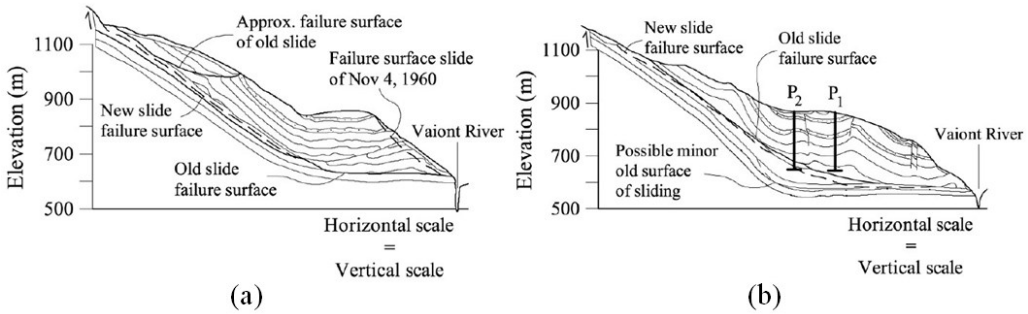

Figure 5.2: Two representative cross-sections of the landslide: (a) Section 2; (b) Section 5 (see the location in Fig. 5.1). After Hendron and Patton (1985). The position and length of piezometers P1 and P2 are shown on Cross-section 5.

5.2 MPM model

The model developed in this thesis departs significantly from the analysis described in previous publications on modelling Vajont landslide. Alonso et al. (2016) compares the modelling approaches of previous contributions taking into account a few topics: problem formulation, sliding geometry and constitutive modelling. The analysis described here is no longer based on the 1D approximation for THM processes in the vicinity of the shear band, the geometry respects the geological conditions of the case and the failure mechanism and landslide geometry are not imposed "a priori". There was an interest in checking if this generalization could reproduce the Vajont accelerated motion.

Initially the gravity acceleration is applied with the reservoir level at the very bottom, then the landslide trigger was the elevation of the water level in the reservoir. The impoundment of the reservoir is modelled as a continuous increase in water level, imposing the groundwater level at material points. Modelling the creeping stage previous to the failure would involve the consideration of additional features. In particular, Veveakis et al. (2007), Alonso et al. (2016) and Alonso and Pinyol (2012) invoked rate effects on the strengthening of the behaviour of the material located in the basal surface to explain the slow motion observed in Vajont slope. In addition, the internal shearing of the mobilized mass during the motion, discussed in Alonso and Pinyol (2010) and Yerro et al. (2016a), probably had also an important role which contributed to maintain the slope at a slow motion. These aspects are out of the scope in this chapter, which focuses on the thermal pressurization phenomena and its consequences on the Vajont landslide run-out.

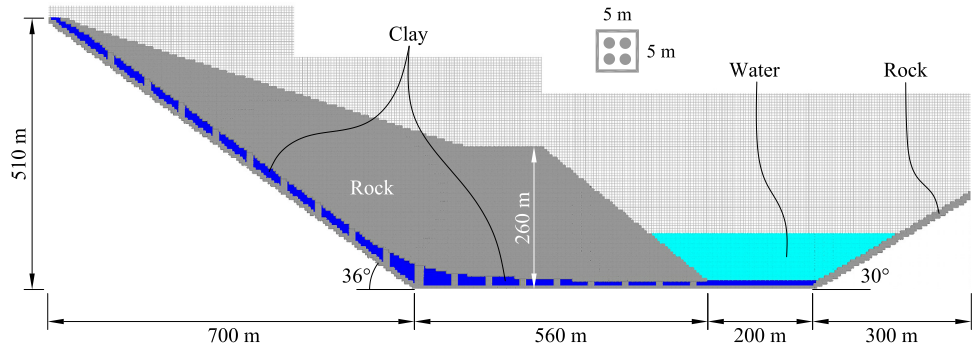

Figure 5.3: Computational model, mesh and initial distribution of material points.

The two-dimensional section selected for the analysis follows Section 2 (Fig. 5.2a) proposed by Hendron and Patton (1985). Figure 5.3 shows the cross section modelled. The mobilized mass is characterized by a unique homogeneous rock whose behaviour is defined by the strain-softening Mohr-Coulomb model. In the MPM model, the rock was defined by a $c'_{peak} = 2800kPa$ and $\phi'_{peak} = 43°$ and $c'_{res} = 200kPa$ and $\phi'_{peak} = 34°$. The softening shape factor selected ($\eta = 100$) leads to a drop of strength from peak to residual value in 30 mm of relative displacement for this mesh size. The selected values are accepted as a rough average approximation of the complex stratification of limestone and marl layers Semenza (2001) with different degrees of fracturing. They are also consistent with the range of average strength parameters suggested by Alonso and Pinyol (2010) for the Vajont rock above the sliding surface. A porosity equal to $n = 0.2$, a Young modulus $E = 5000\ MPa$ and a Poisson′s coefficient $v = 0.33$ were estimated for the rock mass. Parameters for the model are the same used in previous chapter for the reference case (Table 4.1).

The model is able to simulate the progressive failure along shearing planes of the rock. This is expected because the kinematics of the motion force internal shearing of the rock in direction crossing the sedimentary surfaces at high angles. This is shown in the plots of shearing bands given below. This internal shearing was also discussed in Alonso and Pinyol (2010) and Yerro et al. (2016a), Yerro et al. (2016b). Yerro et al. (2016b) found that a unique sub-vertical shear band develops from the sharp kink defined by the two planar basal sliding surfaces. This band acts as a rock degradation mechanism as the slide moves forward. A progressive failure develops along the shear band during all stages of motion. It was also shown that the internal development of shearing bands in the rock mass is controlled by the geometry of the basal sliding surface. Progressive failure of the

brittle rock mass alone was not capable of explaining the high sliding velocities of the slide. An apparent basal friction angle of 0° was required to match the high velocities of the slide.

A significant aspect of the analysis is the nature of the basal sliding surface. In their comprehensive report, Hendron and Patton (1985), even if they accept the dominant role of the residual clay strength, they recognize the existence of areas in which shearing was across bedding planes, the presence of sections not having clay, of areas where the clay was squeezed into rock voids and of brecciated rock fragments within the clay beds. Paronuzzi and Bolla (2015) characterized the basal "detachment" surface by a stepped pattern involving a variety of materials: limestone and marly limestone strata, clay interbeds, clay lenses and angular gravels. Wolter et al. (2014) describe in detail the basal surface by means of terrestrial photogrammetry. The exposed surface is characterized by a complex geometry of undulations and ridges which probably entered into rock-to-rock contact during sliding. They introduce four roughness classes to describe the sliding surface. They conclude that in some areas the asperities would imply the shearing of rock mass or a dilatant behaviour. Figure 5.4 shows the aspect of the basal surface in the spring of 2007, immediately above the displaced rock mass. Some of the mentioned features could be observed in the photographs. The set of observation summarized above indicate that the basal sliding motion was far from being a smooth planar uniform shearing across a layer of clay. Rock shearing and rock-to-rock friction was present during the landslide.

The available information is not enough to adopt a precise model of the basal surface and it was decided to represent it by a number of brittle rock bridges separated by a clay areas (Fig. 5.3). The rock bridges were characterized by the rock properties adopted for the sliding rock mass. Residual strength of the high plasticity clay of the basal surface measured in shearing tests (Ferri et al., 2011, 2010; Hendron and Patton, 1985; Tika and Hutchinson, 1999) suggest a value of 11° for the residual friction angle. A low permeability ($K = 10^{-11}\ m/s$) was adopted for the clay in view of its high plasticity.

The underlying stable bedrock below the clayey layer was given the same properties to the overlying rock. This material is also present in the opposite valley slope. The river canyon on the bottom of the valley was not represented. The calculations indicated that the failure surfaces did not affect the lower boundary rock because of the significantly lower strength of the clayey layer with respect to the rest of the rock. Therefore, the thickness of the material below the clayey layer is small in order to reduce the dimension of the model and the computational cost.

Figure 5.4: Exposed basal surface of Vajont landslide in 2007. Photographs taken in the lower part of the exposed sliding surface. (Pinyol et al., 2017a)

The model includes also the reservoir water as an elastic material characterized by its real volumetric compressibility coefficient and imposing a shearing modulus close to zero. This procedure allows to apply the weight of the water and the corresponding water pressure on the slope surface at the initial time and also during the motion. The dynamic water forces induced during the motion are also included automatically in the calculation. This is a better option than imposing the effect of the reservoir water as a supporting force because these conditions should be applied on the slope surface, which is not fixed, and the position of the nodes or material points defining the slope surface are unknown "a priori".

Figure 5.3 also shows the computational mesh used, which defines the entire domain of the problem. Four materials points are initially distributed within the elements representing the materials. They are located at the corresponding integration points of a four-point Gaussian quadrature. The rectangular elements are $5 \times 5\ m$. This size is limited by the computational cost of the calculation. Using such element size, it is not possible to define accurately the sedimentary layers of Vajont slope. The lower heterogeneous clayey layer was defined by four elements across its thickness. The purpose of this discretization was to avoid that inner elements of the clay band shared nodes with the hard rock material.

According to the discussion presented in Chapter 4, the mechanical work dissipated in heat was scaled, within the embedded localization bands, by assuming a reference clay band thickness of 3 cm. No excess pore pressures were allowed in the rock material because of its high permeability. The initial stress state is the

result of applying the gravity loading.

5.3 Numerical results

The application of weight before the rise of the reservoir level leads to the mobilization of the strength of the clay material as shown in Figure 5.5a where the equivalent plastic shear strains are plotted. The slope remains in static equilibrium thanks to the strength provided by the rock bridges and rock mass. The increase of the water reservoir level leads to the rise of pore water pressures on the sliding surface. The supporting action of the water is also accounted for. Failure initiates when the water level is 100 m above the toe. It corresponds to the elevation 700 m according to the cross-section 2 from Hendron and Patton (1985). At this time, equivalent plastic shear strains localize as shown in Figure 5.5b. Shear surfaces grow from the basal sliding surface at those points where the geometry of the sliding surface, conditioned by the geometry of the clay layer, exhibit a change in curvature. In fact, the infinite curvature radius of the planar sliding surfaces reduces to a radius of approximately 200 m in the curved zone around the kink created at the junction between the planar surfaces. The localized shear bands are curved and tend to join inside the rock mass. The associated strain softening result in a weak fracture surface which is visible in the plots of Figures 5.5 and 5.7.

The damage experienced by the rock mass at the end of the motion, once the landslide recovers a new static equilibrium, is shown in Figure 5.5c. Figure 5.5 shows the displacement and velocity records calculated as average of several materials points located in the five elements of the computational mesh forming the landslide toe. The maximum velocity reached by the landslide was reported by several authors. Müller (1964) mentions 25 m/s to 30 m/s. Ciabatta (1964) cited by Nonveiller (1987), performed a dynamic analysis to find 17 m/s. Nonveiller (1987) calculates a maximum velocity of 15 m/s. Voight and Faust (1982) in his pioneering contribution found a maximum velocity of 26 m/s (for a planar geometry). Hendron and Patton (1985) estimates values in the range $20m/s$ to 25 m/s. These are estimations based on a particular model for the dynamics of the motion and therefore they should be regarded as approximations to the actual field velocity. The maximum velocity calculated here (20 m/s) (Fig. 5.6) fits into the set of values mentioned. The calculated run-out (320 m) (Fig. 5.6) is close but somewhat smaller than other estimated values based on field observation (Hendron and Patton, 1985).

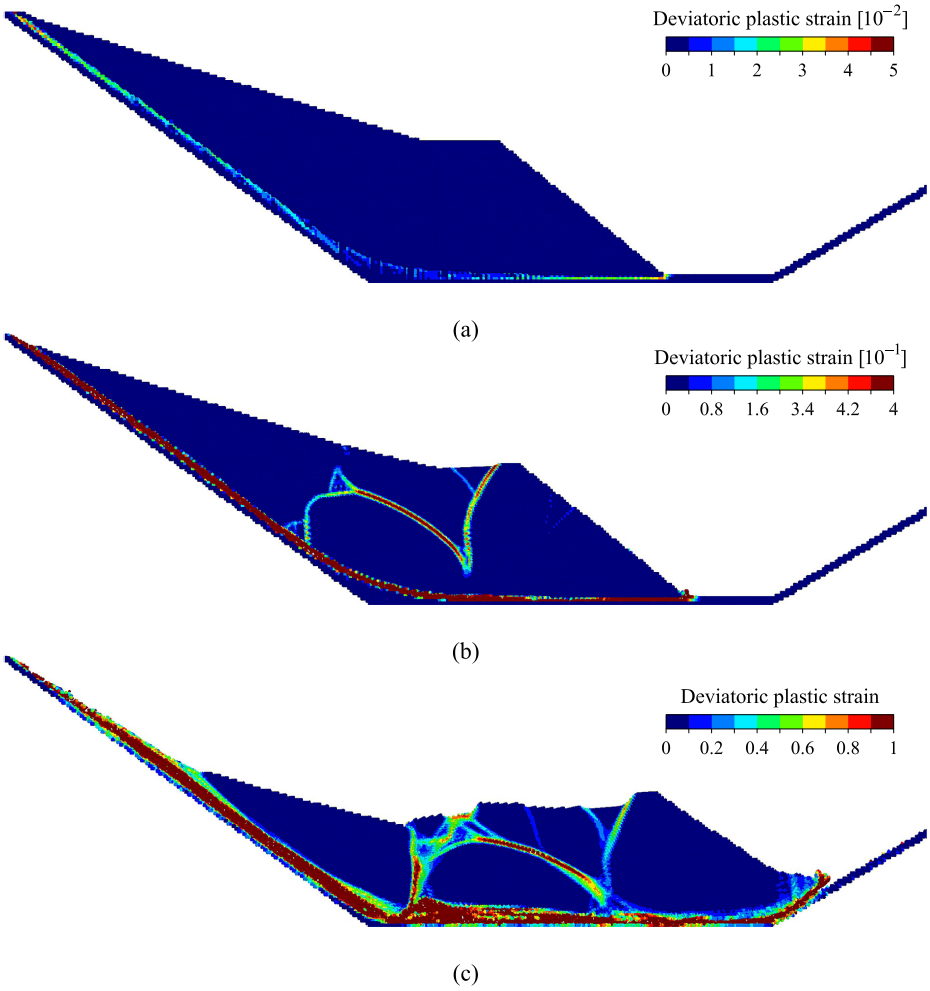

Figure 5.5: Equivalent plastic shear strain: (a) before reservoir impoundment upon application of gravity loading; (b) at the initiation of the motion when reservoir level is at 100 m; (c) at the end of the motion.

Temperature, heat-induced pore water pressure increment and displacement distributions are given in Figure 5.7. Increments of temperature around $50°C$ are computed in the basal shear band. Maximum temperature increments of around $40°C$ are computed inside the rock mass. Excess pore water pressures concentrate in the impervious clayey soil where the work has been scaled. Pore water pressure dissipates outside of the shear band affecting the rock overlying the clay layer. The presence of the previous rock bridges accelerates the pore water pressure dissipation. Figure 5.8 shows the calculated final positions of the landslide materials.

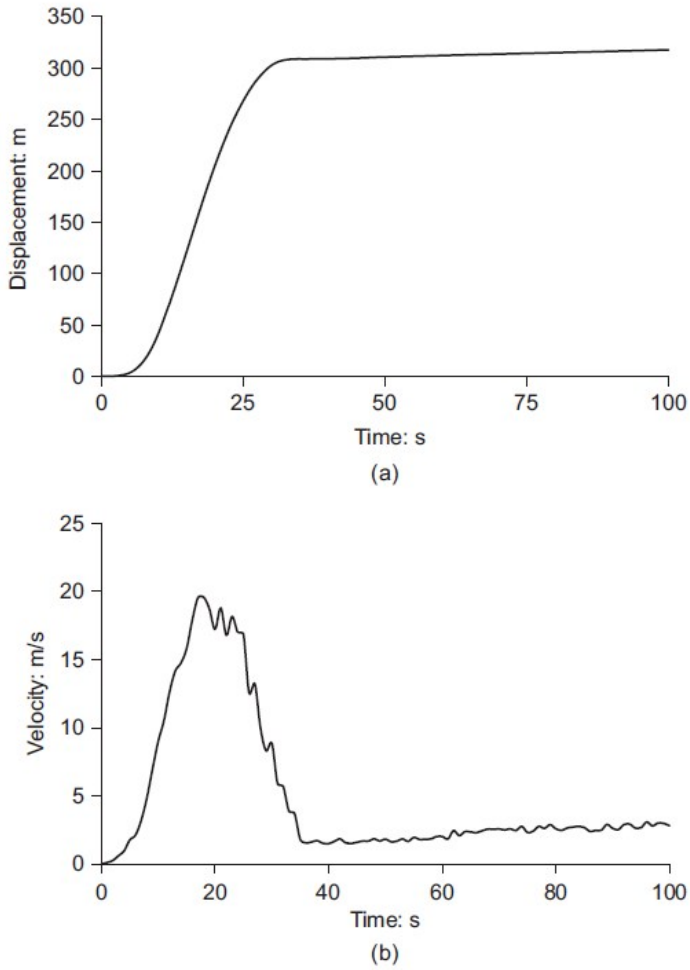

Figure 5.6: Calculated (a) displacement and (b) velocity of Vajont landslide.

What is actually plotted in the figure is the position of all material points. The basal clay layer has extended along most of the failure surface during the motion. In some places the clay has opened its way through the rock. Some field observations mentioned before support this result(Hendron and Patton, 1985; Paronuzzi and Bolla, 2015). Note also that a horizontal layer of clay was located beyond the toe of the slide to avoid a direct rock to rock contact during the motion. Part of this clay was dragged by the landslide and is visible in Figures 5.5c, 5.7 and 5.8.

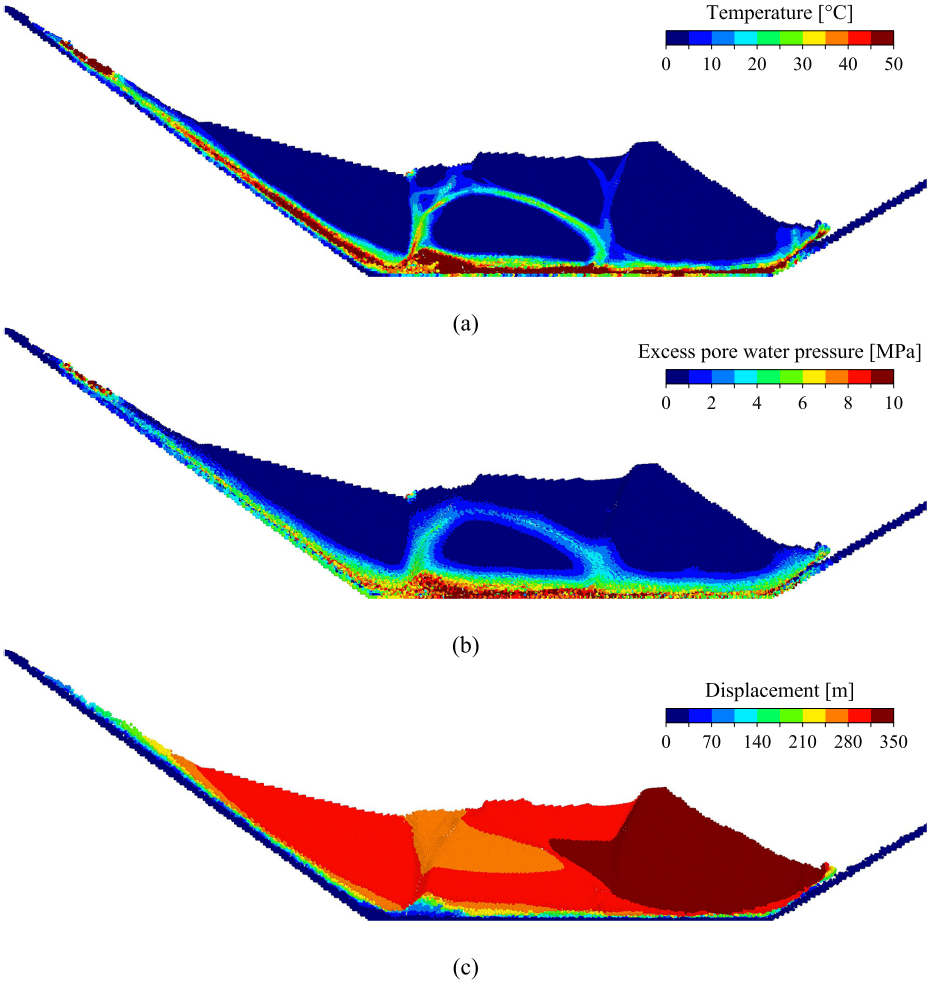

Figure 5.7: (a) Temperature; (b) excess pore water pressures and (c) displacements at the end of the motion.

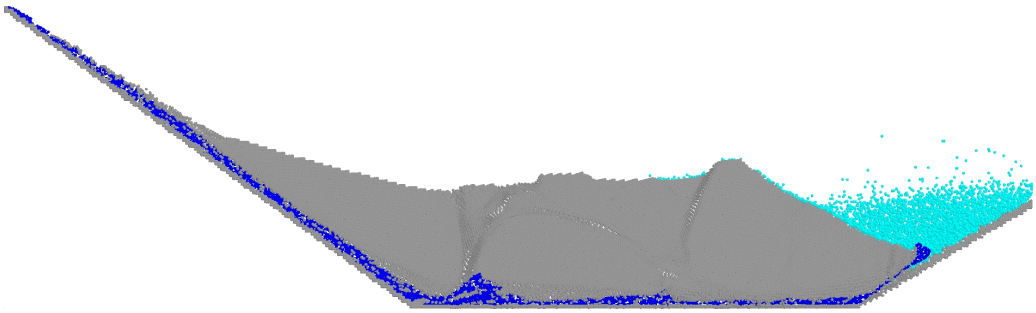

Figure 5.8: Distribution of landslide materials at the end of the motion. The plot indicates the position of material points.

5.4 Concluding remarks

The well-known Vajont landslide case was selected as a real case to check the thermo-hydro-mechanical model developed within the framework of the MPM. Vajont, for the purpose of calibrating model, offers essentially two key items of information: the estimated sliding velocity and the run-out. The model built is based on a representative two-dimensional cross section. The geometry and rock parameters selected profit from previous work on the case and, also, on recent geological investigations. The rock mass above the basal clayey shearing zone was characterized by a brittle Mohr-Coulomb model. A residual friction angle (11°) was adopted for the basal high plasticity clay. However, in view of recent descriptions of the complex nature of the shearing zone, a few "rock bridges" were introduced in an effort to account for the complex geometry and heterogeneous materials involved.

In agreement with real conditions, the failure was triggered by a progressive elevation of the water level in the reservoir (which was also included in the model). Failure and the subsequent accelerated motion occurred at a water elevation close to the actual value. The calculated velocity and run-out also match well the estimated values reported in previous publications.

The model developed is believed to offer an advanced tool to systematically incorporate thermal effects into landslides modelling. It contributes to an increased understanding of phenomena leading to landslide acceleration after failure. The model is capable of reproducing the initial pre-failure state, the onset of failure and the subsequent motion. In the examples described and notably, in the well documented case of Vajont, a single set of material parameters is used.

6

Chapter 6
Conclusions and Future Developments

This final chapter presents the main conclusions of the research work carried out and outlines the main contributions of this thesis. Finally, the current on-working status and future developments are described.

6.1 Final conclusions and contributions

The main goal of this thesis was to develop a model for landslide motion in the presence of thermal effects, by means of the material point method.

A briefly description of existing background information regarding thermally induced landslides was introduced in the first chapter along with the motivation, objectives and methodology of the thesis. The MPM code developed was presented highlighting the improvements made in this work.

The formulation developed to include the heat dissipated by shear deformations into a coupled thermo-hydro-mechanical framework, was included in a material point method framework. A comprehensive calculation tool, capable of simulating

the behaviour of thermally driven landslides from the initial triggering to the post-failure phase was developed. The formulation of the basic theory and the subsequent developments is a generalization of previous contributions in the field of fast landslides. The model developed is believed to offer an advanced tool to systematically incorporate thermal effects into landslides modelling. It contributes to an increased understanding of phenomena leading to landslide acceleration after failure.

One difficulty of the model developed within Material Point Method approach, is the dependence of the results on the thickness of the shear bands developed in a failure scenario. In fact, the method predicts the generation of heat induced excess pore water pressures in shear bands, which controls the available drained shear strength. The described phenomena are strongly dependent on the thickness of the shear band, this results in a strong dependence of the MPM calculations with the discretization mesh. A novel procedure to solve this problem is presented. The shear band thickness, which depends on the material features, is defined as an input parameter. A set of balance equations for the local transfer of liquid and heat is formulated to reproduce the expected thermo-hydro-mechanical coupled physical phenomena inside and in the vicinity of the shear bands.

The procedure to overcome shear band dependence was successfully tested in a reference slope analysis. Thermal interaction phenomena inducing the acceleration of the landslide were found to be independent of mesh size.

A parametric study in a reference case regarding the value of permeability was performed. The MPM formulation presented is capable of recovering no heating effects for high values of permeability as expected.

The well-known Vajont landslide case was selected to evaluate the thermo-hydro-mechanical model developed. Vajont, for the purpose of calibrating model, offers essentially two key items of information: the estimated sliding velocity and the run-out. The model built is based on a representative two-dimensional cross section. In agreement with real conditions, the failure was triggered by a progressive elevation of the water level in the reservoir. Failure and the subsequent accelerated motion occurred at a water elevation close to the actual value. The calculated velocity and run-out also match well the estimated values reported in previous publications.

An additional contribution of the thesis is the analysis of scaled slope failures experiments. It was a useful procedure to check the capabilities of MPM simulations to capture the observed behaviour in the laboratory. The experiments

were analysed as single phase “dry” materials without including neither water or suction effects nor thermal effects. To carry out this analysis, a novel procedure called, particle image velocimetry - numerical particle, was developed to process data from PIV. This procedure is inspired by the MPM calculation procedure and allows tracking information during the motion as strains and displacements assigned to portions of granular materials.

6.2 On-going work status and Future work

There are some numerical limitations with the actual MPM code developed. First, the explicit time integration algorithm used restricts the analysis of long time cases which is a determining factor to analyse creeping behaviour of landslides. To solve such limitation, implicit time integration schemes will be explored as well as the combination of alternative numerical techniques (as FEM) to explore the coupling of creeping phase and rapid motion within MPM.

In addition, the dynamic MPM formulation needs additional stabilization techniques to avoid the oscillations that are present even when the stable solution is reached. Including local damping and smoothing techniques may improve the solution.

On the other hand, regarding localization of shear strains, the thesis faces the dependence of the problem with the shear band thickness. The solution proposed in the thesis to approximate the real thickness of shearing bands will be explored in more detail in the future by means of other regularization techniques such as non-local formulations.

In particular, limitations mentioned above should be overcome in order to be able to simulate problems of landslides covering creeping behaviour and thermally induced rapid motions.

A

Appendix A

MPM code step by step algorithm

In this Appendix, the computational cycle of the MPM code is presented step by step. Detailed information is given for each step. The governing equations presented in Chapter 4 (balance equation of momentum, heat and mass) are solved explicitly as boundary value problems using the weighted residual method, in particular the Galerkin method.

A.1 Computational algorithm

Time integration follows an explicit Euler approach. Solid acceleration, increment of temperature, liquid pressure and stress at time ${}^{k+1}t = {}^{k}t + \Delta t$ are calculated as a function of the variables evaluated at the previous time step.

The computational algorithm consists of the steps indicated below:

1. For time step ${}^{0}t$: definition of the computational mesh and initial material properties, initialization of variables at material points such as the initial position ${}^{0}\mathbf{x}_p$ at the Gauss points, volume ${}^{0}V_p$, mass m_p, velocity ${}^{0}\mathbf{v}_p$, stress

${}^0\sigma_p$, temperature ${}^0\theta_p$, liquid pressure ${}^0p_{L_p}$ and embedded band variables and assignation of constitutive properties and history variables.

2. For time step ${}^kt$: calculation of the shape functions and their gradient associated to nodes evaluated at the position of particles:

$$ {}^kN_i^p = N_i\left({}^k\mathbf{x}_p\right) \tag{A.1} $$

$$ {}^k\left(\nabla N_i^p\right) = \nabla N_i\left({}^k\mathbf{x}_p\right) \tag{A.2} $$

3. Calculation of the lumped mass matrix and lumped volume matrix:

$$ {}^km_i = \sum_{p=1}^{N_p} m_p\,{}^kN_i^p \tag{A.3} $$

4. Calculation of internal forces at nodes using element-wise stress averaging (Zabala, 2010; Zabala and Alonso, 2011) and using selective reduced integration strategy:

$$ {}^kf_i^{\text{int}} = \sum_{p=1}^{N_p} {}^k\left(\nabla N_i^p\right)\cdot {}^k\sigma_p \frac{m_p}{{}^km_{el}}\,{}^kV_{el} \tag{A.4} $$

5. Calculation of body forces at nodes:

$$ {}^k\mathbf{b}_i = \sum_{i=1}^{N_p} m_p\mathbf{g}\,{}^kN_i^p \tag{A.5} $$

6. Calculation of external forces at nodes:

$$ {}^kf_i^{ext} = \int_{\Gamma_t} \rho\,{}^kN_i^p\cdot {}^k\hat{\mathbf{t}}\,\mathrm{d}\Gamma_t + {}^k\mathbf{b}_i \tag{A.6} $$

7. Calculation of the increment of momentum at nodes:

$$^{k+1}\Delta\left(m_i\mathbf{v}_i\right) = {}^{k}f_i^{ext}\,\Delta t - {}^{k}f_i^{\text{int}}\,\Delta t \tag{A.7}$$

8. Update of the position, velocity and acceleration of material points:

$$^{k+1}\mathbf{x}_p = {}^{k}\mathbf{x}_p + \frac{\Delta t}{{}^{k}m_i}\sum_{i=1}^{Nn}\left[{}^{k}\left(m_i\mathbf{v}_i\right) + {}^{k+1}\Delta\left(m_i\mathbf{v}_i\right)\right]{}^{k}N_i^p \tag{A.8}$$

$$^{k+1}\mathbf{v}_p = {}^{k}\mathbf{v}_p + \frac{1}{{}^{k}m_i}\sum_{i=1}^{Nn}\left[{}^{k+1}\Delta\left(m_i\mathbf{v}_i\right)\right]{}^{k}N_i^p \tag{A.9}$$

$$^{k+1}\mathbf{a}_p = \frac{1}{{}^{k}m_i\Delta t}\sum_{i=1}^{Nn}\left[{}^{k+1}\Delta\left(m_i\mathbf{v}_i\right)\right]{}^{k}N_i^p \tag{A.10}$$

9. Update of the nodal velocities following the Modified Update Stress Last (MUSL) (Sulsky et al., 1994):

$$^{k+1}\left(m_i\mathbf{v}_i\right) = \sum_{p=1}^{Np} m_p\,{}^{k+1}\mathbf{v}_p\,{}^{k}N_i^p \tag{A.11}$$

This step is required to avoid divisions by a shape function which may involve numerical problems when a particle is near to a node. For a discussion on this, the readers are referred to Zhang et al. (2017).

10. Calculation of strain increment using reduced integration strategy and update of the strain tensor at particles:

$$^{k+1}\Delta\varepsilon_p = \Delta t\sum_{i=1}^{Nn}\frac{^{k+1}\Delta\left({}^{k}N_i^p\right)m_i\mathbf{v}_i}{{}^{k}m_i} \tag{A.12}$$

$$^{k+1}\varepsilon_p = {}^{k}\varepsilon_p + {}^{k+1}\Delta\varepsilon_p \tag{A.13}$$

11. Map temperature from material points to nodes:

$$ {}^{k}\theta_i = \frac{1}{{}^{k}m_i} \sum_{p=1}^{N_p} m_p {}^{k}\theta_p {}^{k}N_i^p \tag{A.14} $$

12. Calculation to the Fourier's heat flow associated to material points:

$$ {}^{k}\mathbf{q}_{h_p} = -\Gamma \sum_{n=1}^{N_n} {}^{k}\left(\nabla N_i^p\right) {}^{k}\theta_i \tag{A.15} $$

13. Map liquid pressure in material points to nodes:

$$ {}^{k}p_{L_i} = \frac{1}{{}^{k}m_i} \sum_{p=1}^{N_p} m_p {}^{k}p_{L_p} {}^{k}N_i^p \tag{A.16} $$

14. Calculation of gradient of liquid pressure associated to material points:

$$ {}^{k}\nabla p_{L_p} = \sum_{i=1}^{N_n} \nabla N_i^{P\,k} p_{L_i} \tag{A.17} $$

15. Calculation of Darcy's flow:

$$ {}^{k}\mathbf{q}_p = -\frac{k}{\gamma_L}\left({}^{k}\nabla p_{L_p} + \rho_L {}^{k}\mathbf{b}_p + \rho_L {}^{k}\mathbf{a}_{S_p}\right) \tag{A.18} $$

16. Calculation of temperature increment at nodes:

$$ \begin{aligned} \Delta\theta_i = \tfrac{1}{(\rho c)_m {}^{k}V_i} \Bigg[& \sum_{p=1}^{N_p} {}^{k}\left(\nabla N_i^p\right) {}^{k}\mathbf{q}_{h_p}\, \Delta t {}^{k}V_p - \int_{\Gamma_{q_h}} {}^{k}N_i {}^{k}\hat{q}_h \Delta t \mathrm{d}\Gamma + \\ & \sum_{p=1}^{N_p} \rho_w c_w {}^{k}\theta_p {}^{k}\left(\nabla N_i^p\right) {}^{k}\mathbf{q}_p \Delta t {}^{k}V_p - \int_{\Gamma_{q_L}} \rho_w c_w {}^{k}\theta_p {}^{k}N_i {}^{k}\hat{q}_L \Delta t \mathrm{d}\Gamma - \\ & \sum_{p=1}^{N_p} (\rho c)_m {}^{k}N_i^{p\,k}\theta_p {}^{k}\Delta\varepsilon_{vol_p} {}^{k}V_p + \sum_{p=1}^{N_p} N_i^p \psi_\theta \left({}^{k}\theta_p - {}^{k}\theta_p^J\right) V_p \Bigg] \end{aligned} \tag{A.19} $$

17. Update temperature at material points:

$$^{k+1}\theta_p = {}^{k}\theta_p + \sum_{i=1}^{Nn} {}^{k+1}\Delta\theta_i \, {}^{k}N_i^p$$

18. Calculation of liquid pressure increment at nodes:

$$^{k+1}\Delta p_{L_i} = \frac{1}{{}^{k}V_i}\left[Q \sum_{p=1}^{N_p} {}^{k}N_i^p \left(\beta^{k+1}\Delta\theta_p + {}^{k+1}\Delta\varepsilon_{vol_p}\right){}^{k}V_p + \int_{\Gamma_q} {}^{k}N_i \hat{q}_L \Delta t \mathrm{d}\Gamma_q - \sum_{p=1}^{N_p} {}^{k}\nabla N_i^p \cdot {}^{k}\mathbf{q}_p \Delta t \, {}^{k}V_p + \sum_{p=1}^{N_p} N_i^p \psi_L \left({}^{k}p_{L_p} - {}^{k}p_{L_p}^J\right)\right] \tag{A.20}$$

19. Update pore pressure at material points:

$$^{k+1}p_{L_P} = {}^{k}p_{L_p} + \sum_{i=1}^{Nn} {}^{k+1}\Delta p_{L_i} \, {}^{k}N_i^p \tag{A.21}$$

20. Calculation of effective and total stress increment at particles:

$$^{k+1}\Delta\sigma'_p = {}^{k}\mathbf{D} \cdot {}^{k+1}\Delta\varepsilon_p \tag{A.22}$$

$$^{k+1}\Delta\sigma_p = {}^{k+1}\Delta\sigma'_p + {}^{k+1}\Delta p_{L_i} \tag{A.23}$$

21. Update total stress:

$$^{k+1}\sigma'_p = {}^{k}\sigma'_p + {}^{k+1}\Delta\sigma'_p \tag{A.24}$$

22. Calculation of temperature and liquid pressure at joints:

$$^{k+1}\Delta\theta_P^J = \Delta t \left(-\psi_\theta \left({}^{k}\theta_P - {}^{k}\theta_P^J\right) + \frac{L_{ref}}{L_J}({}^{k}\sigma'_P{}^{k} : \dot{\varepsilon}_P^p)\right) \tag{A.25}$$

$$^{k+1}\Delta p^J_{L_P} = Q\beta^k \Delta\theta^J_P - \Delta t \psi_L \left(^k p_{L_P} - ^k p^J_{L_P} \right) \tag{A.26}$$

23. Update properties such as porosity, liquid density and porosity dependent variables.

24. Go to step 2 for a new time step calculation.

Nomenclature

$\mathbf{a}_L$	acceleration of liquid	m/s^2
$\mathbf{a}_{L/S}$	acceleration of liquid with respect to the solid particles	m/s^2
$\mathbf{a}_p^{tk+1}$	acceleration vector at time $tk+1$ of the numerical particles p	m/s^2
A_{ref}	reference area for interaction between band and matrix	m^2
$\mathbf{a}_S$	acceleration of solid particles	m/s^2
$\mathbf{b}$	body forces	N
$\mathbf{B}_\mathbf{j}^\mathbf{k}(x_p)$	strain matrix at time k at position of the numerical particle p	-
c'	effective cohesion	Pa
c_L	specific heat of liquid	N·m/(kg·°C)
c_s	specific heat of solid	N·m/(kg·°C)
$\mathbf{D}$	tangent matrix	Pa
$\frac{D(\cdot)}{Dt}$	material derivative with respect the time	1/s
e	half thickness of the shear band	m
e_{ij}^p	ij component of the deviatoric part of the plastic strain tensor	-
f_L^{B-M}	local flow rate of liquid per unit of volume and time	$kg/m^3{\cdot}s$
f_θ^{B-M}	local flow rate of energy per unit of volume and time	$kg/m^3{\cdot}s$
$\dot{H}$	heat rate per unit of volume	$J/(m^3{\cdot}s)$
$\dot{H}^B$	heat rate per unit volume at embedded shear bands	$J/(m^3{\cdot}s)$
h_1, h_2	height of samples 1 and 2 respectively	m
k	intrinsic permeability	m^2
K	permeability	m/s
l	sample lenth	m
l_x, l_y	horizontal and vertical lengths of the element	m
$\mathbf{m}$	matrix of elements $m_{ij} = \delta_{ij}$	-
m_{el}	mass of the mesh element	kg
m_v	oedometric compressibility coefficient	1/Pa
n	porosity	-
N_i	Standard shape functions	-
N_n	Total number of nodes of the support mesh	-

N_p	Total number of numerical particles	-
p_L	liquid pressure	Pa
p_L^0	reference liquid pressure	Pa
p_L^B	liquid pressure at embedded shear bands	Pa
p_L^M	liquid pressure at matrix	Pa
$\mathbf{q}_h$	heat flow conduction	J/m^2·s
$\mathbf{q}_L$	darcy flow rate	m/s
t	time	s
v	velocity	m/s
V_{el}	volume of the mesh element	m^3
$\mathbf{u(t)}$	displacement vector increments	m
$\mathbf{u_j(t)}$	displacement vector of node j at time t	m
$\mathbf{u_p^{tk+1}}$	displacement vector inc. time $tk+1$ of numerical particle p	m
$\mathbf{u_p(t)}$	displacement vector inc. at time t of numerical particle p	m
$\mathbf{v_p^{tk+1}}$	velocity vector at time $tk+1$ of numerical particle p	m/s
$\dot{W}_1, \dot{W}_2$	mechanical work rate per unit of volume of samples	J/(m^3·s)
$\mathbf{x_p^{tk+1}}$	position vector at time $tk+1$ of numerical particles p	m
α_L	liquid phase compressibility	Pa
β	volumetric thermal expansion coefficient for the mixture	1/°C
β_L	volumetric thermal expansion coefficient for liquid	1/°C
β_S	volumetric thermal expansion coefficient for solid	1/°C
$\dot{\delta}$	displacement rate	m/s
δ_{ij}	kronecker delta	-
$\frac{\partial(\cdot)}{\partial t}$	partial derivative with respect to time	1/s
$\Delta\varepsilon_d^p$	increment of the deviatoric strain invariant at different times	-
$\Delta\varepsilon_p^{tk+1}$	strain increment at time $tk+1$ of numerical particles p	-
$\Delta e_i j^p$	deviatoric component of the strain increment	-
Δt	time elapsed between two successive digital images	s
$\dot{\varepsilon}^p$	plastic strain rate tensor	1/s
ε_p^{tk+1}	accumulated strain at time $tk+1$ of numerical particles p	-
ϕ'	effective friction angle	°
Γ	fourier's thermal conduction coefficient	J/(m·s·°C)
γ_L	specific weight of liquid	N/m^3
$\dot{\gamma}_1, \dot{\gamma}_2$	shear strain rate of samples 1 and 2 respectively	1/s
η	shape factor controlling strength softening	-
μ_L	liquid viscosity	Pa·s
θ	temperature	°C
θ^0	reference temperature	°C

θ^B	temperature at embedded shear bands	°C
θ^M	temperature at matrix	°C
ρ	density of the mixture	kg/m^3
$(\rho c)_m$	specific heat of the mixture	J/(m^3·°C)
ρ_L	liquid density	kg/m^3
ρ_L^0	liquid density at reference liquid pressure and temperature	kg/m^3
ρ_S	solid density	kg/m^3
ρ_S^0	solid density at reference temperature	kg/m^3
σ	cauchy total stress tensor	Pa
σ'	cauchy effective stress tensor	Pa
σ_n	total normal stress	Pa
τ_f	final shear strength	Pa
ψ_L	energy transfer coefficient	kg/(m^3·s·Pa)
ψ_θ	liquid transfer coefficient	J/(m^3·s·°C)
ζ_j, η_j	local coordinates of node j	-
$\nabla(\cdot)$	divergence vector operator	1/m

Bibliography

Abbo, A. J. and S. W. Sloan
1995. A smooth hyperbolic approximation to the Mohr-Coulomb yield criterion. *Computers and Structures*, 54(3):427–441.

Abe, K., K. Soga, and S. Bandara
2014. Material point method for coupled hydromechanical problems. *Journal of Geotechnical and Geoenvironmental Engineering*, 140(3):1–16.

Adrian, R.
1991. Particle-imaging techniques for experimental fluid mechanics. *Annual Review of Fluid Mechanics*, 23:261–304.

Al-Kafaji, I. K. J.
2013. *Formulation of a Dynamic Material Point Method (MPM) for Geomechanical Problems*. PhD thesis, Universität Stuttgart.

Alonso, E. and N. Pinyol
2012. The Vaiont landslide revisited. In *Proceeding of the 2nd Italian Workshop on Landslide*, Pp. 9–24, Napoli.

Alonso, E. E. and N. M. Pinyol
2010. Criteria for rapid sliding I. A review of Vaiont case. *Engineering Geology*, 114(3-4):198–210.

Alonso, E. E., N. M. Pinyol, and A. M. Puzrin
2010. *Geomechanics of Failures. Advanced Topics*. Springer.

Alonso, E. E., A. Zervos, and N. M. Pinyol
2016. Thermo-poro-mechanical analysis of landslides: from creeping behaviour to catastrophic failure. *Géotechnique*, 66(3):202–219.

Alshibli, K. A. and A. Hasan
2008. Spatial variation of void ratio and shear band thickness in sand using X-ray computed tomography. *Géotechnique*, 58(4):249–257.

Alvarado, M., A. Ruiz, and N. Pinyol
2016. Material Point Method analysis of induced laboratory scaled landslide. In *Landslides and Engineered Slopes. Experience, Theory and Practice: Proceedings of the 12th International Symposium on Landslides*, Pp. 309–316, Napoli.

Bandara, S. S.
2013. *Material point method to simulate large deformation problems in fluid-saturated granular medium.* PhD thesis, University of Cambridge.

Bardenhagen, S. G., J. U. Brackbill, and D. Sulsky
2000. The material-point method for granular materials. *Computer Methods in Applied Mechanics and Engineering*, 187(3-4):529–541.

Bardenhagen, S. G., J. E. Guilkey, K. M. Roessig, J. U. Brackbill, and W. M. Witzel
2001. An Improved Contact Algorithm for the Material Point Method and Application to Stress Propagation in Granular Material. *Computer Modeling in Engineering and Sciences*, 2(4):509–522.

Bardenhagen, S. G. and E. M. Kober
2004. The generalized interpolation material point method. *Computer Modeling in Engineering and Sciences*, 5(6):477–495.

Belytschko, T., Y. Lu, and L. Gu
1994. Element-free Galerkin method. *International Journal for Numerical Methods in Engineering*, 37:229–256.

Biot, M. A.
1941. General theory of three-dimensional consolidation. *Journal of Applied Physics*, 12(2):155–164.

Biot, M. A.
1962. Generalized theory of acoustic propagation in porous dissipative media. *The Journal of the Acoustical Society of America*, 34(5):1254–1264.

Caicedo, B. and L. Thorel
2014. Centrifuge modelling of unsaturated soils. *Journal of Geo-Engineering Science*, 2:83–103.

Cao, T. D., L. Sanavia, and B. A. Schrefler
2016. A thermo-hydromechanical model for multiphase geomaterials in dynamics with application to strain localization simulation. *Int. J. Numer. Methods Engng*, 107(4):312–337.

Cecinato, F. and A. Zervos
2012. Influence of thermomechanics in the catastrophic collapse of planar landslides. *Canadian Geotechnical Journal*, 49(2):207–225.

Cecinato, F., A. Zervos, and E. Veveakis
2011. A thermo-mechanical model for the catastrophic collapse of large landslides. *International Journal for Numerical and Analytical Methods in Geomechanics*, 35:1507–1535.

Ciabatta, M.
1964. La dinamica della frana del Vajont. *Giornale di Geologia XXXII*, I:139–154.

Collatz, L.
1955. *Numerische Behandlung von Differentialgbeichungen*. Berlin: Springer.

Cundall, P. A.
1987. Distinct element models of rock and soil structure. In *In Analytical and Conlputational Methods in Engineering Rock Mechanics*, E. T. Brown, ed., Pp. 129–163. London: Allen and Unwin.

Cundall, P. A. and O. D. L. Strack
1979. A discrete numerical model for gran ular assemblies. *Géotechnique*, 29(1):47–65.

Dieterich, J. H.
1979. Modeling of rock friction: 1. Experimental results and constitutive equations. *Journal of Geophysical Research: Solid Earth*, 84(B5):2161–2168.

Donea, J., P. Fasoli-Stella, and S. Giuliani
1977. Lagrangian and Eulerian Finite element techniques for transient fluid-structure interaction problems. In *Transactions of the 4th International Conference on Structural Mechanics in Reactor Technology*, volume B, Pp. 1–12, San Francisco.

Eymard, R., T. Gallouët, and R. Herbin
2000. The finite volume method. In *Handbook of Numerical Analysis*, P. G. Ciarlet and J. L. Lions, eds., volume VII, Pp. 713–1020.

Ferri, F., G. Di Toro, T. Hirose, R. Han, H. Noda, T. Shimamoto, M. Quaresimin, and N. De Rossi
2011. Low- to high-velocity frictional properties of the clay-rich gouges from the slipping zone of the 1963 Vaiont slide, northern Italy. *Journal of Geophysical Research: Solid Earth*, 116(9):1–17.

Ferri, F., G. Di Toro, T. Hirose, and T. Shimamoto
2010. Evidence of thermal pressurization in high-velocity friction experiments on smectite-rich gouges. *Terra Nova*, 22(5):347–353.

Finlayson, B. A.
1972. *The method of weighted residuals and variational principles, with application in fluid mechanics, heat and mass transfer*, Mathematics in Science and Engineering. Elsevier Science.

Finlayson, B. A. and L. E. Scriven
1966. The Method of Weighted Residuals. A Review. *Applied Mechanics Reviews*, 19(6):735–748.

Gajo, A. and R. Denzer
2011. Finite element modelling of saturated porous media at finite strains under dynamic conditions with compressible constituents. *Int. J. Numer. Methods Engng*, 13(85):1705–1736.

Gingold, R. A. and J. J. Monaghan
1977. Smoothed particle hydrodynamics: theory and application to non-spherical stars. *Monthly Notices of the Royal Astronomical Society*, 181:375–389.

Goren, L. and E. Aharonov
2007. Long runout landslides: The role of frictional heating and hydraulic diffusivity. *Geophysical Research Letters*, 34(7):1–7.

Goren, L. and E. Aharonov
2009. On the stability of landslides: A thermo-poro-elastic approach. *Earth and Planetary Science Letters*, 277(3-4):365–372.

Goren, L., E. Aharonov, and M. H. Anders
2010. The long runout of the Heart Mountain landslide: Heating, pressurization, and carbonate decomposition. *Journal of Geophysical Research: Solid Earth*, 115(10):1–15.

Habib, P.
1967. Sur un mode de glissement des massifs rocheux. *Comptes Rendus Acad. Sci*, Pp. 151–153.

He, S. M., W. Liu, and J. Wang
2015. Dynamic simulation of landslide based on thermo-poro-elastic approach. *Computers and Geosciences*, 75:24–32.

Hendron, A. and F. Patton
1985. The Vaiont slide, a geotechnical analysis based on new geologic observations. *US Army Corps of Engineers*, 2:187–188.

Huang, M., Q. Y. Zhong, L. G. Tham, and O. C. Zienkiewicz
2004. On the stable finite element procedures for dynamic problems of saturated porous media. *Int. J. Numer. Methods Engng*, 9(61):1421–1450.

Idelsohn, S. R., E. Oñate, and F. Del Pin
2003. A Lagrangian meshless finite element method applied to fluid-structure interaction problems. *Computers & Structures*, 81(8-11):655–671.

Jassim, I., D. Stolle, and P. Vermeer
2013. Two-phase dynamic analysis by material point method. *International Journal for Numerical and Analytical Methods in Geomechanics*, 37(15):2502–2522.

Jeremic, B., Z. Cheng, M. Taiebat, and Y. Dafalias
2008. Numerical simulation of fully saturated porous materials. *Int. J. Numer. Analyt. Methods Geomech*, 13(32):1635–1660.

Lòpez-Querol, S., J. A. Fernández-Merodo, P. Mira, and M. Pastor
2008. Numerical modelling of dynamic consolidation on granular soils. *Int. J. Numer. Anal. Meth. Geomech.*, 32(12):1431–1457.

Lu, H. and P. D. Cary
2000. Deformation measurements by digital image correlation: Implementation of a second-order displacement gradient. *Experimental Mechanics*, 40(4):393–400.

Monaghan, J. J.
1988. An introduction to SPH. *Comput Phys Commun*, 48:89–96.

Mühlhaus, H. B. and I. Vardoulakis
1987. The thickness of shear bands in granular materials. *Géotechnique*, 37(3):271–283.

Müller, L.
1964. The rock slide in the Vajont Valley. *Rock Mechanics and Engineering Geology*, 2:148–212.

Nonveiller, E.
1987. The Vajont reservoir slope failure. *Engineering Geology*, 24:493–512.

Pan, B., A. Asundi, H. Xie, and J. Gao
2009. Digital image correlation using iterative least squares and pointwise least

squares for displacement field and strain field measurements. *Optics and Lasers in Engineering*, 47(7-8):865–874.

Pan, B., H. Xie, Z. Guo, and T. Hua
2007. Full-field strain measurement using a two-dimensional SavitzkyâĂŞGolay digital differentiator in digital image correlation. *Optical Engineering*, 46:46 – 46 – 10.

Paronuzzi, P. and A. Bolla
2015. Gravity-induced rock mass damage related to large en masse rockslides: Evidence from Vajont. *Geomorphology*, 234:28–53.

Pastor, M., O. C. Zienkiewicz, and A. H. C. Chan
1990. Pastor, Zienkiewicz, Chan - 1990 - Generalized plasticity and the modelling of soil behaviour.pdf. *Int. J. Numer. Analyt. Methods Geomech*, 3(14):151–190.

Pinyol, N. M. and E. E. Alonso
2010a. Criteria for rapid sliding II. Thermo-hydro-mechanical and scale effects in Vaiont case. *Engineering Geology*, 114(3-4):211–227.

Pinyol, N. M. and E. E. Alonso
2010b. Fast planar slides. A closed-form thermo-hydro-mechanical solution. *International journal for numerical and analytical methods in geomechanics*, 34(1):27–52.

Pinyol, N. M. and M. Alvarado
2017. Novel analysis for large strains based on particle image velocimetry. *Canadian Geotechnical Journal*, 12(February):1–12.

Pinyol, N. M., M. Alvarado, E. E. Alonso, and F. Zabala
2017a. Thermal effects in landslide mobility. *Géotechnique*, (2012):1–18.

Pinyol, N. M., M. Alvarado, F. Parera, and A. Yerro
2017b. Novel Procedure to Validate MPM Results by Means of PIV Measurements. *Procedia Engineering*, 175:332–340.

Pouliquen, O.
1999. Scaling laws in granular flows down rough inclined planes. *Physics of Fluids*, 11(3):542–548.

Prevost, J. H.
1980. Mechanics of continuous porous media. *Int. J. Engng Sci.*, 6(18):787–800.

Ruina, A.
1983. Slip instability and state variable friction laws. *Journal of Geophysical Research: Solid Earth*, 88(B12):10359–10370.

Ruiz, Á., M. Alvarado, and N. M. Pinyol
2017a. Análisis MPM de la rotura de un talud ensayado en centrífuga . Comparación de los resultados con medidas procesadas mediante PIV-NP. In *Congreso de Métodos Numéricos en Ingeniería CMN*, Valencia.

Ruiz, Á., M. Alvarado, N. M. Pinyol, and B. Caicedo
2017b. Wetting Collapse and Failure of an Slope Tested in Centrifuge Machine. In *JTC1 Workshop on Advances in Landslide Understanding*, Pp. 24–27.

Scarpelli, G. and D. M. Wood
1982. Experimental observations of shear band patterns in direct shear tests. In *In Proceedings of the IUTAM conference on deformation and failure of granular materials*, P. A. Vermeer and H. J. Luger, eds., Pp. 473–484.

Schrefler, B. and R. Scotta
2001. A fully coupled dynamic model for two-phase fluid flow in deformable porous media. *Computer Methods in Applied Mechanics and Engineering*, 3223:3223–3246.

Semenza, E.
2001. *La Storia del Vaiont Raccontata del Geologo che ha Scoperto la Frana*. Tecomproject Editore Multimediale.

Skempton, A. W.
1985. Residual strength of clays in landslides, folded strata and the laboratory. *Géotechnique*, 35(1):3–18.

Sloan, S. W.
1987. Substepping schemes for the numerical integration of elastoplastic stress-strain relations. *International journal for numerical methods in ...*, 24(September 1986):893–911.

Soga, K., E. Alonso, A. Yerro, K. Kumar, and S. Bandara
2016. Trends in large-deformation analysis of landslide mass movements with particular emphasis on the material point method. *Géotechnique*, 66(3):248–273.

Sosio, R., G. B. Crosta, and O. Hungr
2008. Complete dynamic modeling calibration for the Thurwieser rock avalanche (Italian Central Alps). *Engineering Geology*, 100(1-2):11–26.

Stanier, S., J. Blaber, W. Take, and D. White
2016. Improved image-based deformation measurement for geotechnical applications. *Canadian Geotechnical Journal*, 53(5):727–739.

Sture, S., N. Costes, S. Batiste, M. Lankton, K. AlShibli, B. Jeremic, R. Swanson, and M. Frank
1998. Mechanics of granular materials at low effective stresses. *Journal of Aerospace Engineering*, 11(3):67–72.

Sture, S., N. Costes, S. Batiste, M. R. Lankton, K. Alshibli, B. Jeremic, R. A. Swanson, and M. Frank
2009. Mechancis of granular materials at low effecive stresses. *Journal of Chemical Information and Modeling*, 53(3):556–581.

Sulsky, D., Z. Chen, and H. L. Schreyer
1994. A particle method for history-dependent materials. *Computer Methods in Applied Mechanics and Engineering*, 118(1-2):179–196.

Sulsky, D. and H. L. Schreyer
1996. Axisymmetric form of the material point method with applications to upsetting and Taylor impact problems. *Computer Methods in Applied Mechanics and Engineering*, 139(1-4):409–429.

Sulsky, D., S.-J. Zhou, and H. L. Schreyer
1995. Application of a particle-in-cell method to solid mechanics. *Computer Physics Communications*, 87(1-2):236–252.

Sutton, M., J. L. Turner, H. A. Bruck, and T. Chao
1991. Full-field representation of discretely sampled surface deformation for displacement and strain analysis. *Exp. Mech*, 31:168–177.

Take, W. A.
2015. Thirty-Sixth Canadian Geotechnical Colloquium: Advances in visualization of geotechnical processes through digital image correlation ¹. *Canadian Geotechnical Journal*, 52(9):1199–1220.

Take, W. A., M. D. Bolton, P. C. P. Wong, and F. J. Yeung
2004. Evaluation of landslide triggering mechanisms in model fill slopes. *Landslides*, 1(3):173–184.

Thielicke, W. and E. J. Stamhuis
2014. PIVlab - Towards User-friendly, Affordable and Accurate Digital Particle Image Velocimetry in MATLAB. *Journal of Open Research Software*, 2:2–10.

Tika, T. E. and J. N. Hutchinson
1999. Ring shear tests on soil from the Vaiont landslide slip surface. *Geotechnique*, 49(1):59–74.

Tika, T. E., P. R. Vaughan, and L. J. Lemos
1996. Fast shearing of pre-existing shear zones in soil. *Géotechnique*, 46(2):197–233.

Tong, W.
1997. Detection of plastic deformation patterns in a binary aluminum alloy. *Exp. Mech*, 37:452–459.

Uriel, S. and R. Molinia
1977. Kinematic aspects of Vaiont slide. In *Proceedings of the 3th International Conference of the ISRMR*, National Academy of Sciences, ed., volume 2B, Pp. 865–870, Denver, USA.

Uzuoka, R. and R. I. Borja
2012. Dynamic of unsaturated poroelastic solids at finite strain. *Int. J. Numer. Analyt. Methods Geomech*, 36(13):1535–1573.

Vardoulakis, I.
1980. Shear band inclination and shear modulus of sand in biaxial tests. *Int. J. Numer. Analyt. Methods Geomech.*, 4(2):113–119.

Vardoulakis, I.
2000. Catastrophic landslides due to frictional heating of the failure plane. *Mechanics of Cohesive-Frictional Materials*, 5(6):443–467.

Vardoulakis, I.
2002. Dynamic thermo-poro-mechanical analysis of catastrophic landslides. Geotechnique. *Geotechnique*, 52(3):157–171.

Verruijt, A.
2010. Theory and applications of Transport in Porous Media. In *An Introduction to Soil Dynamics*. Berlin, Heidelberg: Springer.

Veveakis, E., I. Vardoulakis, and G. Di Toro
2007. Thermoporomechanics of creeping landslides: The 1963 slide, northern Italy. *Journal of Geophysical Research*, 112(F3):2156–2202.

Voight, B. and C. Faust
1982. Frictional heat and strength loss in some rapid landslides. *Géotechnique*, 32(1):43–54.

Wang, F. W., K. Sassa, and G. Wang
2002. Mechanism of a long-runout landslide triggered by the August 1998 heavy rainfall in Fukushima Prefecture, Japan. *Engineering Geology*, 63(1-2):169–185.

Wattrisse, B., A. Muracciole, and J. Nemoz-Gaillard
2001. Analysis of strain localization during tensile tests by digital image correlation. *Exp. Mech*, 41:29–39.

Wedage, A., N. R. Morgenstern, and D. H. Chan
1998. A strain rate dependent constitutive model for clays at residual strength. *Canadian Geotechnical Journal*, 35(2):364–373.

White, D., W. Take, and M. Bolton
2003. Soil deformation measurement using particle image velocimetry (PIV) and photogrammetry. *Geothechnique*, 53(7):619–631.

White, D. J. and M. D. Bolton
2004. Displacement and strain paths during plane-strain model pile installation in sand. *Géotechnique*, 54(6):375–397.

Wolter, A., D. Stead, and J. J. Clague
2014. A morphologic characterisation of the 1963 Vajont Slide, Italy, using long-range terrestrial photogrammetry. *Geomorphology*, 206:147–164.

Yerro, A.
2015. *MPM modelling of landslides in brittle and unsaturated soils*. PhD thesis.

Yerro, A., E. Alonso, and N. Pinyol
2014. Modelling progressive failure with MPM. In *Numerical Methods in Geotechnical Engineering*, M. Hicks, R. B. J. Brinkgreve, and A. Rohe, eds., Pp. 319–323. 214 Taylor & Francis Group.

Yerro, A., E. E. Alonso, and N. M. Pinyol
2016a. Run-out of landslides in brittle soils. *Computers and Geotechnics*, 80:427–439.

Yerro, A., N. M. Pinyol, and E. E. Alonso
2016b. Internal progressive failure in deep-seated landslides. *Rock Mechanics and Rock Engineering*, 49(6):2317–2332.

Zabala, F.
2010. *Modelación de problemas geoternicos hidromecanicos utilizando el metodo del punto material*. PhD thesis, Polytechnic University of Catalonia.

Zabala, F. and E. E. Alonso
2011. Progressive failure of Aznalcóllar dam using the material point method. *Géotechnique*, 61(9):795–808.

Zabala, F. and E. E. Alonso
2012. The Material Point Method and the analyisis of dams and dam failures. In

Innovative Numerical Modelling in Geomechanics, A. Roberto, ed., chapter 8, Pp. 171–177.

Zabala, F., R. Rodari, and L. Oldecop
2004. Localización de deformaciones en estructuras utilizando el Método del Punto Material. *Revista Engenharia Estrutural*, 1290(5400):11–29.

Zhang, H. W., K. P. Wang, and Z. Chen
2009. Material point method for dynamic analysis of saturated porous media under external contact/impact of solid bodies. *Computer Methods in Applied Mechanics and Engineering*, 198(17-20):1456–1472.

Zhang, X., Z. Chen, and Y. Liu
2017. *The Material Point Method A Continuum-Based Particle Method*.

Zienkiewicz, O.
1989. *The finite element method. Vol. 1. Basic formulation and linear problems*. London: McGraw-Hill.

Zienkiewicz, O. C.
1977. *The Finite Element Method in Engineering Science*. London: McGraw-Hill.

Zienkiewicz, O. C., A. H. C. Chan, M. Pastor, B. A. Schrefler, and T. Shiomi
1999. *Computational geomechanics with special reference to earthquake engineering*. Chichester, UK: Wiley.

Zienkiewicz, O. C. and T. Shiomi
1984. Dynamic behaviour of saturated porous media; the generalized Biot formulation and its numerical solution. *International Journal for Numerical and Analytical Methods in Geomechanics*, 8(1):78–96.

List of publications

At indexed journals

Thermal effects in landslide mobility (2017)
Authors: Pinyol N., **Alvarado M.**, Alonso E., Zabala F.
Journal: Géotechnique, DOI: 10.1680/jgeot.17.P.054

Novel analysis for large strains based on particle image velocimetry (2017)
Authors: Pinyol N., **Alvarado M.**
Journal: Canadian Geotechnical Journal, 54(7): 933-944, DOI: 10.1139/cgj-2016-0327

At conferences

Novel procedure to validate MPM results by means of PIV measurements (2017)
Authors: Pinyol N., **Alvarado M.**, Parera F., Yerro A.
Journal: Procedia Engineering, 177: 332-340, DOI: 10.1016/j.proeng.2017.01.039

Effect of shear band thickness on the termo-hydromechanical coupled analysis of landslides (2017)
Authors: Pinyol N., **Alvarado M.**, Alonso E.
In: JTC1 Workshop Advances in Landslide Understanding: proceedings of the First JTC1 Workshop: Advances in Landslide Understanding, Barcelona, Spain, pp. 52-55

Wetting collapse and failure of and slope tested in centrifuge machine (2017)
Authors: Pinyol N., Ruiz A.,**Alvarado M.**, Bernardo C.

In: JTC1 Workshop Advances in Landslide Understanding: proceedings of the First JTC1 Workshop: Advances in Landslide Understanding, Barcelona, Spain, pp. 122-125

Aceleración de deslizamientos por efectos térmicos: modelación mediante el método del punto material (2017)
Authors: **Alvarado M.**, Pinyol N., Alonso E.
In: TALUDES 2017: IX Simposio Nacional sobre Taludes y Laderas Inestables, Santander, España, pp. 1313-1320

Nuevo método para la interpretación de imágenes digitales de inestabilidad mediante la técnica PIV (2017)
Authors: **Alvarado M.**, Ruiz A., Pinyol N.
In: TALUDES 2017: IX Simposio Nacional sobre Taludes y Laderas Inestables, Santander, España, pp. 307-313

Material Point Method analysis of induced laboratory scaled landslide (2016)
Authors: **Alvarado M.**, Ruiz A., Pinyol N.
In: Landslides and Engineered Slopes. Experience, Theory and Practice: Proceedings of the 12th International Symposium on Landslides, Napoli, Italy, pp. 309-316